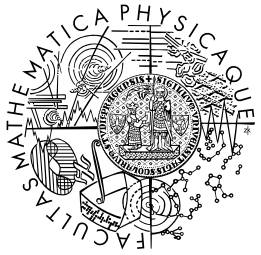

FACULTY
OF MATHEMATICS
AND PHYSICS
Charles University

DOCTORAL THESIS

Radim Slovák

Study of jet fragmentation and inclusive jet production in heavy-ion collisions with the ATLAS experiment

Institute of Particle and Nuclear Physics

Supervisor of the doctoral thesis:	Mgr. Martin Spousta, Ph.D.
Study programme:	Physics
Study branch:	Subnuclear physics

Prague 2017

I declare that I carried out this doctoral thesis independently, and only with the cited sources, literature and other professional sources.

I understand that my work relates to the rights and obligations under the Act No. 121/2000 Sb., the Copyright Act, as amended, in particular the fact that the Charles University has the right to conclude a license agreement on the use of this work as a school work pursuant to Section 60 subsection 1 of the Copyright Act.

In Prague, 4th July 2017

Title: Study of jet fragmentation and inclusive jet production in heavy-ion collisions with the ATLAS experiment

Author: Mgr. Radim Slovák

Institute: Institute of Particle and Nuclear Physics

Supervisor: Mgr. Martin Spousta, Ph.D., Institute of Particle and Nuclear Physics, Charles University

Abstract: This thesis presents two measurements - measurement of the jet fragmentation functions and inclusive jet production in heavy-ion collisions. The fragmentation functions are measured in Pb+Pb and *pp* collisions with the ATLAS detector at the LHC. The distributions are measured as a function of jet transverse momentum and rapidity. The analysis utilises an integrated luminosity of 0.14 nb^{-1} of Pb+Pb data and 4.0 pb^{-1} of *pp* data collected in 2011 and 2013, respectively, at the same centre-of-mass energy of 2.76 TeV. Modest but significant centrality-dependent modifications of fragmentation functions in Pb+Pb collisions with respect to those in *pp* collisions are seen. Measurements of the yield and nuclear modification factor, R_{AA}, for inclusive jets are performed using 25 pb^{-1} of *pp* data at $\sqrt{s} = 5.02$ TeV and 0.49 nb^{-1} of Pb+Pb data at $\sqrt{s_{\text{NN}}} = 5.02$ TeV. The jets are measured over the transverse momentum range of 100–1000 GeV in six rapidity intervals covering $|y| < 2.8$. The magnitude of the R_{AA} increases with increasing p_{T} and with decreasing centrality of the Pb+Pb collision. The R_{AA} is independent of rapidity at low p_{T} and it decreases with increasing rapidity at high p_{T}.

Keywords: jet quenching, fragmentation functions, nuclear modification factor, ATLAS detector

I would like to thank my supervisor Martin Spousta for his guidance, strong support and endless help as well as his friendly encouragements. I would like also to thank all my collaborators in ATLAS heavy-ion group, specially to my two close colleagues Laura Havener and Tomáš Kosek, for helping me in many aspects of my work. Last but not least, I wish to thank my grandmother, mother and my sister for supporting me and for giving me courage in this challenging period of my life.

Contents

Introduction

Heavy-ion collisions at ultra-relativistic energies produce a medium of strongly interacting nuclear matter composed of deconfined color charges that is commonly called a quark-gluon plasma (QGP) [1, 2, 3, 4]. Hard scattering processes occurring in these collisions produce high transverse momentum (p_{T}) partons that propagate through the medium and lose energy, resulting in the phenomenon of "jet quenching". Jet quenching refers, collectively, to a set of modifications of parton showers by the plasma through interactions of the constituents of the shower with the color charges in the plasma [5]. In particular, quarks and gluons in the shower may be elastically or inelastically scattered on the constituents of the plasma resulting in both deflection and energy loss of the constituents of the shower i.e. in the suppression of jet production and modification of the jet internal structure [6, 7, 8]. A complete characterization of the effects of jet quenching therefore requires measurements of both the jet fragmentation distributions and single jet suppression. The modified jet fragmentation was measured at the LHC and this thesis presents the latest precise measurement using the data collected by the ATLAS experiment [9, 10]. The inclusive jet suppression has also been previously measured at the LHC in terms of the nuclear modification factor [11, 12, 13]. This thesis presents a new measurement of the nuclear modification factor with the ATLAS experiment.

This thesis is divided into five chapters and it is organized as follows. In Chapter 1 there is a summary of the basic background of the theory needed for the understanding of the jet fragmentation and inclusive jet suppression measurement. Chapter 2 describes the LHC accelerator together with the ATLAS detector. A short description of CMS and ALICE detectors is presented as well. Chapter 3 provides a description of the jet reconstruction used at the LHC for run 1 and run 2. Chapter 4 and 5 describe the jet fragmentation measurement and inclusive jet suppression measurement, respectively. These are two analyses that were done with a significant contribution of the author of this thesis. To be more specific, author is one of two main analysers working on the jet fragmentation measurement. This work was done together with Tomáš Kosek who was responsible for the calculation of systematics uncertainties (Sec. 4.4), for the unfolding procedure (Sec. 4.5.3, 4.5.4) and for producing some of the final figures. Except that the rest of the analysis was done by the author of this thesis. The results of the jet fragmentation measurement were published by the European Physical Journal C (EPJC) [14]. For the inclusive jet suppression measurement, the preliminary results were obtained for XXVI international conference on ultrarelativistic heavy-ion collisions (Quark Matter 2017) [15] and the analysis is close to be finalized for the paper. Author of this thesis was one of two main analysers together with Laura Havener from Columbia University of New York. Her contribution was to provide a cross-check with author's result in the early stage of the analysis. Laura also did a significant contribution to the jet performance evaluation. In Chapter 6 there is a summary of the previous results on the jet fragmentation and inclusive jet suppression measurement at the LHC with conclusions following in the last chapter.

Additionally to the jet fragmentation and inclusive jet suppression measure-

ment, author contributed to evaluation of the jet trigger performance during Pb+Pb and p+Pb in run 2.

Selected publications of the author of the thesis:

- Slovák, R., Inclusive jet measurements in Pb+Pb collisions at 5 TeV with the ATLAS detector, ATLAS-PHYS-PROC-2017-004, accepted by Nuclear and Particle Physics Proceedings [16]
- ATLAS Collaboration, Study of inclusive jet yields in Pb+Pb collisions at $\sqrt{s_{\mathrm{NN}}} = 5.02$ TeV, ATLAS-CONF-2017-009 [15]
- Slovák, R., Jet Fragmentation in *pp*, p+Pb and Pb+Pb collisions at ATLAS detector, ATLAS-PHYS-PROC-2017-030, accepted by Nuclear Physics A [17]
- ATLAS Collaboration, Measurement of jet fragmentation in Pb+Pb and *pp* collisions at $\sqrt{s_{\mathrm{NN}}} = 2.76$ TeV with the ATLAS detector at the LHC, Eur. Phys. J., C77(6):379, 2017 [14]

1. Theoretical background

In this section we will provide introduction to the basics of Quantum chromodynamics (QCD), fragmentation functions and nuclear modification factor and some aspect of Heavy Ions (HI) collisions such as Glauber model, centrality of the heavy-ion collisions. A brief introduction into jets and jet quenching is also presented.

1.1 Fundamentals of QCD

An understanding of QCD is critical to modelling physics processes at the LHC since all physics starts from the collision of two protons or heavy-ion nuclei.

Quantum chromodynamics is the field theory that describes the strong nuclear force. The basic building blocks of QCD are quarks and gluons which carry color charge described by SU(3) non-Abelian gauge symmetry group. The half spin quark fields, ψ_a, transform under the rotation in color space as [18]:

$$\psi_a^{'}(x) = e^{i\phi^C(x)t_{ab}^C}\psi_b(x) = U_{ab}(x)\psi_b(x)\,, \tag{1.1}$$

where the subscripts a and b describe the quark color (a, $b = 1, 2, 3$) and $\phi^C(x)$, $C = 1, \cdots, 8$ are functions of x. The generators of the gauge group, t_{ab}^C, can be represented eight 3×3 matrices that obey the Lie Algebra

$$[t_{ab}^A, t_{ab}^B] = if^{ABC}t_{ab}^C\,, \tag{1.2}$$

where f^{ABC} are real constants, called the structure constants of the SU(3) group.

To impose SU(3) local gauge invariance on the usual Dirac Lagrangian, the derivatives have to be replaced by gauge-covariant derivative D_μ:

$$D_{\mu,ab} = \partial_\mu\delta_{ab} - igt_{ab}^C A_\mu^C\,. \tag{1.3}$$

The covariant derivative introduces a non-Abelian coupling of strength g between quarks and gluons, represented by spin-1, massless gauge fields A_μ^a. The constant g can be expressed via strong coupling constant α_{S} as:

$$g = \sqrt{4\pi\alpha_{\mathrm{S}}}. \tag{1.4}$$

Constant α_{S} (or g) plays a critical role in determining the rates of physical processes (e.g. particle decay rates, production rates, or scattering rates).

The full Lagrangian of QCD can be written as:

$$\mathcal{L}_{\mathrm{QCD}} = \sum_q \overline{\psi}_q\left(i\gamma^\mu D_\mu - m_q\right)\psi_q - \frac{1}{4}F_{\mu\nu}^A F^{A,\mu\nu}\,, \tag{1.5}$$

where the index q labels a quark of a given flavour and mass m_q. The field strength tensor $F_{\mu\nu}^A$ is defined as:

$$F_{\mu\nu}^A = \partial_\mu A_\nu^A - \partial_\nu A_\mu^A - gf^{ABC}A_\mu^B A_\nu^C. \tag{1.6}$$

From (1.5) all possible interactions can be determined. One of them is the quark-gluon vertex corresponding to $gA\overline{\psi}\psi$ term. The second is three gluon vertex

represented by $gAA\partial A$ and the third 4-gluon vertex represented by g^2AAAA term. These vertices are shown in Fig. 1.1.

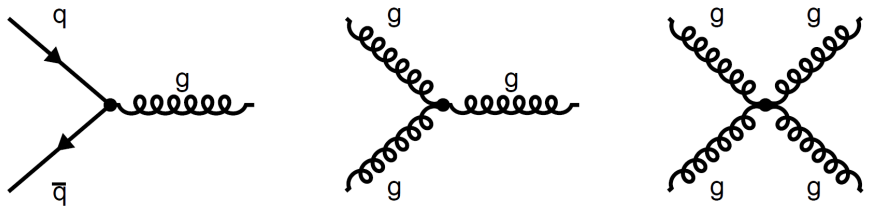

Figure 1.1: Three possible diagrams allowed by QCD Lagrangian. The curl lines represent gluons and the solid lines represent quarks. The quark-gluon (left) vertex and three gluon vertex (middle) are proportional to g. The four gluon vertex (right) is proportional to g^2.

Because of the appearance of the divergent terms from integrating over large momenta of virtual particles in quantum loops, the renormalization procedure is necessary. The magnitude of the α_{S} depends generally on a momentum scale μ called renormalization scale. The derivative of coupling constant with respect to the renormalization scale μ is defined by the β-function:

$$\frac{\partial \alpha_{\mathrm{S}}(\mu)}{\partial \ln \mu} = \beta\left(\alpha_{\mathrm{S}}\right). \tag{1.7}$$

The running constant α_{S} can be expressed in the following renormalization group equation:

$$\beta\left(\alpha_{\mathrm{S}}\right) = \mu^2 \frac{\partial \alpha_{\mathrm{S}}}{\partial \mu^2} = -\alpha_{\mathrm{S}}^2\left(b_0 + \alpha_{\mathrm{S}} b_1 + \cdots\right). \tag{1.8}$$

Wilczek, Gross and Politzer [19, 20] computed the one-loop β-function for SU(3) non-Abelian gauge theories which gives the leading order contributions to 1.8. The term b_0 is:

$$b_0 = \frac{1}{12\pi}\left(11N_c - 2n_f\right), \tag{1.9}$$

where N_c is the number of colors and n_f is the number of quark flavours. The second term b_1 in (1.8) is [21]

$$b_1 = \frac{1}{24\pi^2}\left(17N_c^2 - 19n_f\right). \tag{1.10}$$

The other terms are dependent on the renormalization scheme [1] and are more complicated, see e.g. [21].

The solution of Eq. (1.7) for one-loop β-function is:

$$\alpha_{\mathrm{S}}\left(\mu\right) = \frac{\alpha_{\mathrm{S}}\left(\mu_0\right)}{1 + b_0 \alpha_{\mathrm{S}}\left(\mu_0\right) \ln\left(\dfrac{\mu^2}{\mu_0^2}\right)}. \tag{1.11}$$

[1] The term b_1 for quarks with non-zero mass is also dependent on the renormalization scheme.

The equation (1.11) can be also rewritten as follows:

$$\alpha_S(\mu) = \frac{1}{b_0 \ln \frac{\mu^2}{\Lambda^2_{QCD}}}, \tag{1.12}$$

where $\Lambda_{QCD} \approx 200 - 400$ MeV is the Landau pole where the coupling constant will be infinite at the leading order (LO) and perturbative calculations cannot be used.

From equation (1.9), it is clear that b_0 is positive and therefore the coupling constant α_S decreases with increasing μ. QCD has two unique properties that give rise to important behaviour of the strong interaction. One property is called confinement, which guaranties that all observable states are color singlets mesons and baryons. A consequence of the confinement is that free quarks and gluons are unobservable. The second property is called asymptotic freedom, which guaranties that quarks and gluons behave as free particles when the interaction energy increases.

The measured dependence of the coupling constant on the energy scale is shown in Fig. 1.2. Asymptotic freedom at large μ as well as the rise leading to confinement at small μ can be observed. The coupling constant is usually expressed for $\mu = m_Z^2$. The latest value is estimated to be [21]:

$$\alpha_S\left(m_Z^2\right) = 0.1181 \pm 0.0011 \tag{1.13}$$

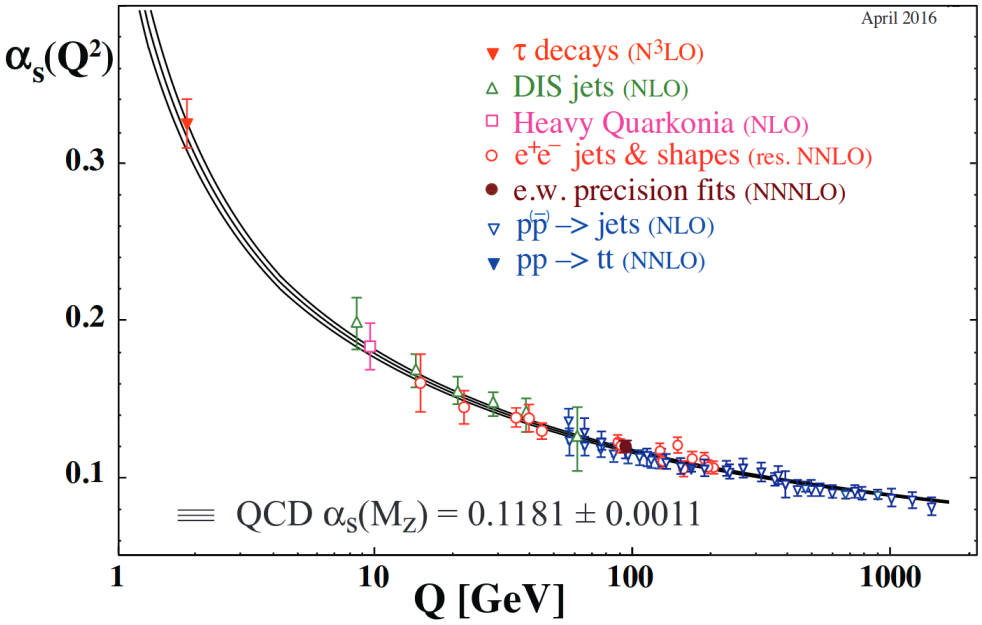

Figure 1.2: Summary of measurements of α_S as a function of the energy scale $\sqrt{Q^2} \equiv \mu \equiv \sqrt{\mu^2}$. The respective degree of QCD perturbation theory used in the extraction of α_S is indicated in brackets (NLO: next-to-leading order; NNLO: next-to-next-to leading order; res. NNLO: NNLO matched with resummed next-to-leading logs; N3LO:next-to-NNLO). Figure taken form [21].

The cross-section for inclusive hadron production at high p_{T} can be factorized as:

$$\mathrm{d}\sigma_{A+B\to h+X} = \sum_{a,b,c,d} \int f_{a/A}(x_a,\mu_f) f_{b/B}(x_b,\mu_f) \mathrm{d}\sigma_{ab\to cd}(\mu_R) D_c^h(z,\mu_F) \mathrm{d}x_a \mathrm{d}x_b \mathrm{d}z \tag{1.14}$$

where $f_{a/A}(x_a,\mu_f)$ and $f_{b/B}(x_b,\mu_f)$ are parton distribution functions (PDF) which express the probability that hadron A and B contains parton a and b carrying the initial momentum fraction $x_a = p_a/P_A$ and $x_b = p_b/P_B$, respectively. $D_c^h(z,\mu_F)$ is the fragmentation function describing a probability for a fragmentation of a parton c to hadron h (for more details see Sec. 1.6) and $\sigma_{ab\to cd}(\mu_R)$ is the elementary partonic cross-section. The Eq. (1.14) contains factorization scales μ_f and μ_F at which the hard perturbative process is separated from the non-perturbative initial state and final state evolution. μ_R is the renormalisation scale. These scales are usually taken to be the same $\mu_f = \mu_F = \mu_R = \sqrt{Q}$ where Q is the momentum scale. The fragmentation functions and parton distribution functions are universal but non-perturbative. Meaning it is not possible to calculate them from the first principles but it is possible to determine their scale dependence using the Dokshitzer-Gribov-Lipatov-Altarelli-Parisi (DGLAP) evolution equations [22, 23, 24]:

$$\frac{\mathrm{d}f_q(x,\mu)}{\mathrm{d}\ln\mu} = \frac{\alpha_{\mathrm{S}}(\mu^2)}{2\pi} \int_x^1 \frac{\mathrm{d}y}{y} \left(f_q(y,\mu) P_{qq}\left(\frac{x}{y}\right) + f_g(y,\mu) P_{qg}\left(\frac{x}{y}\right) \right) \tag{1.15}$$

$$\frac{\mathrm{d}f_g(x,\mu)}{\mathrm{d}\ln\mu} = \frac{\alpha_{\mathrm{S}}(\mu^2)}{2\pi} \int_x^1 \frac{\mathrm{d}y}{y} \left(\sum_{i=1}^{n_f} \left(f_q^i(y,\mu) + \overline{f}_q^i(y,\mu) \right) P_{gq}\left(\frac{x}{y}\right) + f_g(y,\mu) P_{gg}\left(\frac{x}{y}\right) \right) \tag{1.16}$$

The Eqs. (1.15) and (1.16) are the DGLAP evolution equation in the leading order (LO) for the quark distribution function, $f_q(x,\mu)$, and gluon distribution function, $f_g(x,\mu)$. $P_{ab}(x/y)$ are the splitting functions for parton b with momentum fraction y splitting into parton a with momentum fraction x.

1.2 Jets and jet finding algorithms

Jets are collimated bunches of hadrons, electrons and photons which are the result of the fragmentation of the original energy which was produced in the hard scattering. A jet can be roughly characterized by the opening angle $R = \sqrt{\Delta\phi^2 + \Delta\eta^2}$ defining a cone around the jet axis where the most of the energy is deposited. Here ϕ and η are azimuthal angel and pseudorapidity, respectively.

More accurate definitions involve jet finding algorithm [25, 26, 27, 28].

Many jet algorithms are based on association of objects that are nearby in angle. These are also called cone algorithms. Many of them were unsatisfactory because of the infrared and collinear (IRC) unsafety. For example the final number of reconstructed jets must not be changed due to splitting of a given parton or adding a soft gluon.

To avoid these problems, sequential clustering algorithms were introduced. They are based on association of energy deposited in calorimeters and are IRC safe. A basic description of these algorithms is stated here. Sequential clustering algorithms measure the distance between pair of objects (particles, clusters, calorimetric towers) and decide which objects should be clustered together and when should be the clustering terminated. The spatial distance, R_{ij}, between object i and j is defined as

$$\Delta R_{ij}^2 = (y_i - y_j)^2 + (\phi_i - \phi_j)^2 \tag{1.17}$$

where y and ϕ are particles' rapidity and azimuthal angle, respectively.

For each pair of objects i and j algorithm evaluates the p_{T}-weighted distance:

$$d_{ij} = \min(p_{\mathrm{T}i}^{2p}, p_{\mathrm{T}j}^{2p}) \frac{\Delta R_{ij}^2}{R^2} \tag{1.18}$$

where R is the jet size parameter.

For $p = -1$ the jet algorithm is called anti-k_t algorithm [27], while $p = 1$ corresponds to the k_t [26] and $p = 0$ to the Cambridge-Aachen algorithm [28]. The k_t algorithm clusters jets from soft objects and complete them with the hard jet signal while the anti-k_t algorithm clusters hard objects first ending with cone like jets. The Cambridge-Aachen algorithm uses for object clustering only geometric consideration.

The sequential clustering algorithms work as follows:

- Calculate d_{ij} for each pair of objects i and j, also calculate the beam distance $d_{iB} = p_{\mathrm{T}i}^{2p}$.
- Find such objects i and j with the minimum distances d_{ij} and d_{iB}.
- If the minimum is a d_{ij}, combine objects i and j together and start over from the beginning.
- If the minimum is a d_{iB}, the corresponding jet i is stated as a final-state jet and it is removed from subsequent clustering.
- Finish clustering when no particles remain.

1.3 Jet quenching

The hot and dense medium called quark-gluon plasma (QGP) is created in the heavy-ion collisions. Jets are a powerful tool to study the QGP via the phenomenon called "jet quenching". The jet quenching most generally refers to modification of jet yields and jet properties, which is a consequence of the parton energy loss in the hot and dense plasma. It is important to study this interaction because it should provide a key insight into the properties of the decomfined medium.

The relativistic heavy-ion collisions were studied at the Alternating Gradient Synchrotron (AGS), $\sqrt{s_{\mathrm{NN}}} \leq 5$ GeV, at the CERN Super Proton Synchrotron (SPS), $\sqrt{s_{\mathrm{NN}}} \leq 20$ GeV, the Brookhaven Relativistic Heavy Ion Collider (RHIC), $\sqrt{s_{\mathrm{NN}}} \leq 200$ GeV, and at the Large Hadron Collider (LHC) at CERN, $\sqrt{s_{\mathrm{NN}}} \leq$

5.5 TeV. One of the most significant jet quenching observation at RHIC was the strong suppression of the inclusive hadron yields [29] in Au+Au collisions and the change in the rate of azimuthally back-to-back hadron pairs in the heavy-ion relative to *pp* and d+Au collisions [30].

The difference between heavy-ion collisions and *pp* collisions is often expressed in terms of the nuclear modification factor, $R_{\rm AA}$, which is a ratio of the yield in the heavy-ion collisions to a cross-section in *pp* collisions which is scaled to account for multiple nucleon-nucleon collisions occurring in a heavy-ion collisions (details can be found in Sec. 1.7). Fig. 1.3 demonstrates the experimental results from PHENIX and STAR experiments. The left panel shows the central to peripheral ratio of the inclusive hadron production, $R_{\rm CP}$, for Au+Au collisions [29] measured by PHENIX collaboration where a clear suppression of the inclusive hadron yields in central collisions can be observed. The right panel of Fig. 1.3 shows the STAR experiment results on the high $p_{\rm T}$ dihadron azimuthal angle measurement, $\Delta\phi$ [30].

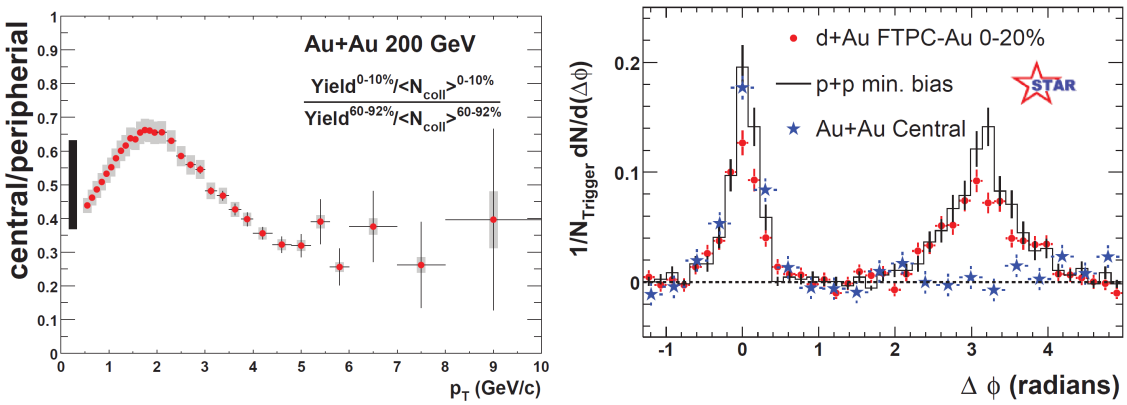

Figure 1.3: Left: $R_{\rm CP}$ for Au+Au collisions as a function of the transverse momentum measured by PHENIX experiment [29]. Right: Azimuthal correlations of dihadrons for different collisions systems: *pp*, d+Au and Au+Au by STAR experiment [30].

It was observed in *pp*, d+Au and Au+Au collisions that hadrons from a single jet generate an enhanced correlation at $\Delta\phi \simeq 0$. That is around the highest $p_{\rm T}$ hadron which is used to trigger events. Hadrons from the other jet in the dijet system should generate an enhanced correlation at $\Delta\phi \simeq \pi$. That was measured in *pp* and d+Au collisions but not in Au+Au collisions. This is a model independent measurement which suggests that the suppression is because of the final state interaction. Other important results from PHENIX [31] and STAR [32] experiments can be found in Refs. [33, 34, 35, 36, 37].

It was first suggested by Bjorken [38] that jets could be a suitable tool to study the quark gluon plasma. He suggested that if the two partons have a different path length in the medium, the back-to-back jets would be sensitive to differential energy loss of partons propagating through the dense QCD medium. It could also happen in the extreme cases that one jet deposits all of its energy in the medium while its highly energetic partner will survive. Bjorken's energy loss per path length, $\mathrm{d}E/\mathrm{d}x$, was estimated based on the elastic collisions of high momentum partons with the medium constituents [38] resulting in an ionization-like energy

loss:

$$\frac{\mathrm{d}E}{\mathrm{d}x} = C_{\mathrm{R}}\pi g^2 T^2 \left(1 + \frac{N_f}{6}\right) \ln \frac{4ET}{m_{\mathrm{D}}^2}, \tag{1.19}$$

where C_{R} is the color factor equals to 3 for gluons or 4/3 for quarks. T is the plasma temperature, N_f is the number of quarks flavours, g is the coupling parameter and the Debye screening mass, m_{D}, is defined as:

$$m_{\mathrm{D}} = \left(1 + \frac{N_f}{6}\right) g^2 T^2. \tag{1.20}$$

It was found later that the another important source of the parton energy loss is the gluon radiation ("gluonstrahlung") [39] which is similar to the bremstrahlung process in QED. Hard scattered parton can radiate and scatter off gluons on its path through the medium. These gluons may further interact with the medium as illustrated in Fig. 1.4.

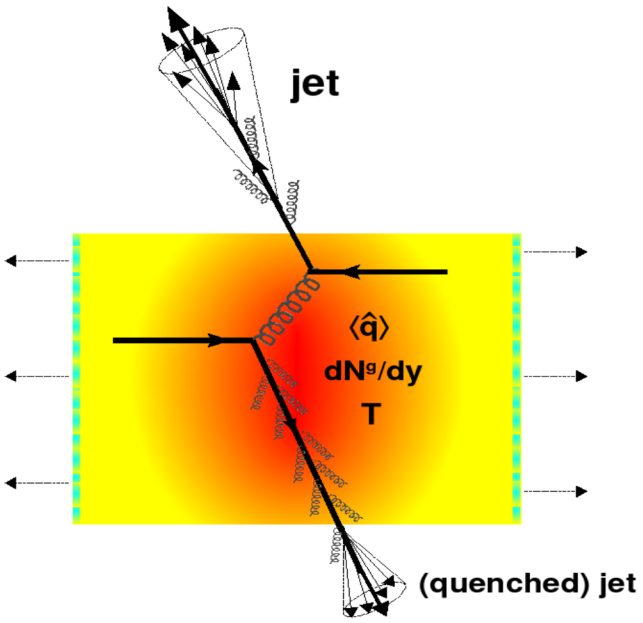

Figure 1.4: Illustration of the jet quenching phenomenon. From the hard scattering of two quarks, two highly energetic partons are produced that radiate gluons when propagating through the hot dense medium. In this cartoon, one jet suffers energy loss by the "gluonstrahlung" and fragments outside the medium. His partner goes directly to the vacuum and fragments into an unquenched jet.

To describe this processes, it is useful to introduce following independent quantities [40]:

- forward jet energy, E,
- the Debye mass, defined in Eq. (1.20),
- the mean free path $\lambda = 1/(\sigma\rho)$ where σ is the integrated cross-section of the particle-medium interaction and ρ is the medium density,

- the opacity or geometrical thickness of the medium $N = L/\lambda$ which is the number of scatterings experienced by a particle propagating though the medium of thickness L,
- the transport coefficient $\widehat{q} = \mu^2/\lambda$ is the transverse momentum squared transferred to the traversing particle per unit path length,
- the virtuality of the initial parton Q^2,
- the energy of emitted gluon, ω.

In the case of thin media $L \ll \lambda$, the analogue of Landau Pomeranchuk Migdal (LPM) effect [41, 42] known from QED is causing the suppression of gluonstrahlung spectrum due to coherence effects. The QCD analog of LPM effect was introduced in work of Baier, Dokshitzer, Mueller, Peigne, Schiff (BDMPS), [43] and independently in the work by Zakharov [44] and it was found to be an important mechanism for the jet quenching [45, 46]. In this regime, the QCD radiative energy loss, E_{rad}^{LPM}, grows quadratically with path length in the medium L as:

$$\Delta E_{rad}^{LPM} \approx \alpha_{\mathrm{S}} C_{\mathrm{R}} \begin{cases} \widehat{q}L^2 & \text{if } \omega < \omega_{\mathrm{C}} \\ \widehat{q}L^2 \ln(E/\widehat{q}L^2) & \text{if } \omega > \omega_{\mathrm{C}} \end{cases} \tag{1.21}$$

where ω_{C} is the average energy loss. Not quantified in the formula (1.21) is the energy loss of heavy quarks for which the emission of gluons is suppressed at small angles due to the dead cone effect [47]. One can also see in Eq. (1.21) that the energy loss, ΔE_{rad}^{LPM}, is independent of initial parton energy, E, if $\omega < \omega_{\mathrm{C}}$. The energy loss of quark is smaller then the energy loss of gluons because of the color factor C_{R}.

The energy loss, defined in Eq. (1.21), presents an idealistic situation. Because the reality is far more complex, different phenomenological approaches were developed to study radiative processes in the medium. Models are usually identified after names of their authors [7]. Here we will shortly describe main models. Already mentioned was BDMPS-Z model. Other models are Armesto, Salgado, Wiedemann (ASW) model [48, 49], Gyulassy, Levai, Vitev (GLV) model [50, 51], Luo, Qiu, Sterman called Higher Twist (HT) model [52, 53, 54, 55, 56] and Arnold, Moore, Yaffe (AMY) model [57, 58, 59]. We will discuss only the basic ideas of those models here. All four models calculate the single gluon emission, the differential radiation spectra and the energy loss of partons is calculated in the fragmentation process. BDMPS-Z and ASW models are very similar. The "gluonstrahlung" can be formulated using a path integral that takes into account the scatterings on multiple soft static cattering centers. The radiated gluons modify the fragmentation functions. In the GLV model, the opacity expansion was developed. It is similar to BDMPS-Z and ASW approaches but the GLV begins with expanding single hard radiation. In the finite temperature field approach which is used in AMY, the fragmentation functions are computed directly, similarly as in the case of the HT model. In AMY model, medium modified fragmentation functions are calculated as a convolution of vacuum fragmentation functions and hard radiated partons. HT uses modified splitting functions to obtain the medium-modified fragmentation function. Therefore, the HT approach is similar to DGLAP formalism.

To simulate the real events, Monte Carlo (MC) generators were developed. All of the MC generators which simulate the jet quenching use modification of PYTHIA [60]. In particular parton shower algorithm in PYTHIA is altered. The most common jet quenching MC generators are PYQUEN [61], Q-PYTHIA [62] and JAWEL [63].

1.4 Glauber model

The basic experimental observation in heavy-ion collisions is a presence of large multiplicity of charged particles. When colliding two nuclei in their centre-of-mass system, two Lorentz contracted "pancakes" of nuclear matter collide at the impact parameter **b**. Impact parameter quantifies the distance between two centres of the nuclei in the transverse plane of the collision, as shown in Fig. 1.5. Small values of the impact parameter correspond to a large overlap of nuclei in the transverse plane. These are so called central collisions where one can observe very large multiplicities. Large values of the impact parameter correspond to a small overlap of nuclei. These are so called peripheral collisions where the multiplicities are small, e.g. close to high-intensity (pile-up) *pp* collisions.

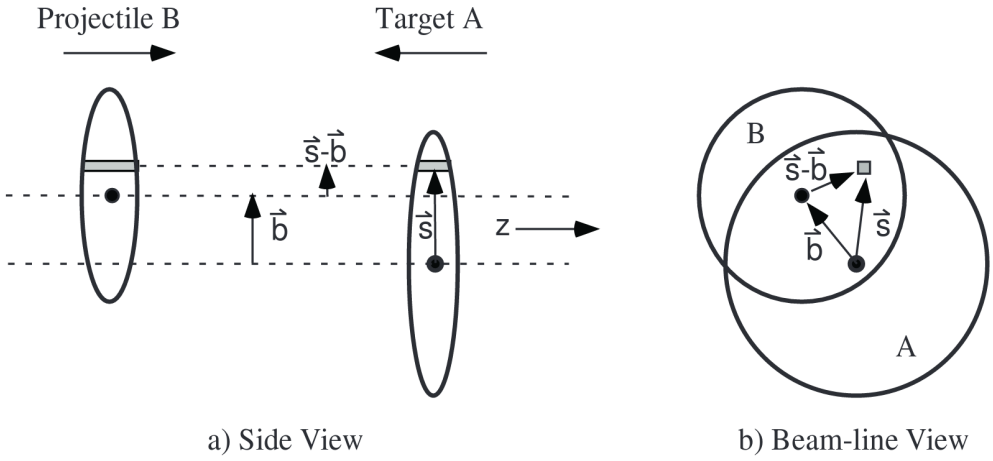

Figure 1.5: Schematic view of a nucleus-nucleus collision described in terms of the impact parameter b in the longitudinal (left) and transverse (right) plane. Figure adapted from Ref. [64].

The process of a nucleus-nucleus collision can be described with a phenomenological description starting from the geometrical configuration of the nuclei which is called Glauber model [65, 64]. It is based on a superposition of independent nucleon-nucleon interactions. In such a model, nuclei are composed of a set of nucleons, and the nuclear reaction is approximated by successive independent nucleon-nucleon interactions assuming the nucleons travel in a straight line along the beam axis and that nucleons are smoothly distributed in the nucleus. Eq. 1.22 describes Woods-Saxon distribution [66] that is often used for description of the nucleon density $\rho(r)$:

$$\rho(r) = \frac{\rho_0}{1 + e^{(r-R)/a}} \ , \tag{1.22}$$

where a is the skin thickness and R is the radius of nucleus with N nucleons defined as $R = R_0 N^{1/3}$ with constant $R_0 = 1.18$ fm. The constant ρ_0 is an overall normalization factor ensuring the distribution is normalized to the number of nucleons. For Pb^{208} these parameters are $R = 6.62 \pm 0.06$ fm, $a = 0.55 \pm 0.01$ fm [67].

The nuclear profile function, $T_{\mathrm{A}}(\mathbf{s})$, which is a key quantity in the Glauber model, depends on the distance $\mathbf{s}$ from the center of the nucleus A in the transverse plane and describes the profile of nucleus in the plane perpendicular to the beam axis z. It is defined as:

$$T_{\mathrm{A}}(\mathbf{s}) = \int \rho_{\mathrm{A}}(\mathbf{s}, z)\mathrm{d}z. \tag{1.23}$$

which is the number of nucleons per unit area along a direction z with ρ_{A} being the nuclear density distribution of nucleus A.

The probability of interaction of two incoming nucleons inside two nuclei with mass number A and B and with the impact factor b can be written as $T_{\mathrm{AB}}(\mathbf{b})\sigma^{\mathrm{NN}}$ where σ^{NN} is the nucleon-nucleon inelastic cross section and $T_{\mathrm{AB}}(\mathbf{b})$ is the normalized overlap function defined as:

$$T_{\mathrm{AB}}(\mathbf{b}) = \int T_{\mathrm{A}}(\mathbf{s})T_{\mathrm{B}}(\mathbf{s} - \mathbf{b})\mathrm{d}s. \tag{1.24}$$

When taken into account the independent nucleon-nucleon collisions, the probability for the occurrence of n inelastic collisions for an impact parameter $\mathbf{b}$ is then:

$$P(n, \mathbf{b}) = \binom{AB}{n} \left[T_{\mathrm{AB}}(\mathbf{b})\sigma^{\mathrm{NN}}\right]^n \left[1 - T_{\mathrm{AB}}(\mathbf{b})\sigma^{\mathrm{NN}}\right]^{AB-n}. \tag{1.25}$$

The total probability of an inelastic event in the collision of A and B is then:

$$\frac{\mathrm{d}\sigma^{\mathrm{A+B}}}{\mathrm{d}b} = \sum_{n=1}^{AB} P(n, \mathbf{b}) = 1 - \left[1 - T_{\mathrm{AB}}(\mathbf{b})\sigma^{\mathrm{NN}}\right]^{AB}. \tag{1.26}$$

From this equation it is possible to estimate the average number of binary nucleon-nucleon collisions N_{coll} as a function of the impact parameter. N_{coll} can be calculated as the mean value of the binomial distribution $P(n, \mathbf{b})$:

$$N_{\mathrm{coll}}(\mathbf{b}) = \sum_{n=1}^{AB} nP(n, \mathbf{b}) = ABT_{\mathrm{AB}}(\mathbf{b})\sigma^{\mathrm{NN}}. \tag{1.27}$$

The number of participants, N_{part}, is the number of protons or neutrons from the nuclei that undergo an inelastic collision when two nuclei pass each other. N_{part} can be expressed as a function of the impact parameter $\mathbf{b}$ as:

$$\begin{aligned} N_{\mathrm{part}}(\mathbf{b}) = A \int T_{\mathrm{A}}(\mathbf{s}) \left\{1 - \left[1 - T_{\mathrm{B}}(\mathbf{s\text{-}b})\sigma^{\mathrm{NN}}\right]^B\right\} \mathrm{d}^2 s + \\ B \int T_{\mathrm{B}}(\mathbf{s\text{-}b}) \left\{1 - \left[1 - T_{\mathrm{A}}(\mathbf{s})\sigma^{\mathrm{NN}}\right]^A\right\} \mathrm{d}^2 s \end{aligned} \tag{1.28}$$

Nuclear overlap function for the identical nuclei, T_{AA}, can be obtained from the inelastic proton-proton (pp) cross-section using number of binary collisions N_{coll} as:

$$T_{\mathrm{AA}} = \frac{N_{\mathrm{coll}}}{\sigma_{pp}}. \tag{1.29}$$

1.5 Centrality of Heavy Ions collision

Experimentally, different amount of geometrical overlap of the nucleon-nucleon collisions determine different level of overall event activity or "centrality" of heavy-ion collisions. Because the direct measurement of the impact parameter is not possible, the centrality can be characterized using the total transverse energy, $\Sigma E_{\mathrm{T}}^{\mathrm{FCal}}$, at the electromagnetic scale deposited in the forward calorimetres. The pseudorapidity coverage of this system is $3.2 < |\eta| < 4.9$ which is well separated from the central region of the detector, meaning that hard processes such as the jet production will have a minimal impact on the centrality determination. This is demonstrated in the left panel of Fig. 1.6. The $\Sigma E_{\mathrm{T}}^{\mathrm{FCal}}$ distribution can be divided into percentiles of the total inelastic cross-section for Pb+Pb collisions, see the right panel of Fig. 1.6. The first percentile, 0–10%, represents the 10% of collisions that have the largest overlap implying that there is the largest event activity in such collisions. The last percentile, 90–100%, represents the 10% of collisions that are the most peripheral implying that there is the smallest event activity in such collisions. Another quantity to characterize the centrality is the number of participating nucleons N_{part}. Number of participating nucleons is defined using the geometrical model of heavy-ion collisions called Glauber model, see Sec. 1.4. The relation between the centrality and number of participating nucleons is obtained by running the Glauber Monte Carlo tool [64].

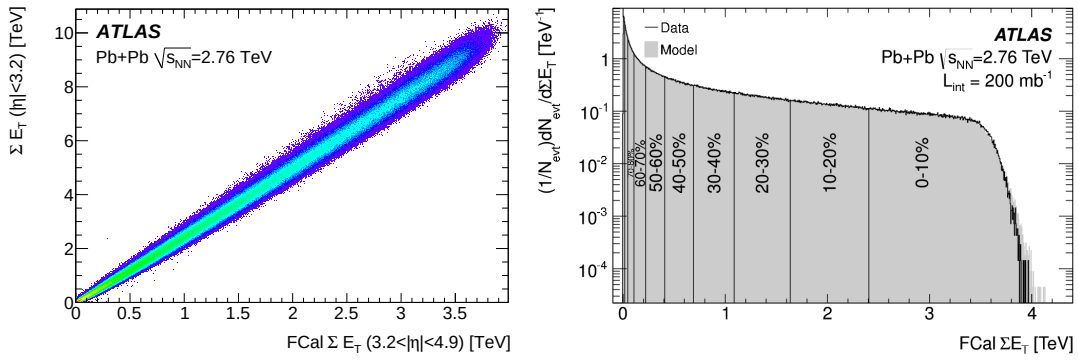

Figure 1.6: Left: Correlation of uncorrected $\sum E_{\mathrm{T}}$ in the electromagnetic barrel ($|\eta| < 1.475$) with the FCAL detector ($3.1 < |\eta| < 4.9$) [68]. Right: Measured $\Sigma E_{\mathrm{T}}^{\mathrm{FCal}}$ distribution divided into 10% centrality intervals [69]. Both measurement were done with Pb+Pb $\sqrt{s_{\mathrm{NN}}} = 2.76$ TeV.

1.6 Fragmentation functions

The fragmentation function $D_{i/h}(z, \mu^2)$ express the probability for a hadron i to carry a fraction z of the momentum of outgoing parton h. Generally, the fragmentation functions describe how the color-carrying quarks and gluons transform into color-neutral particles. Beyond the leading order (LO) of perturbative QCD, fragmentation functions are factorization-scheme dependent, and in quark-parton model they obey the momentum sum rule and probability conservation [21]:

$$\sum_h \int_0^1 z D_{i/h}(z, \mu^2) \mathrm{d}z = 1 \tag{1.30}$$

$$\sum_q \int_{z_{min}}^1 \left[D_{i/h}(z, \mu^2) + D_{\bar{i}/h}(z, \mu^2) \right] \mathrm{d}z = n_h \tag{1.31}$$

where $z_{min} = 2m_h/Q$ is the threshold energy for producing a hadron of mass m_h and n_h is the average multiplicity of hadrons h. The momentum sum rule (1.30) expresses that the sum of the energies of all hadrons is the energy of the parent quark. The probability conservation (1.31) states that the number n_h for hadrons h is given by the sum of probabilities of obtaining hadron h from all possible parents (quarks or anti-quarks of any flavour).

The quantities that are later used in jet fragmentation measurement in Sec. 4 were introduced in Ref. [9], namely the jet fragmentation functions, $D(z)$, and transverse momentum distribution of the charged particles found inside the jet, $D(p_\mathrm{T})$. The $D(z)$ distributions are defined as

$$D(z) \equiv \frac{1}{N_\mathrm{jet}} \frac{\mathrm{d}N_\mathrm{ch}}{\mathrm{d}z}, \tag{1.32}$$

where N_jet is the total number of jets, N_ch is number of charged particles associated with a jet, and where the longitudinal momentum fraction z is defined as

$$z \equiv \frac{p_\mathrm{T}}{p_\mathrm{T}^\mathrm{jet}} \cos \Delta R = \frac{p_\mathrm{T}}{p_\mathrm{T}^\mathrm{jet}} \cos \sqrt{\Delta y^2 + \Delta \phi^2}. \tag{1.33}$$

Here p_T stands for the transverse momentum of a charged particle, Δy and $\Delta \phi$ are the distances between the jet axis and the charged particle position in rapidity and azimuth, respectively. A cartoon elucidating the definitions used here is shown in Fig. 1.7.

The $D(p_\mathrm{T})$ distributions which are often used as a complementary tool to study the jet structure are defined as

$$D(p_\mathrm{T}) \equiv \frac{1}{N_\mathrm{jet}} \frac{\mathrm{d}N_\mathrm{ch}(p_\mathrm{T})}{\mathrm{d}p_\mathrm{T}}. \tag{1.34}$$

1.7 Nuclear modification factor

As shown in many previous studies at the LHC the modification of yields of hadrons in Pb+Pb collisions depends on the centrality of the collision. Measurements of the modification of observables as a function of collision centrality can provide insight into the mechanism of the jet quenching. Generally, the energy

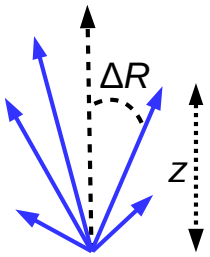

Figure 1.7: A cartoon illustrating the definition of variables used in this thesis. The dashed arrow is the direction of the jet axis. Blue arrows are the directions of particles. The length of blue arrows reflects the p_{T} of particles.

loss of partons traversing QGP will result in a systematic reduction in the yield of hadrons at fixed p_{T}. Thus, the hard scattering rates are suppressed in central collisions relative to peripheral or proton-proton (pp) collisions as measured previously in Refs. [11, 12].

Central collisions receive an enhancement in hard scattering rate due to the larger geometric overlap between the colliding nuclei, resulting in a larger per-collision nucleon-nucleon luminosity. The centrality dependence of measured hard scattering rates must therefore be normalized by a factor, nuclear overlap function, T_{AA}, that accounts for this geometric enhancement to allow a proper assessment of the quenching effects. Such an assessment is quantified by the nuclear modification factor, R_{AA}, defined as:

$$R_{\mathrm{AA}} = \frac{\frac{1}{N_{\mathrm{evt}}^{\mathrm{tot}} T_{\mathrm{AA}}} \left.\frac{\mathrm{d}^2 N_{\mathrm{HI}}}{\mathrm{d}p_{\mathrm{T}}\mathrm{d}y}\right|_{\mathrm{cent}}}{\left.\frac{\mathrm{d}^2\sigma_{pp}}{\mathrm{d}p_{\mathrm{T}}\mathrm{d}y}\right|_{pp}}, \tag{1.35}$$

where N_{evt} is number of events is heavy-ion (HI) collisions, $\mathrm{d}^2 N_{\mathrm{jet}}/\mathrm{d}p_{\mathrm{T}}\mathrm{d}y|_{\mathrm{cent}}$ is the differential yield for the jet production in HI collisions of a given centrality, $\mathrm{d}^2\sigma_{\mathrm{jet}}/\mathrm{d}p_{\mathrm{T}}\mathrm{d}y|_{pp}$ is the differential cross section for the jet production in pp collisions. In the case of the absence of jet quenching effect, the R_{AA} would be unity.

The modification of yields in Pb+Pb collisions can be also alternatively studied using the central-to-peripheral nuclear modification factor, R_{CP}:

$$R_{\mathrm{CP}} = \frac{T_{\mathrm{AA}}|_{\mathrm{perip}}}{T_{\mathrm{AA}}|_{\mathrm{cent}}} \frac{(1/N_{\mathrm{evt}}\mathrm{d}^2 N_{\mathrm{jet}}/\mathrm{d}p_{\mathrm{T}}\mathrm{d}y)\,|_{\mathrm{cent}}}{(1/N_{\mathrm{evt}}\mathrm{d}^2 N_{\mathrm{jet}}/\mathrm{d}p_{\mathrm{T}}\mathrm{d}y)\,|_{\mathrm{perip}}}, \tag{1.36}$$

where $(1/N_{\mathrm{evt}}\mathrm{d}^2 N_{\mathrm{jet}}/\mathrm{d}p_{\mathrm{T}}\mathrm{d}y)$ is differential per event yield in HI collisions. $T_{\mathrm{AA}}|_{\mathrm{cent}}$ and $T_{\mathrm{AA}}|_{\mathrm{perip}}$ are nuclear overlap functions for central and peripheral events, respectively.

The disadvantage of R_{CP} is that if the peripheral collisions contain nuclear effects the modification could be suppressed. R_{CP} is usually used when the pp reference is not available.

2. Experimental setup

In the first section of this chapter we will provide a short description of the Large Hadron Collider (LHC) located at Conseil Européen pour le Recherche Nucléaire (CERN) close to Geneva, Switzerland. Next section is dedicated to the ATLAS detector together with all its important subcomponents. A short description of CMS and ALICE detectors is presented in the last section of this thesis.

2.1 The Large Hadron Collider

The Large Hadron Collider [70] is the world's largest particle accelerator with the circumference around 27 km located in the same tunnel (buried approximately 175 m underground) where the Large Electron-Positron Collider (LEP) was installed. It consists of the parallel beam lines circulating particles in opposite directions, colliding at designated interaction points. There are used 1232 dipole magnets bending the particles trajectories, 392 quadrupoles to keep the beam focused, 2464 sextupoles and approximately 2500 other magnets, such as octupoles or decapoles.

The designed instantaneous luminosity for protons is 10^{34} cm^{-2}s^{-1} and for heavy-ions it is 10^{27} cm^{-2}s^{-1} [71]. The beam is made up from maximal 2808 bunches of protons with bunch spacing no less then 25 ns. For lead ions, the number of bunches is no more then 356.

It was primary designed to collide protons at center of mass energy up to $\sqrt{s} = 14$ TeV but the machine is capable of colliding heavy ions Pb^{82+} at the corresponding center of mass energy per nucleon, $\sqrt{s_{NN}} = 82/208 \cdot 14$ TeV $= 5.52$ TeV, as well. The LHC can also accelerate and collide proton with lead ions. The processes to accelerate protons and ion consists in different steps that

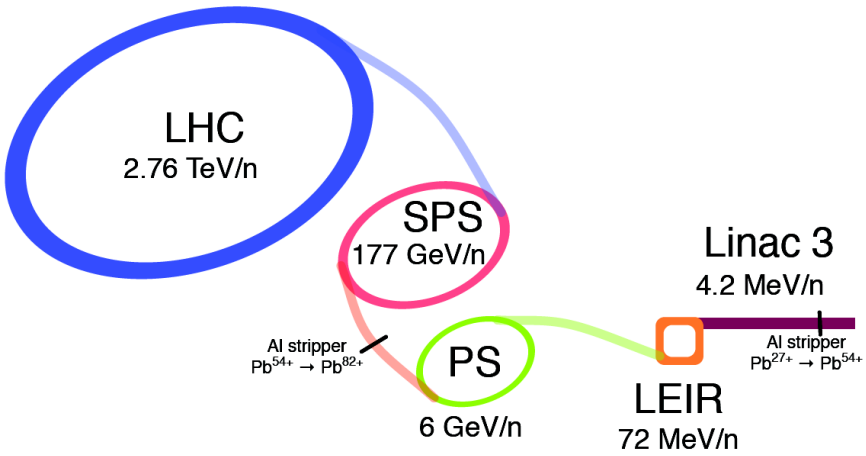

Figure 2.1: LHC injection chain.

mainly differ in the initial stage. As shown in Fig. 2.1, Pb^{208} are extracted from the ion source. They start at Linear accelerator 3 (LINAC3) which is the starting point of a sequence of injection chain leading to the LHC. At LINAC3, the first couple of electrons are stripped away and ions Pb^{27+} are accelerated to centrer of mass energy of 4 MeV per nucleon. Then they continue to Low Energy Ion Ring

(LEIR) where the ions are again accelerated up to 72 MeV per nucleon. Also more electrons are stripped away. Then the ions Pb^{54+} are processed to Proton Synchrotron (PS) where they gain energy of 6 GeV per nuleon. Before they are send to Super Proton Synchrotron (SPS), the final ions Pb^{82+} are produced. In the end from SPS where ions are accelerated up to 177 GeV per nucleon they continue to LHC where the ions are accelerated to the desired center of mass energy.

Protons are extracted from a hydrogen tank and injected in a linear accelerator (LINAC2) in which they reach an energy of 50 MeV. After that, they are accelerated up to 1.4 GeV in the Proton Synchrotron Booster (PSB) and injected to the Proton Synchrotron (PS), which leads to the the Super Proton Synchrotron (SPS). After the SPS, protons at 450 GeV can be injected to the LHC accelerator ring.

There are four big experiments and several smaller ones at the LHC. Among the main experiments are A Toroidal LHC Apparatus (ATLAS), Compact Muon Solenoid (CMS), A Large Ion Collider Experiment (ALICE) and Large Hadron Collider Beauty (LHCb). And among the small ones are for example Total Elastic and Diffractive Cross Section Measurement (TOTEM), Large Hadron Collider Forward (LHCf) or Monopole and Exotic Particle Detector at the LHC (MOEDAL).

2.2 ATLAS detector

The ATLAS detector [72] is a modern multi-purpose particle detector situated at Interaction Point 1 of the LHC ring. It was designed to measure many interesting processes and search for new physics. ATLAS is also involved in the studies of the heavy ion collisions. One of the main outcome is the experimental study of the quark-gluon plasma. The plasma properties can be studied using various measurements such as elliptic flow measurement, jet measurements or measurements of charmonic, see e.g. [68, 73, 74].

ATLAS is intentionally constructed to precisely measure particles with different properties such as electrons, hadrons, photons and muons. To accomplish that, ATLAS is divided into several layers that all cover the full 2π in azimuthal range, see Fig. 2.2. The inner detector (ID) is the closest apparatus to the interaction point. Its purpose is to measure tracks and transverse momenta of charged particles together with the primary and secondary vertices. Inner detector is placed in the solenoid magnetic field of $B = 2$ T. The next layer is the electromagnetic and hadronic calorimeter used to measure energy of the electromagnetically and strongly interacting particles. The most outer part of the ATLAS detector consists of precise muon spectrometer which is placed in the toroidal magnetic field of $B = 0.5$ T. Its purpose is to measure the momentum of muons.

The origin of the coordinate system in ATLAS is the nominal interaction point. In the Cartesian coordinate system the z-axis is oriented parallel to the beam line in anti-clockwise direction, the x-axis points horizontally to the centre of the LHC ring and the y-axis is perpendicular to the x-axis and z-axis and points upwards. The detector is symmetric with respect to the perpendicular plane spanned by the x and y axis. The symmetry of the detector makes cylindrical

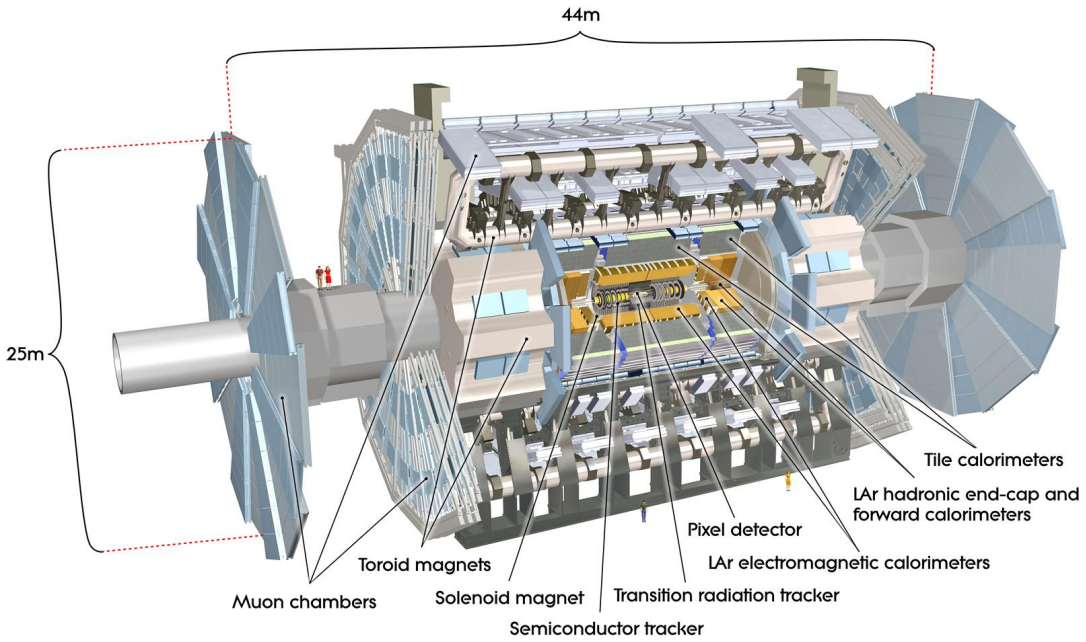

Figure 2.2: The ATLAS detector.

coordinates useful with variables (r, ϕ, θ) where r is the transverse radius from the beam axis and the azimuthal angle, ϕ, is the angle in the perpendicular plane to the beam axis (z-axis). The polar angle, θ, is defined as the angle with the positive z-axis and is measured from the beam axis.

Pseudorapidity, η, is a parameter commonly used due to the fact that it only depends on the polar angle, θ, of the particle's trajectory, and not on the energy of the particle and it is Lorentz invariant. Pseudorapidity is defined as:

$$\eta = -\ln\left(\tan\frac{\theta}{2}\right). \tag{2.1}$$

Rapidity is defined as:

$$y = \frac{1}{2}\ln\frac{E + p_z}{E - p_z}, \tag{2.2}$$

where E and p_z is the energy and the component of the momentum along the beam direction.

2.2.1 Inner detector

The Inner Detector (ID) is the 6.2 m long precision tracker with cylindrical shape of radius 1.15 m. The ID is the closest detector to the interaction point and, as mentioned in the previous section, it is placed in the solenoid magnetic field of $B = 2$ T. Its task is to reconstruct the trajectories of charged particles that are delivered by the LHC. It performs momentum and vertex measurements and it is used also for the electron identification. The design of the Inner detector allows pseudorapidity coverage up to $|\eta| < 2.5$ and track reconstruction for particles with $p_{\mathrm{T}} > 100$ MeV.

The ID is divided in three parts: a central barrel region and two symmetric end-caps. The barrel part of the ID extends over ± 80 cm along the z-axis. The schematic view of the ID is shown in Fig. 2.3. The ID is composed by these subsystems: the Pixel Detector, the Semiconductor Tracker (SCT) and the Transition Radiation Tracker (TRT).

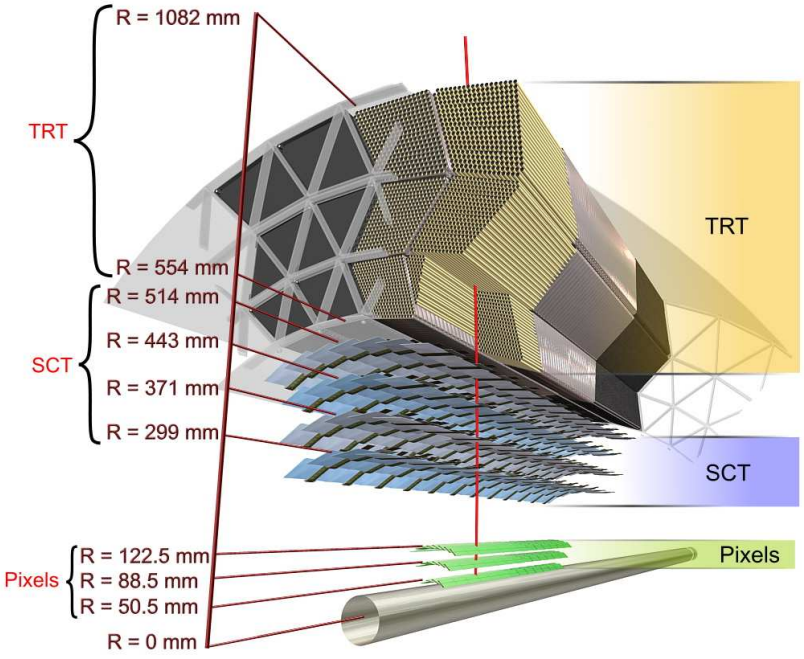

Figure 2.3: Layout of the Inner detector.

Pixel Detector

The Pixel Detector is the inner most sub-detector. It occupies the radii between 5 and 15 cm from the interaction point and it consists of over 80 million pixel detectors of size 50×400 μm. The pixel modules are single silicon sensors mounted onto 1744 modules and they are segmented in r, ϕ and η. It consists of one B–layer ($|\eta| < 2.5$) named by its important role in B-physics, two cylindrical barrel layers ($|\eta| < 1.7$) and two end-caps ($1.7 < |\eta| < 2.5$), with three discs on each side of the central barrel. The resulting intrinsic resolution is 12 μm in the $r\phi$ (transversal) direction and 66 μm in the z (longitudinal) direction and 77 μm in $r\phi$ direction for the end-caps.

Semiconductor Tracker

The Semiconductor Tracker (SCT) is in the middle section of the ID and consists of four barrel layers ($|\eta| < 1.4$) and two end-caps ($1.4 < |\eta| < 2.5$). SCT provides additional information about the particle's trajectory and interaction points up to pseudorapidity coverage $|\eta| < 2.5$. Each $p^{+}n$ silicon detector is approximately 6×6 cm^2 rectangle, 285 μm thick with 768 readouts strips of 80 μm pitch. The modules are 12.87 cm long strips placed in rows parallel to the beam axis on each barrel. A single module consists of two pairs of silicon detectors. Each end-cap consists of 9 disks supported by a cylinder with modules arranged in

rings within a disk. A disk may have up to three rings, therefore three types of end-cap modules (namely inner, middle, and outer) are needed. The design required resolution of the SCT is 17 μm in the $r\phi$ direction and 580 μm in the z direction for the barrel and 580 μm in the $r\phi$ direction for the end-caps.

Transition Radiation Tracker

The Transition Radiation Tracker (TRT) is the outermost segment of the ID that additionally provides the particle identification and trajectory coordinates. It is based on the use of straw detectors with the capability to generate and detect transition radiation. It consists of about 300 000 gaseous straw tubes arranged in 73 layers in the barrel region ($|\eta| < 2.5$) and 2×160 straw planes in the end-cap regions ($0.7 < |\eta| < 2.5$). Each straw tube with diameter of 4 mm is filled with a gas mixture of Xe (70%), CO_2 (27%) and O_2 (3%). One of the main reasons to use a gas mixture is to minimize the material used to build the ID. The gas mixture provides an efficient X-ray absorption, a fast charge collection and a stable operation over a sufficient high-voltage range even at high particle rates. Its technology allows to have an intrinsic resolution of 170 μm per straw for both the barrel and end-cap regions.

2.2.2 Calorimeters

The next major system of detectors which is between the ID and muon chambers is the calorimeter system. The ATLAS uses sampling calorimeters that are used to measure energy of all particles except muons and neutrinos.

There are two subsystems of calorimeters with different purposes. The inner subsystem is an electromagnetic (EM) calorimeter, while the outer subsystem is comprised of the hadronic calorimeters. The EM calorimeter is designed to stop particles that interact electromagnetically and the hadronic calorimeters stop and measure energy of the strongly interacting particles. One of the prominent features of the EM calorimeter is fine granularity to resolve photons and electrons in high detail. The forward calorimeter (FCAL) improves the overall coverage of the ATLAS detector and enables accurate measurements of jets and missing transverse energy. The hadronic calorimeters have coarser granularity compared to the EM calorimeters because of the larger volume occupied by jets, compared to electrons and photons. Fig. 2.4 shows the ATLAS calorimetric systems.

Electromagnetic Calorimeter

The electromagnetic calorimeter uses liquid argon (LAr) as the active material and lead as an absorber in both the barrel and end-cap regions, covering together the pseudorapidity range up to $|\eta| < 3.2$. In the EM calorimeter, the barrel is divided into two equal halves. The barrel region is located from 1.25 m to 2.05 m away form the z axis covering $|\eta| < 1.475$ and consisting of three layers of varying granularity The first layer, has a $\Delta\eta \times \Delta\phi$ granularity of 0.003×0.1. The second layer $\Delta\eta \times \Delta\phi$ granularity is 0.025×0.025, and the third is 0.05×0.025. The resolution of the electromagnetic calorimeter is $\sigma/E = 10\%/\sqrt{E[\text{GeV}]} \oplus 0.7\%$.

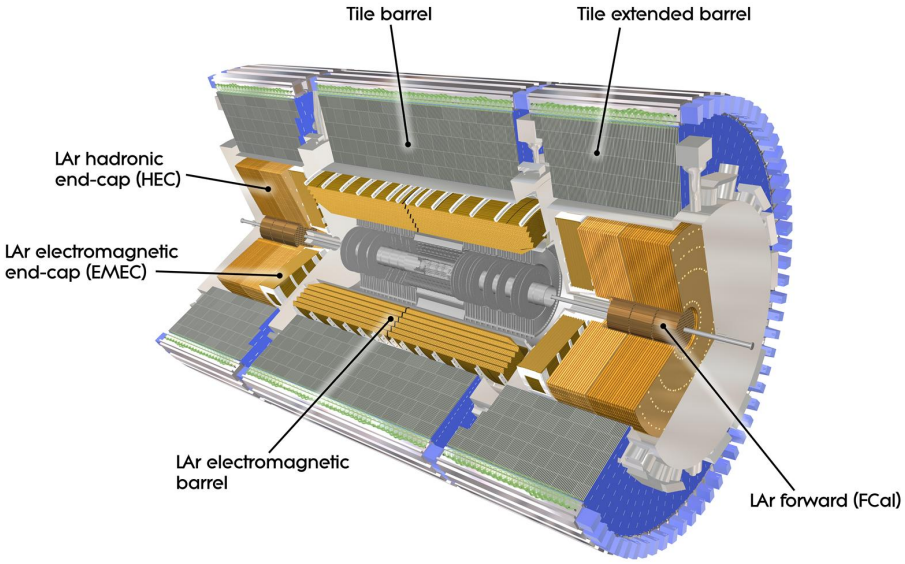

Figure 2.4: The electromagnetic and hadronic calorimeters of the ATLAS detector.

The electromagnetic end-cap calorimeter (EMEC) are wheels 63 cm thick located on each side of the barrel LAr calorimeter. The wheels provide coverage for $1.375 < |\eta| < 3.2$, overlapping with the barrel. In this overlap region, a pre-sampler spanning $1.5 < |\eta| < 1.8$ accounts for energy lost in the barrel calorimeter.

Hadronic Calorimeter

The hadronic sampling calorimeter is located outside of the EM calorimeters and is designed to stop and measure the energies of the hadrons. The barrel region of the hadronic calorimeter is called the tile calorimeter, providing coverage for $|\eta| < 1.7$ and consisting of central ($|\eta| < 1.0$) and extended regions ($0.8 < |\eta| < 1.7$) on each side. These have lengths of 5.8 m and 2.6 m, respectively, and inner and outer radii of 2.28 m and 4.25 m. Each barrel contains 64 modules consisting of alternating steel plates and scintillating tiles.The scintillating tiles are 3 mm thick and made of polystyrene, doped with wavelength-shifting compounds. Each tile is encased in a protective plastic sleeve that also keeps scintillation photons from escaping the tile. The ratio of steel plates to scintillating tiles is 4.7:1 by volume. The first two layers have granularity $\Delta\eta \times \Delta\phi = 0.1 \times 0.1$, the third layer has $\Delta\eta \times \Delta\phi = 0.2 \times 0.1$. The hadronic calorimeter has a resolution of $\sigma/E = 50\%/\sqrt{E[\text{GeV}]} \oplus 3\%$.

The hadronic end-cap calorimeters (HEC) are located outside of the electromagnetic end-cap calorimeter and cover the region $1.5 < |\eta| < 3.2$. The HEC uses LAr as the active material, has copper absorbers, and is divided into two wheels, a front and rear, each containing 32 modules. The granularity of the HEC is $\Delta\eta \times \Delta\phi = 0.1 \times 0.1$ for $|\eta| < 2.5$ and 0.2×0.2 otherwise.

The outermost calorimeter systems are the forward calorimeters (FCAL), designed to cover $3.1 < |\eta| < 4.9$. This extreme pseudorapidity range furthers

the goal of making the detector as hermetic as possible, important especially for missing transverse energy measurements. The inner module is used for EM calorimetry, while the outer two modules are devoted to hadronic measurements. All of them use LAr as the active material. The FCAL calorimeter is placed 4.7 m far from the interaction point, subjects it to high particle fluxes, requiring that the plastic be radiation-hard. It has a resolution of $\sigma/E = 100\%/\sqrt{E[\text{GeV}]} \oplus 10\%$. In Pb+Pb collisions the FCAL detectors are used for measuring the centrality of the collisions, for more details see Sec. 1.5.

2.2.3 Muon spectrometer

The Muon Spectrometer (MS) is the most outer most part of the ATLAS detector. The spectrometer provides a precise measurement of the muon momentum in the pseudorapidity region of $|\eta| < 2.7$ possible due to magnetic field of $B = 0.5$ T in the barrel region ($|\eta| < 1.0$) and $B = 1$ T in the end-caps region.

The muon spectrometer system consists of two high-precision tracking chambers: the Monitored Drift Tubes (MDT), $|\eta| < 2.0$, and Cathode Strip Chambers (CSC) used at the large pseudorapidities $2.0 < |\eta| < 2.7$, as well as two tracking chambers used for triggering, bunch-crossing identification and providing the coordinates in the non-bending plane: Resistive Plate Chambers (RPC) with $|\eta| < 1.05$ and Thin Gap Chambers (TGC), $1.05 < |\eta| < 2.7$. The layout of the different chambers is shown in Fig. 2.5. The azimuthal coverage is 2π and the momentum resolution for 1 TeV muon is about 10%.

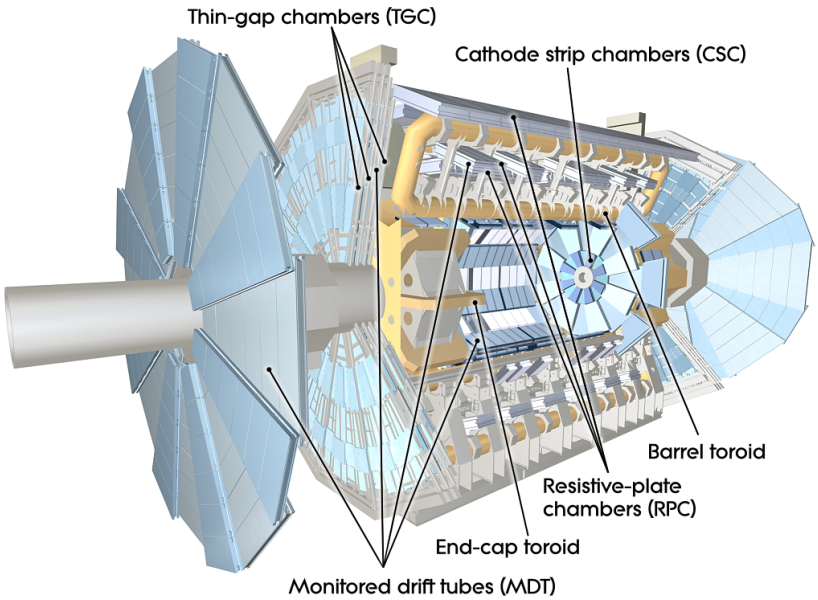

Figure 2.5: The muon spectrometer of the ALTAS detector.

2.2.4 Minimum bias trigger scintillators

The Minimum bias trigger scintillators (MBTS) [75] are used to both select minimum bias events online and reject background events in offline event selection.

Scintillators are made of polystyrene and they are located at $z = \pm 3.6$ m between the ID and the liquid argon calorimeter. The MBTS consist of two layers, inner and outer ring, each with 8 counters covering in a pseudorapidity range of $2.1 < |\eta| < 3.8$ and in full azimuth angle. One detector may provide up to 16 hits. The MBTS is primarily used offline for timing. Each hit caries a time information so the difference in time measured at A and C side, $\Delta t_{\mathrm{MBTS}} = t_A - t_C$, can be used to reject out-of-time signals corresponding to non-collision background or collisions between satellite bunches.

2.2.5 Zero degree calorimeters

The ATLAS Zero Degree Calorimeter (ZDC) [76] is a set of two sampling calorimeter modules symmetrically located at 140 m from the ATLAS interaction point. The ZDC covers a pseudorapidity range of $|\eta| > 8.3$ and it is both longitudinally and transversely segmented, thus providing energy and position information of the incident particles. ZDC observes forward going neutral particles that are produced in heavy-ion, pA or pp collisions. Using the coincidence between two arms, ZDC is one of main heavy ion triggers in ATLAS. In ultra-peripheral collisions, where almost no activity is present at central rapidities, the ZDC is the only available trigger. The ZDC uses Cherenkov light detection produced by the highly energetic charged particles in the shower. It consists of four modules grouped of 1.5 mm quartz rods running perpendicular to the beam and the light from these fibers is detected by photomultiplier tubes. This signal is used for the measurement of the energy deposited in the module.

2.2.6 Trigger system

With the LHC luminosity of 10^{34} cm^{-2}s^{-1} and bunch crossing of 25 ns leading to a 40 MHz collision rate, it is not possible to record all events by the data acquisition system. The ATLAS trigger [77] is a three level system which is a combination of hardware and software components designed to select interesting events. It performs a reduction from 40 MHz rate to about 200 Hz. The first level is entirely hardware-based trigger called first-level (L1) [78], the second software-based Higher Level trigger (HLT) is further divided into the second level (L2) and Event Filter (EF) triggers.

The L1 trigger makes fast decision with simple algorithms to match latency limit of 205 μs in which the reduction from 40 MHz to 75 kHz has to be provided. It selects events with high-p_{T} electrons, photons, jets, muons, hadronically decaying tau leptons candidates. The L1 also operates with the total missing energy E_{T}. The electromagnetic and hadronic clusters and missing transverse energy are obtained from coarse sums of transverse energy in trigger towers which are calorimeter units consisting of groupings of calorimeter cells. The granularity of these towers is $\Delta\eta \times \Delta\phi = 0.1 \times 0.1$. The energy deposited in the electromagnetic and hadronic calorimeters is summed separately and in parallel. Information on muon momentum, η and ϕ is passed to the L1 trigger from the RPC and TGC trigger chambers located at the muon spectrometer. The L1 algorithm uses information from the detectors to define regions of interest (RoI) around the identified high-momentum objects. All L1 trigger information is passed to the Central Trig-

ger Processor that ultimately decides on which events to trigger. If the event is accepted, the information is stored in readout buffers which are later read out by the HLT.

The HLT [77] consists of two steps, the Level 2 and Event filter trigger. The L2 trigger is designed to reduce the rate from 75 kHz to 1 kHz within the latency of 40 ms by using more complex algorithms. The L2 trigger uses the momentum, η and ϕ of objects provided by the L1 trigger in the RoI. The L2 has an access to data of objects from all other sub-detectors with the full granularity and precision. The Event filter is the final step in the triggering process. The selection is based on full granularity information about the entire event. The EF reduces output event rate from 1 kHz to the final 200 Hz that are then stored on tapes. The event processing time is approximately 4 s. The EF trigger is able to perform vertex reconstruction, track fitting, and includes bremsstrahlung of electrons. The access to complete data allows the EF trigger to perform monitoring, calibration and apply alignment corrections during detector operation. The calibration and alignment performed by the EF trigger is not the final one, but provides reliable intermediate values.

Because of the difference in processing times between trigger levels, events awaiting higher level decisions are kept in a pipeline. Data from accepted events are written into one or more data streams dedicated to various objects (e.g. muons, electrons and photons, jets and missing transverse energy) for analysis.

2.3 CMS and ALICE detector

CMS detector

CMS [79] is a multi-purpose detector with similar design as the ATLAS detector. It is 21.6 m long, 15 m in diameter, and weighs about 14.000 tonnes and it has the full 2π azimuthal coverage.

The inner detector reconstructs the bended trajectories of charged particles delivered by the LHC using superconducting solenoid. The magnet is 12.5 m long with an internal diameter of 6 m providing a uniform magnetic field of 3.8 T. The tracking system composed of a pixel detector with three barrel layers at radii between 4.4 and 10.2 cm and a silicon strip tracker with 10 barrel layers extending outwards to a radius of 110 cm. With two end-cap modules the pseudorapidity coverage is up to $|\eta| = 2.5$ and providing track reconstruction down to 100 MeV with a momentum resolution for reconstructed tracks about 1% at $p_{\mathrm{T}} = 100$ GeV in the barrel region and up to 2% in the end-cap region at the same p_{T}.

The calorimeters inside the magnetic coil consist of a lead-tungstate crystal electromagnetic calorimeter (ECAL) and a brass/scintillator hadron calorimeter (HCAL) with coverage up to $|\eta| = 3.0$. Steel/quartz-fibre Cherenkov hadron forward (HF) calorimeter covers the forward rapidities $3 < |\eta| < 5.2$. The calorimeter cells are grouped in projective towers of granularity in pseudorapidity and azimuthal angle given by $\Delta\eta \times \Delta\phi = 0.087 \times 0.087$ for the central rapidities $|\eta| \leq 2.0$, having a coarser segmentation at forward rapidities. Muons are measured in gas-ionization detectors embedded in the steel flux-return yoke of the magnet.

ALICE detector

The ALICE detector [80] is a general-purpose detector specially designed for the heavy-ion physics program. It consists of a central barrel, embedded in a large solenoidal magnet, and a muon arm with a separate dipole magnet and several smaller specialized subdetectors. The acceptance of the central detector system covers the pseudorapidity interval $|\eta| < 0.9$ over the full azimuth range while the muon arm covers the pseudorapidity interval $-4.0 < \eta < -2.5$. The ALICE magnet provides a magnetic field of 0.5 T, parallel to the beam axis. This field has been chosen to have both a good acceptance for low-p_{T} tracks and a good resolution for high-p_{T} tracks.

The central barrel includes the Inner Tracking System (ITS) which consists of six layer of silicon detectors, the Time Projection Chamber (TPC) which is the main tracking detector with pseudorapidity coverage of $|\eta| < 0.9$. It is filled with a gas that gets ionized when particle crosses the detector. Its purpose is to measure particle p_{T} as well as their identification. The next detector is the Transition Radiation Detector (TRD) for electron identification above $p_{\mathrm{T}} > 1$ GeV and the Time-of-Flight (TOF) for charged particle identification in the intermediate momentum range (from 0.2 to 2.5 GeV).

In addition, other three detectors with smaller acceptances are located at mid rapidity: the High-Momentum Particle Identification Detector (HMPID), which consists of an array of Cherenkov detectors designed to identify high-momentum particles and two electromagnetic calorimeters, the Photon Spectrometer (PHOS), the Electromagnetic Calorimeters (EMCaL) and the Di-jet calorimeter arm (DCal). The PHOS is dedicated to the measurement of photons and neutral mesons, while the EMCaL and DCal are meant to enhance ALICE capabilities in jet studies, besides from measure neutral mesons and electrons from heavy-flavour decay. The Forward Muon Spectrometer (FMS), which is designed to detect muons, is situated in the pseudo-rapidity range $-4.0 < \eta < -2.5$. In the same rapidity region there are also a Photon-Multiplicity Detector (PMD) and the Forward Multiplicity Detector (FMD), which is a silicon strip detector built to measure particle multiplicity. In addition, two sets of neutron and proton calorimeters, the Zero Degree Calorimeters (ZDCs) are located about 116 m far from the interaction point at almost zero degrees in order to measure the event centrality in Pb+Pb and p+Pb collisions. Two arrays of scintillator counters, the V0 detectors, are located on each side of the interaction point. They are used in ALICE to provide trigger and centrality information and to allow the rejection of beam-gas interactions. Other two Cherenkov counters, the T0 detectors, are installed to measure the interaction time of the collisions.

3. Jet reconstruction in ATLAS

In the ATLAS experiment, jet reconstruction is a modification of the procedure used in *pp* collisions which takes into account large UE present in the heavy-ion collisions. In this section we will describe this procedure along with its performance.

3.1 Jet reconstruction in Run 1

Jets are reconstructed using the heavy-ion jet reconstruction algorithms, which are discussed at length in Refs. [11]. Jets are clustered by the anti-k_t algorithm [27] with R parameter set to 0.4 using 0.1×0.1 calorimeter towers as inputs. The resulting jet kinematics are corrected for the presence an uncorrelated underlying event contribution to the calorimetric signal inside the jet cone using a background subtraction technique. A background transverse energy density $\rho_i(\eta, \phi)$ is defined separately for each calorimeter sampling layer denoted by the index i. For each cell clustered within the jet, the background is evaluated at the cell's coordinates and the cell's energy is corrected via:

$$E_{\mathrm{T}}^{\mathrm{cell}}\big|_{\mathrm{subtracted}} = E_{\mathrm{T}}^{\mathrm{cell}}\big|_{\mathrm{unsubtracted}} - \rho_{i^{\mathrm{cell}}}(\eta^{\mathrm{cell}}, \phi^{\mathrm{cell}})\Delta\eta^{\mathrm{cell}}\Delta\phi^{\mathrm{cell}}\,. \tag{3.1}$$

The jet's four-vector is then recomputed as the four-vector sum of the individual cell's four-vectors, which are taken to be massless. The concrete procedure of the UE estimation and subtraction is performed in two steps and works as follows.

A first estimate of the UE average transverse energy density, $\rho_i(\eta)$, is evaluated in 0.1 intervals of η from all cells in each calorimeter layer, i, within the given η interval excluding those within "seed" jets. In the first subtraction step, the seeds are defined to be $R = 0.2$ jets that are less susceptible to distortions from UE fluctuations[1]. The kinematics for $R = 0.2$ jets generated in this first subtraction step are calculated via a four-vector sum of all cells contained within the jets using the subtracted E_T values.

The second subtraction step starts with the definition of a new set of seeds using a combination of subtracted $R = 0.2$ jets from the first subtraction step with $E_T > 25$ GeV and track jets with $p_{\mathrm{T}} > 10$ GeV. Using this new set of seeds, a new estimate of the UE, $\rho_i(\eta)$, is calculated excluding cells within $R = 0.8$ of the new seed jets, where $R = \sqrt{(\eta_{cell} - \eta_{jet})^2 + (\phi_{cell} - \phi_{jet})^2}$. The new jet kinematics are obtained for all jet radii from a four-momentum sum of cells within the jets using the subtracted cell transverse energies. Jets generated in this second subtraction step having $E_T > 20$ GeV are recorded for subsequent analysis. Not mentioned in this description is a small correction of an azimuthal (ϕ) dependence of the UE specific to heavy-ion collisions which originates in the so called elliptic flow [81, 82]. The effects of elliptic flow are removed by reweighting the $\rho(\eta)$ by v_2 which quantifies the magnitude of the elliptic flow in a given event.

Due to finite thresholds imposed on seeds, jets themselves may affect the determination of ρ. The subtraction therefore introduces a shift in the JES for

[1] These jets are further required to contain at least one tower with $E_T > 3$ GeV and to have a ratio of maximum tower transverse energy to average tower transverse energy, E_T^{max}/E_T greater then 4.

jets allowed to contribute to ρ (self-energy bias) or other jets in the same event as a jet that contributes to ρ (mutual-energy bias). This effect can shift the JES by approximately 10% for the subset of jets that are affected by the self-energy bias. This bias is removed by the iterative UE subtraction in which the UE estimate is corrected for the presence of a jet and then subtracted again. This effectively removes any residual self-energy bias. This improvement is done during the reprocessing of the data. The rate of jets with the self-energy or mutual-energy bias is negligible for jets above 100 GeV and here it is mentioned only for a completeness.

Then, reconstructed jets need to be corrected for the non-uniformities in the calorimeter response and calibrated to the hadronic scale. The correction to the non-uniformities in the calorimeter response corrects the jet four-momenta using the η, ϕ map of the detector response measured in the data. The jets are then calibrated using the numerical inversion procedure. Finally, the jets are cross-calibrated[2] to *pp* jets to take into account the in-situ corrections to the JES and to allow a consistent evaluation of the systematic uncertainties both on jets reconstructed in *pp* collisions and Pb+Pb collisions.

The performance of the jet reconstruction and calibration in terms of JES is summarized in details in Ref. [83]. For jets with the kinematic selection used in this study ($p_{\mathrm{T}} > 100$ GeV, $|y| < 2.1$) a perfect closure in the JES in MC is seen, the overall systematic uncertainty from the JES is about 3-4%, and the jet reconstruction is fully efficient.

3.2 Jet reconstruction in Run 2

The jet reconstruction in *pp* and Pb+Pb collisions in run 2 is similar to the jet reconstruction in run 1. In run 1 the background subtraction only estimated the UE using the components of the second flow harmonic, v_2 and phase Ψ_2. In run 2 the 3$^{\mathrm{rd}}$ and 4$^{\mathrm{th}}$ harmonics are also used to improve the estimation of the background since the flow harmonics v_3 and v_4 (especially v_3) were found to improve the resolution of jets. Once each of the phases and magnitudes for $n \in (2; 4)$ are determined, the subtraction is applied cell-by-cell within the jet. An iterative procedure is used to remove the impact of jets on the background estimate ρ and the estimation of the magnitude of the flow harmonics. First the average UE density and the flow harmonics are estimated from the transverse energy of cells within $|\eta| < 3.2$. The subtraction is performed cell-by-cell within the jet to obtain the subtracted jet kinematics. Then the ρ and v_n are recalculated by excluding any cells within $\Delta R < 0.4$ of seed jets that are defined to be jets with $E_{\mathrm{T}} > 30$ GeV. These are then used to evaluate a new subtracted energy by applying these to the original cells and then calculating new jet kinematics.

3.2.1 Jet energy scale and jet energy resolution

The jet performance is characterized by evaluating the jet energy scale (JES) and resolution (JER) which are the mean and width of the response in the MC,

[2]The cross-calibration is a procedure in which the energy of a jets from one jet collection is changed such that their jet energy scale is consistent with the jet energy scale of jets from the other collection.

respectively. The response is generated by matching the truth to reconstructed jets in the MC within a cone on $\Delta R = \sqrt{\Delta\eta^2 + \Delta\phi^2} < 0.2$. The ratio of the reconstructed jet p_{T} to the truth jet p_{T} is evaluated as a function of the truth jet p_{T}. This is evaluated in the MC after the jets have been calibrated. This distribution is then fit in slices of the truth p_{T} with a gaussian distribution. The slices are then refit with a truncation around the mean because there are non-gaussian tails in the response that need to be removed from the fit. The mean of this fit is then taken the be the jet energy scale and the width is the jet energy resolution. This is evaluated in each rapidity and centrality bin in the analysis (also for pp). The details of both are described in the following two sub-sections.

Jet energy resolution

The JER as described above is the width of the ratio of reconstructed jet p_{T} in the MC to the truth jet p_{T}. It is expected that the JER can be parameterized as [84]

$$\sigma(\Delta p_{\mathrm{T}}) = a\sqrt{p_{\mathrm{T}}} \oplus b \oplus c p_{\mathrm{T}}. \tag{3.2}$$

The first and last terms are sensitive to aspects of the detector response and are expected to be independent of centrality, while the middle term is driven by the fluctuations uncorrelated with the jet p_{T}. This "noise" term is often thought of in terms of electronic or pileup noise, but in the most peripheral HI collisions, both of these contributions are small compared to the magnitude of the UE fluctuations. The JER for different centrality bins and for pp collisions inclusive in rapidity is shown in Fig. 3.1. Fits using the form of Eq. 3.2 are indicated with dashed lines. In the fits there is no assumption that the a and c terms should be independent. They are generally found to be independent of centrality. In contrast, the b terms have a strong centrality dependence as is shown in Fig. 3.2 for jets with $|y| < 0.4$.

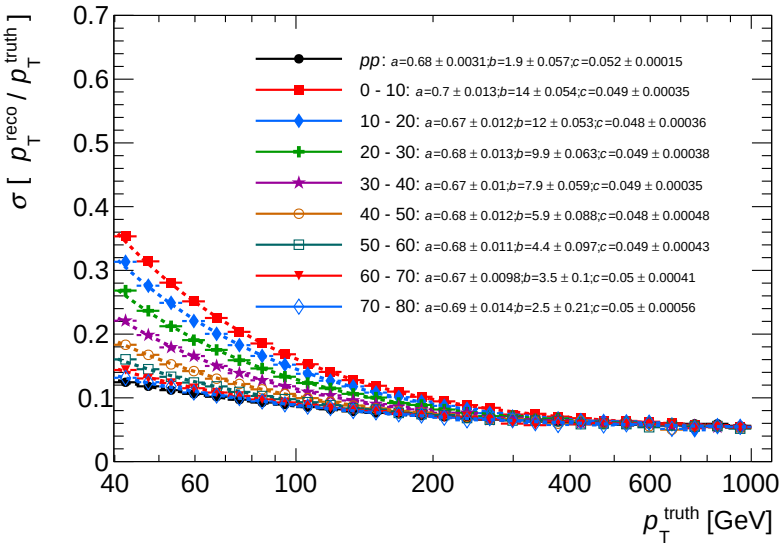

Figure 3.1: The fractional jet energy resolution as a function of jet p_{T} in different centrality bins for jets with $|y| < 2.8$. The dashed lines indicate fits using the functional form in Eq. 3.2 with the fit parameters and their uncertainties indicated in the legend.

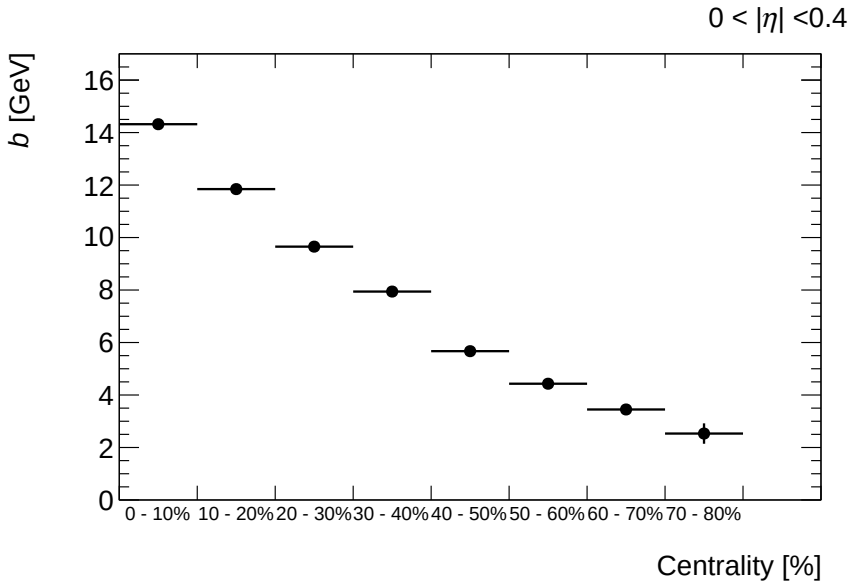

Figure 3.2: The b parameter from the fits of the JER using the functional form in Eq. 3.2 for jets with $|y| < 0.4$ for Pb+Pb collisions. Errors from the fit are included but are not visible.

To make the comparison between fits and JER distributions more quantitative, the quadratic difference between the JER in central collisions and pp collisions was evaluated:

$$\Delta\sigma^2 \equiv \sigma^2[p_{\mathrm{T}}^{\mathrm{reco}}/p_{\mathrm{T}}^{\mathrm{truth}}]\big|_{\mathrm{cent}} - \sigma^2[p_{\mathrm{T}}^{\mathrm{reco}}/p_{\mathrm{T}}^{\mathrm{truth}}]\big|_{pp} = \frac{b_{\mathrm{cent}}^2 - b_{pp}^2}{p_{\mathrm{T}}^{\mathrm{truth}}} \tag{3.3}$$

where the last equality holds under the assumption that the centrality dependence of the JER can be described entirely in terms of changes to the b term. This quantity is shown in the left panel of Fig. 3.3 and fits to the functional form in Eq. 3.3 are also indicated with dashed lines. The values of $\sqrt{b_{\mathrm{cent}}^2 - b_{pp}^2}$ obtained from the fit and their uncertainties are shown in the right panel of Fig. 3.3.

As the MC sample utilizes data overlay, it is expected that the effects of such

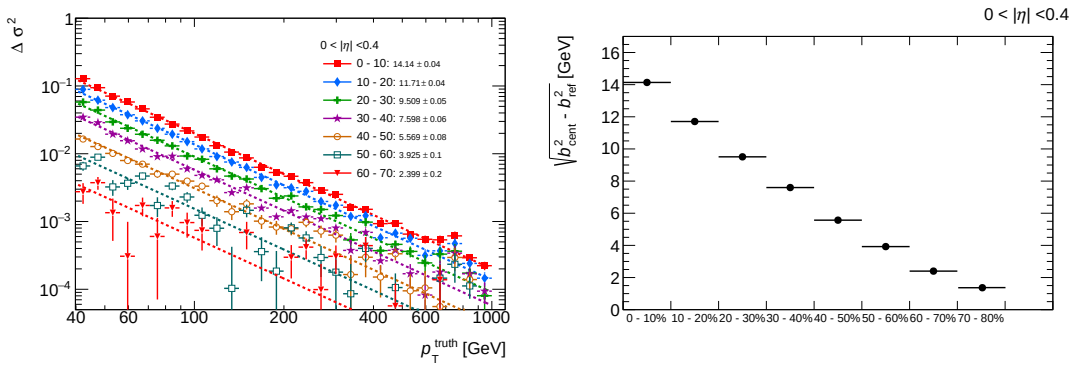

Figure 3.3: Left: the quadratic difference in the JER between central collisions and pp collisions with fits to the form described in Eq. 3.3. Right: The values of $\sqrt{b_{\mathrm{cent}}^2 - b_{pp}^2}$ obtained from the fit. Evaluation is done for jets with $|y| < 0.4$

fluctuations, including their centrality dependence should be well represented in the MC sample. To evaluate the uncertainty, a data-driven estimate of Δb^2_{data} was constructed from an independent analysis of the UE fluctuations. A similar analysis was performed in the run 1 data and is documented extensively in Refs. [85, 11]. This analysis uses continuous groups of calorimeter towers of comparable size as an $R = 0.4$ jet: $\pi R^2/\Delta\eta_{\text{tower}}\Delta\phi_{\text{tower}} \sim 50$ for $R = 0.4$, that is 7×7 group of towers. The total E_{T} for each group in event in the data was calculated and recorded in fine bins of $\Sigma E_{\text{T}}^{\text{FCal}}$. The standard deviations of the E_{T} distributions can be compared to the difference in the b values from the fits. These were found to be comparable to the results from the MC.

The JER, shown if Fig. 3.1, is larger in central collisions compared to peripheral which is what is expected because of the underlying event. The JER is $\approx 20\%$ at 100 GeV in central collisions and decreases with increasing p_{T} to a constant at about 8%. The impact of JER on measured distributions is removed by the unfolding procedure described in Sec. 5.2.2.

Jet energy scale

As described above the JES is the mean reconstructed jet p_{T} for a given truth jet p_{T}, that is $\langle p_{\text{T}}^{\text{reco}} / p_{\text{T}}^{\text{truth}} \rangle$. The JES was found to have a large ϕ dependence due to holes in the detector. This was fixed by applying an $\eta - \phi$ weighting on a cluster by cluster basis during the reconstruction. The jet yield as a function of ϕ with pp overlaid with different heavy-ion centrality bins are shown in Fig 3.5 after the weighting is applied in the reconstruction. This demonstrates that the jets have only small residual ϕ dependence.

The JES with pp overlaid with different heavy-ion centrality bins are shown in Fig 3.5. The JES is around 1% at high jet p_{T} which demonstrates good closure. The JES also has a minimal centrality dependence at high jet p_{T} which is expected. Any residual non-closure in JES will be fixed in the unfolding but starting with a good closure implies an easier unfolding problem.

Figure 3.4 shows the effect of the subtraction procedure on the jet energy scale as a function of the elliptical phase $2|\Psi_2 - \phi|$ on the left and $3|\Psi_3 - \phi|$ on the right. The unfilled black curve on each figure represents the dependence on the variables without applying the UE subtraction modulated by harmonic flow. It demonstrates a large variation for both the $n = 2$ and $n = 3$ harmonics. The filled curves represent the variation with the event plane variables with the harmonic flow subtraction. These show a very good closure.

Jet reconstruction efficiency

The jet reconstruction efficiency with pp overlaid with different heavy-ion centrality bins is shown in Fig 3.5. The efficiency is evaluated by taking the ratio of the truth jets that matched to reconstructed jets to all of the truth jets as a function of truth jet p_{T}. For jets included in this analysis (which have $p_{\text{T}} > 100$ GeV) the jet reconstruction is fully efficient.

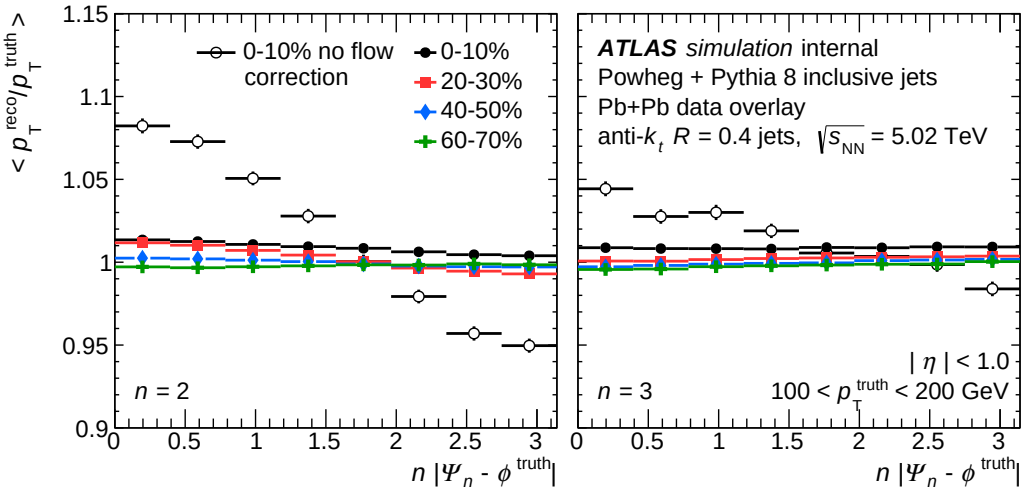

Figure 3.4: The jet energy scale as a function of $2|\Psi_2 - \phi^{\text{truth}}|$ (left) and $3|\Psi_3 - \phi^{\text{truth}}|$ (right) for jets with a truth p_{T} between 100–200 GeV. The black unfilled points are for 0–10% without the harmonic flow subtraction. The filled points are with the harmonic flow subtraction. This is shown in 0–10% (black circles), 20–30% (red squares), 40–50% (blue diamonds), and 60–70% (green crosses).

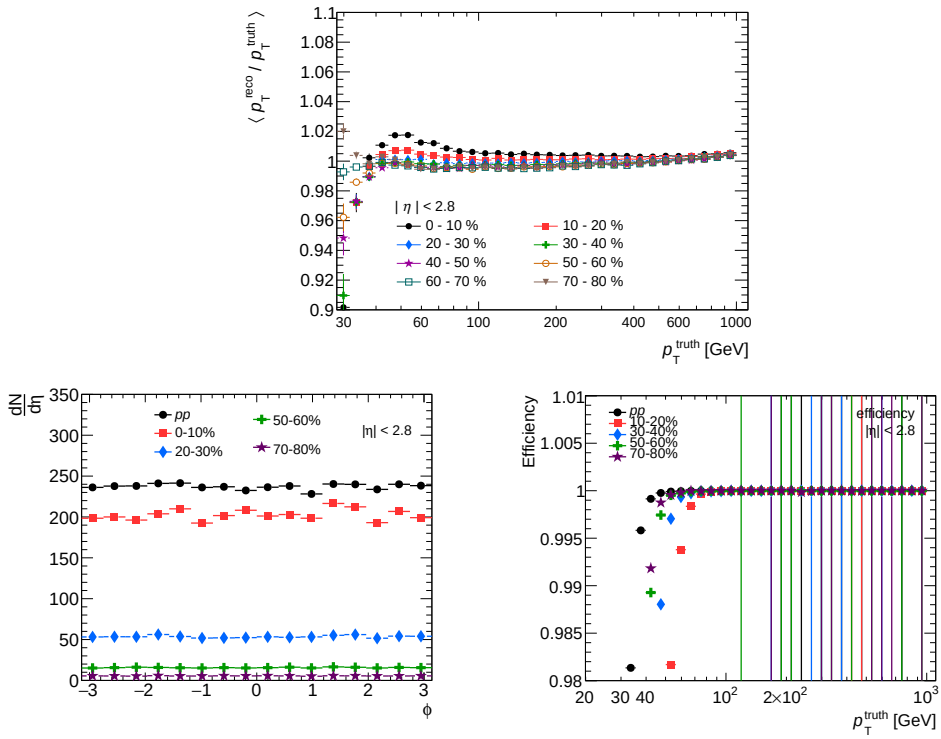

Figure 3.5: The JES as a function of truth jet p_{T} (upper panel) for different centrality bins in Pb+Pb collisions. The jet yield as a function of ϕ for truth jet $p_{\text{T}} > 50$ GeV in different centrality bins (lower left). The jet reconstruction efficiency as a function of truth jet p_{T} in different centrality bins (lower right). Different centrality bins are stated in the legend.

4. Jet fragmentation measurement

This chapter presents a measurement of the jet internal structure measured using the ATLAS detector in Pb+Pb and *pp* collisions, both at the same center-of-mass energy per colliding nucleon pair of 2.76 TeV. The measurement utilizes Pb+Pb data collected during 2011 corresponding to an integrated luminosity of 0.14 nb^{-1} as well as data from *pp* collisions recorded during 2013 corresponding to 4.0 pb^{-1}.

Analysis presented here is a follow up on a previous analysis [9] of the jet internal structure. In this new analysis the same observables are used as in Ref. [9]. $D(z)$ and $D(p_{\text{T}})$ distributions are previously defined in Eqs. (1.32)–(1.34), respectively. The new analysis also extends the minimum p_{T} for charged particles to 1 GeV and evaluates the fragmentation observables differentially in the jet transverse momentum p_{T} and jet rapidity, y. Furthermore, the new analysis uses the fragment distributions measured in *pp* collisions as a reference for the measurement of the jet fragmentation in heavy-ion collisions. This more detailed information on the jet structure should allow a better characterization of the flow of the energy lost by the initial parton and will help to understand the features seen in the suppression of inclusive jet yields such as the unexpected absence of the evolution of nuclear modification factors with rapidity.

This chapter is organized as follows: Sec. 4.1 provides a basic description of the analysis. Sec. 4.2 summarizes the data that were used for this study as well as the event selection and centrality selection. Sec. 4.3 describes the cuts and corrections used for jets and charged particles in the analysis. Sec. 4.4 summarizes the systematic uncertainties associated with the measurement. Sec. 4.5 describes the results of the measurement. Methods used for the jet reconstruction in heavy-ion collisions were previously describes in Sec. 3.1.

Analysis presented in this chapter was published in Ref. [14].

4.1 Basics analysis description

4.1.1 Measuring fragmentation distributions

The first step in the analysis is to obtain the uncorrected measured fragmentation functions, $D^{\text{meas}}(z)$, and the distribution of charged particle transverse momenta measured inside the jet, $D^{\text{meas}}(p_{\text{T}})$, which are defined using following formulae,

$$D^{\text{meas}}(p_{\text{T}}) \equiv \frac{1}{\varepsilon}\frac{\Delta N_{\text{ch}}(p_{\text{T}}^{\text{ch}})}{\Delta p_{\text{T}}^{\text{ch}}}, \tag{4.1}$$

$$D^{\text{meas}}(z) \equiv \frac{1}{\varepsilon}\frac{\Delta N_{\text{ch}}(z)}{\Delta z}. \tag{4.2}$$

Here $\Delta N_{\text{ch}}(p_{\text{T}}^{\text{ch}})$ and $\Delta N_{\text{ch}}(z)$ represent the number of measured charged particles within $\Delta R = 0.4$ of the jet axis in given bins of charged particle transverse momentum, p_{T}^{ch}, and z respectively[1]. The ε represents the MC-evaluated track

[1]The indices 'ch' and 'jet' are introduced in this section to better distinguish the quantities connected with charged particles from quantities connected with jets.

reconstruction efficiency which is described in Sec. 4.3.2. The superscript 'meas' in Eqs. (4.1), (4.2) indicates that the measured distributions do not contain any corrections except the correction for the tracking efficiency and few other basic corrections (such as bad-jet rejection or b-jet rejection) which are discussed in Sec. 4.3. The corrections for the UE and detector effects were applied in the subsequent steps of the analysis as discussed in the next paragraphs.

Charged particles from the UE constitute a background which needs to be subtracted from the measured distributions. This background depends on $p_{\mathrm{T}}^{\mathrm{ch}}$ and η of charged particle, and the centrality of the collision. The evaluation of UE charged particle yields, $\mathrm{d}n_{\mathrm{ch}}^{\mathrm{UE}}/\mathrm{d}p_{\mathrm{T}}^{\mathrm{ch}}$ and $\mathrm{d}n_{\mathrm{ch}}^{\mathrm{UE}}/\mathrm{d}z$ is described in Sec. 4.3.3. These UE distributions are then subtracted from measured distributions as follows

$$D^{\mathrm{sub}}(p_{\mathrm{T}}) = D^{\mathrm{meas}}(p_{\mathrm{T}}) - \frac{\mathrm{d}n_{\mathrm{ch}}^{\mathrm{UE}}}{\mathrm{d}p_{\mathrm{T}}^{\mathrm{ch}}}, \tag{4.3}$$

$$D^{\mathrm{sub}}(z) = D^{\mathrm{meas}}(z) - \frac{\mathrm{d}n_{\mathrm{ch}}^{\mathrm{UE}}}{\mathrm{d}z}. \tag{4.4}$$

The UE subtracted measured distributions, $D^{\mathrm{sub}}(p_{\mathrm{T}})$ and $D^{\mathrm{sub}}(z)$, need to be corrected for the detector effects. There are two main detector effects: smearing due to finite jet energy resolution and smearing due to finite track momentum resolution. The correction for the former involves unfolding in the $p_{\mathrm{T}}^{\mathrm{jet}}$, while correction for the latter involves unfolding in the $p_{\mathrm{T}}^{\mathrm{ch}}$. Since the tracks were evaluated in jets, a two-dimensional unfolding needs to be used to correct for both of these detector effects simultaneously. Two-dimensional Bayesian unfolding [86] using the RooUnfold package [87] was used. The response matrices for the unfolding were created separately for pp and Pb+Pb data for each centrality and rapidity bin. The entries to the response matrix were weighted by the tracking efficiency correction. The impact of resolutions on the measurement is discussed in Sec. 4.5.1 and the unfolding is discussed in Sections 4.5.3 and 4.5.4.

The proper normalization of the measured distributions by the number of jets requires a separate unfolding of the jet p_{T} spectrum. This was performed by applying a one-dimensional Bayesian unfolding, separately in each centrality and rapidity interval. The unfolded jet p_{T} spectra were integrated over a given jet p_{T} interval. The result of this integration represents the total number of jets in a given p_{T} interval and was used to normalize the unfolded fragmentation distributions, $D^{\mathrm{unfolded}}(p_{\mathrm{T}})$ and $D^{\mathrm{unfolded}}(z)$, as follows

$$D(p_{\mathrm{T}}) = \frac{1}{N_{\mathrm{jet}}} D^{\mathrm{unfolded}}(p_{\mathrm{T}}), \tag{4.5}$$

$$D(z) = \frac{1}{N_{\mathrm{jet}}} D^{\mathrm{unfolded}}(z), \tag{4.6}$$

where $D(p_{\mathrm{T}})$ and $D(z)$ are the final, particle level corrected distributions.

The performance of the above described reconstruction procedure was tested by comparing unfolded distributions in MC samples with truth distributions. The ratio of corrected to truth distributions was found to be consistent with unity for all the bins used in the measurement as shown in Sec. 4.5.3.

To summarize the analysis flow: First, the per-track and per-jet corrections are applied (e.g. tracking efficiency correction, bad jet rejection) when looping over all the events in the data or Monte Carlo. Loop over events produces:

the measured signal distributions (e.g. $D(p_{\mathrm{T}})$), measured UE distributions (e.g. $\mathrm{d}n_{\mathrm{ch}}^{\mathrm{UE}}/\mathrm{d}p_{\mathrm{T}}^{\mathrm{ch}}$), and measured jet p_{T} spectra. Then, the UE subtraction is applied on the measured distributions and UE-subtracted distributions are produced. Then, these distributions are unfolded using the 2D Bayesian unfolding. The measured jet spectra are also unfolded but using a 1D Bayesian unfolding. The unfolded jet spectra are used to normalize the unfolded fragmentation distributions so that the final per-jet distributions are obtained. The flow chart of the analysis is depicted in Fig. 4.1.

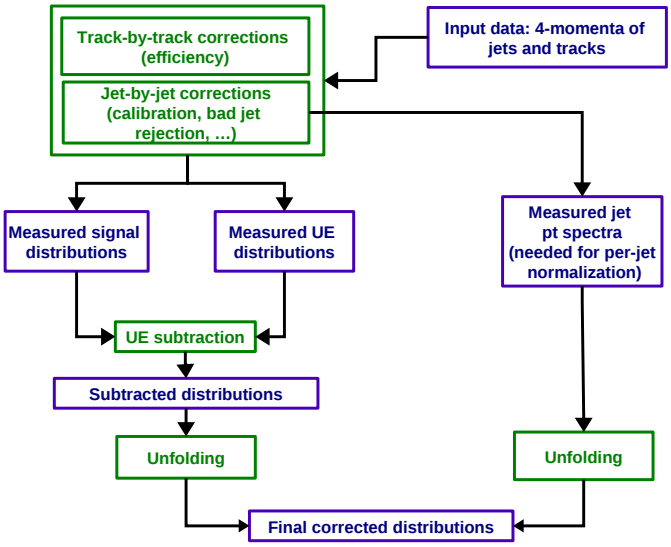

Figure 4.1: The flow-chart of the analysis. The different steps in the analysis are in green, the distributions at different level are in blue.

4.1.2 Calculating ratios of fragmentation distributions

As shown in the first study [9], the modification of the jet internal structure due to the jet quenching depends on the centrality of the collision. In more central collisions the modification should be more pronounced. Therefore, the fragmentation was evaluated in seven centrality bins: 0–10%, 10–20%, 20–30%, 30–40%, 40–50%, 50–60%, and 60–80% and for pp collisions that are used as a reference. This allows to evaluate the ratio between fragmentation observables measured in heavy ion collisions to the fragmentation observables measured in pp collisions, defined as

$$R_{D(z)} = \frac{D(z)|_{\mathrm{cent}}}{D(z)|_{p+p}} \tag{4.7}$$

$$R_{D(p_{\mathrm{T}})} = \frac{D(p_{\mathrm{T}})|_{\mathrm{cent}}}{D(p_{\mathrm{T}})|_{p+p}}. \tag{4.8}$$

Here index ‘cent’ stands for one of the seven centrality bins.

4.2 Data sample and event selection

4.2.1 Heavy-ion data

The Pb+Pb data used in this study was collected during the 2011 heavy-ion run. The full sample of events reconstructed in the Hard Probe stream has been used. Hard Probe stream consists of different High Level Triggers (HLT) triggering on high-p_{T} jets, muons, electrons, and photons. The total collected luminosity of 158 $\mu\mathrm{b}^{-1}$ has been used. All the runs were required to pass the official good run list (GRL). The GRL excluded the lumiblocks with badly functioning subdetector systems. All the subdetector systems, namely tracking, calorimeter, and muon spectrometers, were required to be fully functional. This lead to the reduction of the luminosity from original 158 $\mu\mathrm{b}^{-1}$ to 140 $\mu\mathrm{b}^{-1}$.

To collect events with rare processes such as jet events, the high-level-trigger (HLT) was employed in 2011 heavy-ion run. The HLT jet algorithms are based on the heavy-ion jet finding algorithms used in the offline jet reconstruction. The HLT algorithms are simplified although they contain the full subtraction of the underlying event performed at the cell-by-cell basis. The default jet finding algorithm used in HLT for heavy-ions is anti-k_t algorithm with the distance parameter $R = 0.2$. The default unprescaled HLT chain used to select the events in this study is *EF_j20_a2hi_L1TE10*. This primary HLT trigger requires at least one HLT anti-k_t $R = 0.2$ jet with $E_{\mathrm{T}} > 20$ GeV present in the event. The HLT trigger is seeded by events with the total energy greater than 10 GeV (TE10) selected by the Level 1 trigger. The HLT trigger jets are at the electromagnetic scale. Beside the HLT trigger requirement the events have to obey the requirement of at least one good primary vertex and good timing measured by Minimum-Bias Trigger Scintillator (MBTS), see Sec. 2.2.4. The MBTS timing cut is ($|time(\mathrm{MBTS\ A}) - time(\mathrm{MBTS\ C})| < 3$ ns) with both MBTS times not equal to zero and not equal to ± 75 ns (to avoid the MBTS overflow). For $R = 0.4$ offline jets the trigger efficiency reaches a plateau at $p_{\mathrm{T}} \approx$ 90 GeV, which is well below the p_{T} cut of 100 GeV used in this study.

4.2.2 Proton-proton data

The *pp* data used in this analysis was recorded during the 2013 operation at $\sqrt{s} = 2.76$ TeV. It consists of a total integrated luminosity of 4.1 pb^{-1}. The pileup during this period varied from 0.3–0.6. Events were selected using the HLT trigger running the $R = 0.4$ anti-k_t jets and requiring a minimum p_{T} of 75 GeV. For $R = 0.4$ offline jets the trigger efficiency reaches a plateau at $p_{\mathrm{T}} \approx$ 80 GeV, which is well below the p_{T} cut of 100 GeV used in this study. Beyond the trigger selection the only additional requirements for the events where that the luminosity blocks be flagged as having good data quality and that the event contained a reconstructed primary vertex.

4.2.3 Heavy-ion Monte Carlo

As a Monte Carlo (MC) reference, this study utilize a sample of minimum bias heavy-ion data events with embedded MC11 PYTHIA *pp* di-jet events at $\sqrt{s} =$ 2.76 TeV. PYTHIA simulation uses PYTHIA version 6.423 [88] and the AUET2B

J	p_{T}^{min} [GeV]	p_{T}^{max} [GeV]	σ [nb]
1	17	35	$1.88 \cdot 10^{5}$
2	35	70	$8.28 \cdot 10^{3}$
3	70	140	$2.94 \cdot 10^{2}$
4	140	280	6.45
5	280	560	$6.39 \cdot 10^{-2}$

Table 4.1: Definitions of PYTHIA samples used in embedding. For each J value samples were produced with the same number of events, one million, to ensure high statistical sampling for a jet p_{T} out to 500 GeV. Each J sample has a cross-section weighting σ.

tune [89]. The minimum bias heavy-ion data were collected for this overlay MC during the 2011 run. The events were recorded by a dedicated minimum bias trigger. PYTHIA MC consists of five sets of samples (J1-J5 samples), each with a fixed range set on the p_{T}^{min} and p_{T}^{max} in the PYTHIA hard scattering. A single minimum bias event was overlayed on an event from each of the different J samples, with no reuse of minimum bias events. The different J samples are then combined using a cross-section weighting obtained from PYTHIA to build a combined sample with good counting statistics over a wide range of jet p_{T}. The definitions of the PYTHIA samples can be found in Tab. 4.1. The overlay sample will be referred to as "MC11" throughout the text of this chapter.

4.2.4 Proton-proton Monte Carlo

The MC sample used for the simulation of pp data utilizes the same generator and tune but was simulated with detector conditions corresponding to 2013.

4.3 Basic Cuts and Corrections

In this section we discuss the default cuts on jet kinematics as well as tracking selection cuts. We also discuss the corrections that have been made to the measured objects (jets or tracks) and to the measured distributions. The list of important corrections is the following:

- Tracking efficiency correction
- Underlying event subtraction
- b-jet exclusion
- Jet isolation
- Bad jet exclusion
- Monte Carlo reweighting

Each of these correction is discussed below in a separate section. The performance of these correction is discussed in Sec. 4.5.3.

4.3.1 Jet and tracking selection cuts

Since the Inner Detector (ID) covers the $|\eta| < 2.5$, the analysis can only be performed for jets within the rapidity interval of $|y| < 2.1$ since $R = 0.4$ jets were used in this analysis. A problematic response to charged particles in the region $|\eta| \in (1.0, 1.2)$ was identified during the first measurement [9]. In this region, the rate of good tracks changes abruptly by 20% due to the impact of barrel to end-cap transition in the SCT. To reduce the impact of ID regions with this problematic response on the measurement, jets with $1.0 < |y| < 1.2$ were excluded from the analysis. These jets have very likely the leading particle pointing to a problematic region and therefore a possible bias namely at charged particle high-p_{T} can occur for those jets. In the default configuration of this analysis reconstructed jets are selected to have $p_{\mathrm{T}} > 100$ GeV which ensures a region where both, the HLT and offline jet reconstruction are fully efficient.

To explore the properties of the jet modifications as a function of the rapidity, the jets are reconstructed in four rapidity regions: $|y| < 0.3$, $0.3 < |y| < 0.8$, $1.2 < |y| < 2.1$, and $|y| < 2.1$. These regions were selected to match the selections made in the analysis of inclusive jet suppression [12] which allows to build a solid connections between these two measurements.

Track-quality selection requirements consist of cuts on the number of hits in different subdetectors of ID and cuts on the pointing of tracks to the primary vertex. The longitudinal (z_0) and transverse (d_0) impact parameter of the track measured with respect to the primary vertex are scaled by their errors d_0^{cov}, z_0^{cov}, $\sin\theta^{cov}$, and $\mathrm{cov}(d_0, \theta)$ (see Fig. A.7 and A.8 in Appendix A) which defines a significance of the impact parameter (σ_{z_0} and σ_{d_0}). The cuts on significance introduce a natural p_{T} scaling of pointing cuts as shown in Ref. [90]. For the Pb+Pb data and MC, the list of default track-quality selection requirements is the following

- at least two hits in the Pixel ID
- at least seven hits in the Semiconductor Tracker (SCT)
- at least one hit in the first layer of the Pixel ID (BLayer) if expected
- $\sigma_{d_0} \equiv \frac{d_0}{\sqrt{d_0^{cov}}} < 3$
- $\sigma_{z_0} \equiv \frac{z_0 \sin\theta}{\sqrt{z_0^{cov} \sin^2\theta + \sin\theta^{cov}(z_0\cos\theta)^2}} < 3$

For *pp* data and MC, the last two cuts on pointing were relaxed and on top of the requirements on hits, requirements on d_0 and $z_0 \sin(\theta)$ were imposed on tracks. In total, the track-quality selection requirements in *pp* are the following

- at least one hits in the Pixel ID
- at least six hits in the Semiconductor Tracker (SCT)
- at least one hit in the first layer of the Pixel ID (BLayer) if expected
- $|z_0 \sin(\theta)| < 1.5$ mm
- d_0 impact parameter was parametrized in the region of $p_{\mathrm{T}}^{\mathrm{trk}} \in (1-100)$ GeV as a function of $p_{\mathrm{T}}^{\mathrm{trk}}$ as follows:

$$d_0(p_{\mathrm{T}}^{\mathrm{trk}}) = a_0 e^{a_1 p_{\mathrm{T}}^{\mathrm{trk}}} + a_2 e^{a_3 p_{\mathrm{T}}^{\mathrm{trk}}} \tag{4.9}$$

  where a_i represent free parameters of the fit. This parametrisation was chosen to guarantee a smooth behaviour of the d_0 parameter as a function of track momentum. The fitting parametrisation was set to meet the following criteria: $d_0(1\text{ GeV}) = 0.6$ mm, $d_0(10\text{ GeV}) = 0.3$ mm, $d_0(100\text{ GeV}) = 0.2$ mm. The fitted parameters are then as follows: $a_0 = 0.47$, $a_1 = -0.15$, $a_2 = 0.19$, $a_3 = 0.34 \cdot 10^{-4}$.

This cut configuration guaranties a removal of high-p_{T} fake tracks as demonstrated in the measurement of nuclear modification factor of charged particles at high-p_{T}, Ref. [91]. Spectra of reconstructed tracks and fake tracks are show in Appendix A in Fig.A.1. Also more tracking performance plot are shown in Figs. A.3 and A.4. The impact parameter d_0 as a function of track momentum is shown in Fig. A.5 as well as $z_0 \sin(\theta)$ in Fig. A.6.

4.3.2 Tracking efficiency correction

The tracking efficiency correction has been derived using the MC PYTHIA di-jet events described in Sections 4.2.4 and 4.2.3. The track to particle matching has been performed using the hit pattern matching cuts and the tracks with the *trk_mc_probability* > 0.5 were allowed to match the PYTHIA particles[2]. The

[2] *trk_mc_probability* is defined as $(10 \times N_{Pix}^{common} + 10 \times N_{SCT}^{common})/(5 \times N_{Pix}^{trk} + 5 \times N_{SCT}^{trk})$, where the number of hits common to the generated particle and the reconstructed track for both Pixel and SCT detectors, N_{Pix}^{common} and N_{SCT}^{common} are compared to the number of hits which form the track N_{Pix}^{trk} and N_{SCT}^{trk} with weights 5, resp. 10.

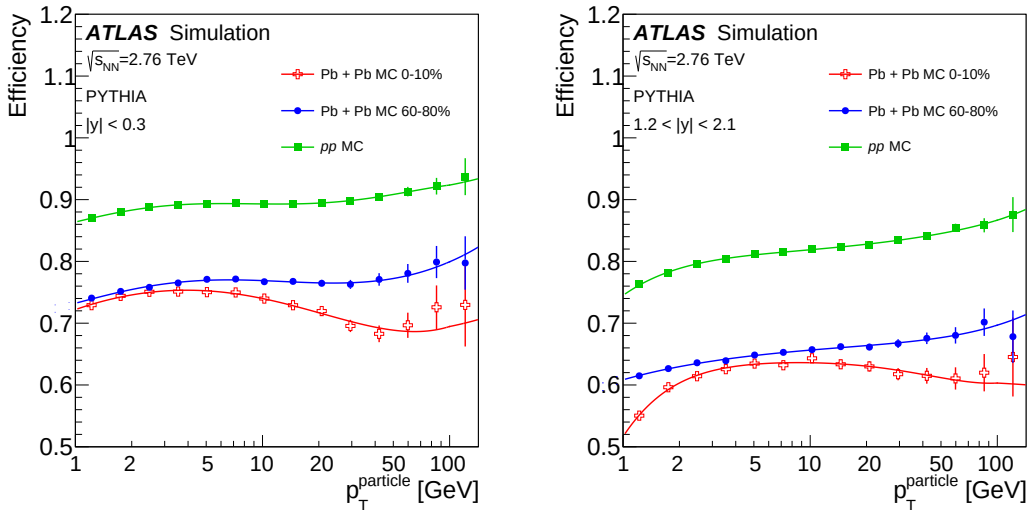

Figure 4.2: The tracking efficiency evaluated for particles in jets with $p_{\mathrm{T}} > 100$ GeV as a function of p_T^{ptc} for $|y| < 0.3$ (left) and $1.2 < |y| < 2.1$ (right). Efficiency is shown for central and peripheral Pb+Pb collisions as well as for pp MC. The full line represents the parametrization (for more details see the text).

same procedure was used e.g. in the measurement of inclusive charged particles or in the previous fragmentation analysis where alternatives to this procedure were tested.

Only tracks and truth particles associated to $R = 0.4$ truth jets were used as the input to the efficiency correction. Jets were required to have $p_{\mathrm{T}} > 100$ GeV which is the p_{T} region where the measurement is performed. A typical behavior of the tracking efficiency as a function of $p_{\mathrm{T}}^{\mathrm{trk}}$ is following: first, the tracking efficiency increases at very low-$p_{\mathrm{T}}^{\mathrm{trk}}$, then it reaches a plateau at $3 - 8$ GeV, then it starts to slowly decrease, reaches a minimum at ≈ 30 GeV, and then it increases again. This evolution is centrality and pseudorapidity dependent. The slow decrease in intermediate charged particle p_{T} range was identified to be dominantly due the cuts on pointing significance, namely due to the missing $\mathrm{cov}(d_0, \theta)$ term of the covariance matrix which is not properly booked in the case of Pb+Pb MC and data. This prevent us from defining the pointing significance using this term which in turns leads to this behavior. The origin of this feature was verified in pp collisions where the pointing cuts (which are not used in the default cut scheme) were constructed with and without the significance and the behaviour seen in heavy-ion collisions was reproduced. This behavior makes the fitting procedure more demanding, but does not represent any problem as will be seen from the next.

The tracking efficiency correction, $c(p_{\mathrm{T}}^{\mathrm{trk}})$ was evaluated from the tracking efficiency, $\varepsilon(p_{\mathrm{T}}^{\mathrm{trk}})$, as $c = 1/\varepsilon$. To guarantee a smooth behaviour of the correction factors as a function of track momentum, the tracking efficiency has been parametrized in the region of $p_{\mathrm{T}}^{\mathrm{trk}} = 1 - 90$ GeV using

$$\varepsilon(p_{\mathrm{T}}^{\mathrm{trk}}) = \sum_{i=0}^{4} a_i \log^i(p_{\mathrm{T}}^{\mathrm{trk}}) \tag{4.10}$$

where constants a_i represent free parameters of the fit. The tracking efficiency

correction was evaluated in seven centrality bins separately and also separately in pp MC. To capture the rapidity dependence of the tracking efficiency, the efficiency correction was evaluated in four different rapidity selections imposed on jets used in this analysis, namely $|y| < 0.3$, $0.3 < |y| < 0.8$, $1.2 < |y| < 2.1$, and $|y| < 2.1$. This leads in total to a set of 32 tracking efficiency correction functions. Example of tracking efficiencies evaluated in two rapidity regions (the most central and the most forward) for central and peripheral heavy-ion MC and pp MC is shown in Fig. 4.2. The functional form (4.10) can well describe the onset of the efficiency at low charged particle p_{T} as well as the structure in the intermediate-p_{T} region. At the same time it is not susceptible to statistical fluctuations in these regions. The study of the high charged particle p_{T} behaviour in different J-samples[3], both in pp and Pb+Pb simulation has shown that the tracking efficiency continues in general to follow the trends present at $p_{\mathrm{T}} < 90$ GeV. Thus, the result of the fit using (4.10) for tracks with $p_{\mathrm{T}} > 90$ GeV is replaced by a linear efficiency with the slope determined from the difference of the fit in $p_{\mathrm{T}} = 70$ GeV and $p_{\mathrm{T}} = 90$ GeV. This guarantees no susceptibility to the statistical fluctuations at high-pt which are present in Fig. 4.2.

4.3.3 Underlying event subtraction

The jets are corrected for the underlying event (UE) contribution during the jet reconstruction as described in Sec. 3.1. The measured distributions, which do not involve only calorimeter jets but also the charged particles, have to be corrected for the UE contribution too since there is no UE event subtraction running in the ID during the reconstruction. Thus, the $D(p_{\mathrm{T}})$ and $D(z)$ distributions were corrected for the presence of the UE underneath the jet as stated in Sec. 4.1.1.

This UE background depends on $p_{\mathrm{T}}^{\mathrm{ch}}$, η and the centrality of the collision. The contribution of the UE background was evaluated for each measured jet using a grid of $R = 0.4$ cones that spanned the full coverage of the inner detector. The cones had a fixed distance between their centroids chosen such that the coverage of the inner detector was maximized while the cones do not overlap each other. Any such cone having a charged particle with $p_{\mathrm{T}}^{\mathrm{ch}} > 6$ GeV or having a distance between its centroid and the nearest jet with $p_{\mathrm{T}} > 100$ GeV smaller then 0.4 was assumed to be associated with a real jet in the event and was excluded from the UE background determination (this choice of the parameters is justified by a good performance and it is discussed in Sec. 4.5.3).

The resulting UE charged particle yields, $\mathrm{d}n_{\mathrm{ch}}^{\mathrm{UE}}/\mathrm{d}p_{\mathrm{T}}^{\mathrm{ch}}$ or $\mathrm{d}n_{\mathrm{ch}}^{\mathrm{UE}}/\mathrm{d}z$, were evaluated over $1 < p_{\mathrm{T}}^{\mathrm{ch}} < 6$ GeV as a function of charged particle $p_{\mathrm{T}}^{\mathrm{ch}}$, $p_{\mathrm{T}}^{\mathrm{jet}}$, and y^{jet} and averaged over all cones according to:

$$\frac{\mathrm{d}n_{\mathrm{ch}}^{\mathrm{UE}}}{\mathrm{d}p_{\mathrm{T}}^{\mathrm{ch}}} = \frac{1}{N_{\mathrm{cone}}}\frac{1}{\varepsilon}\frac{\Delta N_{\mathrm{ch}}^{\mathrm{cone}}(p_{\mathrm{T}}^{\mathrm{ch}}, p_{\mathrm{T}}^{\mathrm{jet}}, y^{\mathrm{jet}})}{\Delta p_{\mathrm{T}}^{\mathrm{ch}}}, \tag{4.11}$$

$$\frac{\mathrm{d}n_{\mathrm{ch}}^{\mathrm{UE}}}{\mathrm{d}z} = \frac{1}{N_{\mathrm{cone}}}\frac{1}{\varepsilon}\frac{\Delta N_{\mathrm{ch}}^{\mathrm{cone}}(z, p_{\mathrm{T}}^{\mathrm{jet}}, y^{\mathrm{jet}})}{\Delta z}\bigg|_{z=\frac{p_{\mathrm{T}}^{\mathrm{ch}}}{p_{\mathrm{T}}^{\mathrm{jet}}}\cos\Delta R}. \tag{4.12}$$

Here N_{cone} represents the number of background cones associated with a given jet with $p_{\mathrm{T}}^{\mathrm{jet}}$ and y^{jet}, $\Delta N_{\mathrm{ch}}^{\mathrm{cone}}$ is the number of charged particles summed across all

[3]J-samples are defined in Sec. 4.2.3

cones associated to the jet in question, and ΔR represents the distance between the centroid of a cone and the position of a given charged particle. By evaluating the UE yields only from events containing jets included in the analysis, the background automatically had the correct distribution of centralities within a given centrality bin.

Not shown in Eqs. (4.11) and (4.12) is a correction factor that was applied to each background cone to correct for the difference in the average UE particle yield at a given $p_{\mathrm{T}}^{\mathrm{ch}}$ between the η position of the cone and y^{jet}, and a separate correction factor to account for the difference in the elliptic flow modulation at the ϕ position of the UE cone and ϕ^{jet}. These corrections are described separately in Sec. 4.3.3.

The UE yields need to be further corrected for the correlation between the actual UE yield underneath the jet and a finite, centrality dependent jet energy resolution. The details on this correction are provided in Sec. 4.3.3. The corrected UE distributions, $\mathrm{d}\tilde{n}_{\mathrm{ch}}^{\mathrm{UE}}/\mathrm{d}p_{\mathrm{T}}^{\mathrm{ch}}$ and $\mathrm{d}\tilde{n}_{\mathrm{ch}}^{\mathrm{UE}}/\mathrm{d}z$, were then subtracted from measured distributions as stated in Eqs. 4.3 and 4.4.

Correction for flow and η-dependence

The elliptic flow correction was based on a parameterization of the $p_{\mathrm{T}}^{\mathrm{ch}}$ and centrality dependence of previously measured elliptic flow coefficients, v_2 [69, 92]. The correction factor for the elliptic flow in $0-10\%$ central collisions is shown in the left plot of Fig. 4.3. The correction factor is evaluated as a function of the distance of a jet from the reaction plane, $\cos 2(\phi_{jet} - \Psi)$ where Ψ is the phase. One can see that the flow correction is less than one for jets that are oriented in the direction perpendicular to the reaction plane and greater than one for jets oriented in the direction of the reaction plane. Jets oriented in the direction perpendicular to the reaction plane ($\cos 2(\phi_{jet} - \Psi) = -1$) contain typically less UE particles and therefore the UE cone located at a random position in the ID is typically corrected down by the flow factor. Jets oriented in the direction of the reaction plane ($\cos 2(\phi_{jet} - \Psi) = +1$) have typically larger yields of particles and therefore the background located at a random position in the ID is typically corrected up by the flow factor. Since the measurement was not performed with respect to the reaction plane, the impact of the flow correction was at the level of few percent of the magnitude of UE yields.

The correction to a difference in the yields of UE particles at a position of the jet and at a position of the track entering the UE estimate is done based on the parameterization of inclusive yields of charged particles evaluated as a function of pseudorapidity. The inclusive yields of charged particles were measured using efficiency corrected tracks with $p_{\mathrm{T}} > 1$ GeV. The illustration of yields for central and peripheral collisions are presented in the right plot of Fig. 4.3. The correction is then a ratio of the values of pseudorapidity distribution in the position of a jet and position of the track used for the calculation of the UE estimate.

Correction for correlation of underlying event and jet energy resolution

The obtained UE distributions need to be rescaled prior applying the subtraction in order to take into account the interplay between the UE and the JER which we will now briefly describe. The UE distribution, $dn_{\mathrm{ch}}^{\mathrm{UE}}/dp_{\mathrm{T}}^{\mathrm{ch}}$, is observed to

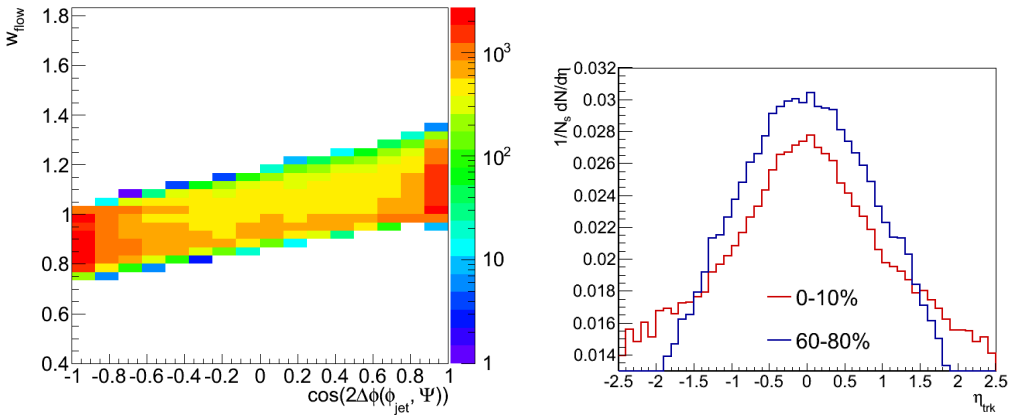

Figure 4.3: Left: The correction factor for the difference in the elliptic flow at a position of the jet and at a position of a track entering the estimate of the UE contribution evaluated as a function of the distance between the jet axis and the direction of the reaction plane. Right: Inclusive yields of charged particles measured using the efficiency corrected tracks evaluated as a function of pseudorapidity and for two different centrality bins.

be independent of $p_{\mathrm{T}}^{\mathrm{jet}}$ both in the data and MC. However, it was observed that the finite JER induces in the MC a difference between the extracted $dn_{\mathrm{ch}}^{\mathrm{UE}}/dp_{\mathrm{T}}^{\mathrm{ch}}$ and the actual UE contribution to reconstructed jets. The magnitude of this difference is centrality dependent and it also exhibits a modest $p_{\mathrm{T}}^{\mathrm{jet}}$ dependence. That difference was found to result from intrinsic correlations between the charged particle density in the UE and the MC $p_{\mathrm{T}}^{\mathrm{jet}}$ error, $\Delta p_{\mathrm{T}}^{\mathrm{jet}} = p_{\mathrm{T}}^{\mathrm{rec}} - p_{\mathrm{T}}^{\mathrm{truth}}$. In particular, jets with positive (negative) $\Delta p_{\mathrm{T}}^{\mathrm{jet}}$ are found to have an UE contribution larger (smaller) than jets with $\Delta p_{\mathrm{T}}^{\mathrm{jet}} \sim 0$. Due to the net upfeeding on the falling jet spectrum, the selection of jets above a given $p_{\mathrm{T}}^{\mathrm{jet}}$ threshold causes the UE contribution to be larger than that estimated from the above-described procedure. The average fractional mismatch in the estimated UE background was found to have minor dependence on $p_{\mathrm{T}}^{\mathrm{ch}}$, $p_{\mathrm{T}}^{\mathrm{jet}}$, and pseudorapidity and to vary with centrality by factors between 0–15% with respect to the original UE estimates. To correct for this effect, the centrality-, η-, $p_{\mathrm{T}}^{\mathrm{jet}}$- and $p_{\mathrm{T}}^{\mathrm{trk}}$-dependent multiplicative correction factors were applied on $dn_{\mathrm{ch}}^{\mathrm{UE}}/dp_{\mathrm{T}}^{\mathrm{ch}}$ distributions. The example of those factors is plotted as a function of $p_{\mathrm{T}}^{\mathrm{jet}}$ and $p_{\mathrm{T}}^{\mathrm{trk}}$ for 0–10% bin and for jets with $|y| < 2.1$ in Fig. 4.4. These weights were estimated as a ratio UE distributions calculated from tracks within the area of a jet which do not have an associated truth particle and the the UE distribution. This multiplicative weight thus removes the impact of the correlation between the UE and the finite JER. The performance of this procedure is demonstrated in Sec. 4.5.3.

An independent check of the subtraction of UE contribution from measured distributions was performed by estimating the UE charged particle p_{T} spectra from the minimum bias data sample. In this method we book the full event from minimum bias stream in a multidimensional histogram (p_{T}, η, ϕ, flow and centrality). The only condition is that there must not be a jet with $p_{\mathrm{T}} > 50$ GeV threshold in that event. If there is, then the event is not taken into account. Then, when looping over the hard-probes data, the multidimensional object was retrieved and we asked what is the UE in the cone around the jet axis in that

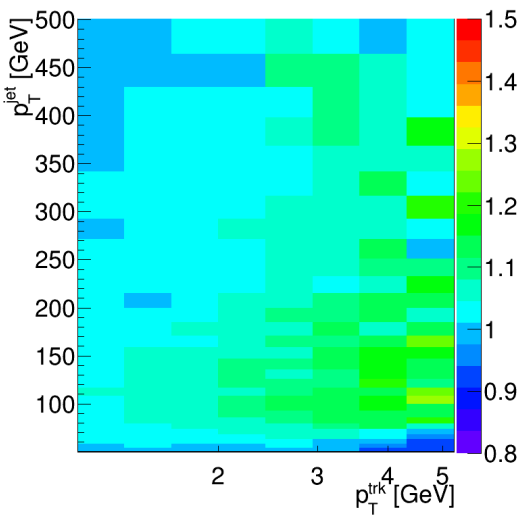

Figure 4.4: The multiplicative correction factors that correct for the correlation between the UE and the JER (for more details see the text).

multidimensional object. That UE is booked and subtracted offline. After applying centrality reweighting, these UE charged particle p_{T} spectra were found to be consistent within statistical uncertainties with UE distributions obtained by the cone method. This is illustrated in Fig. 4.5.

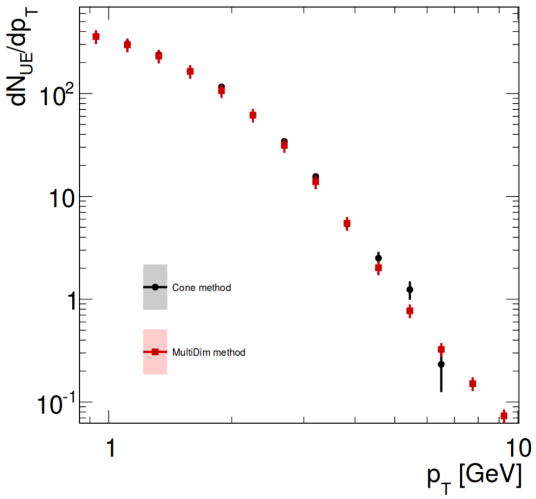

Figure 4.5: Check of the subtraction of the UE contribution. The UE from the default cone method is compared with an alternative method based on calculating the background based in the minimum bias stream.

4.3.4 b-jet exclusion

The fragmentation of b-jets differs from the fragmentation of light quark jets. Since the fraction of b-jets can be different in central and peripheral collisions in the data it is reasonable to maximally reduce the b-jet component from the study. To do so we exclude jets containing reconstructed muons. The muon to jet association was based on the distance cut of $\Delta R = \sqrt{\Delta\eta^2 + \Delta\phi^2} < 0.4$. These

combined muons have to fulfill the following criteria: $p_T > 4$ GeV, at least 1 Pixel hit, at least 1 B-layer hit, at least 7 SCT hits, sum SCT and Pixel holes less then two, no SCT holes, match χ^2/ndof < 10, $|d_0^{PV}| < 5$ mm, $|z_0^{PV}| < 5$ mm, momentum measured by ID $p_{ID} > 3$ GeV, and momentum measured by the Muon Spectrometer $p_{muon} > 0.1$ GeV. These criteria has been adopted from the open heavy flavor working group.The overall reduction of the jets due to b-jet exclusion is found to be about 0.9% both in central and peripheral collisions.

4.3.5 Bad jet exclusion

The jets reconstructed in pp events were required not be `isUgly` and `isBadMedium`, in details described in [93]. It was shown in past analyses that the jets reconstructed in Pb+Pb collisions are not susceptible to problems occurring in higher luminosity pp running such as noise bursts. However, in Pb+Pb collisions, false jets can typically appear at low p_{T}. These false jets come from correlated UE fluctuations that are reconstructed as jets. The matching of reconstructed jets with track jets and EM clusters is typically applied to remove the false jets. Since this analysis works with jets with $p_{\mathrm{T}} > 100$ GeV we see that there is practically no contribution from false jets. Thus, the procedure of the false jet rejection was not applied in the analysis.

4.3.6 Jet isolation

Both reco and truth jets were required to be isolated. Any jet having another jet with high p_{T} in its vicinity ($\Delta R < 1.0$) has been discarded. The p_{T} isolation threshold has been selected to be the p_{T} of the test jet. Jet isolation has been required in order not to bias the fragmentation measurement by a potential presence of split jets that might occur more frequently in data compared to MC. Split jets are jets that should be reconstructed as a one jet but during the jet reconstruction they were badly reconstructed as a individuals jet. This requirement rejects less then 1% of jets.

4.3.7 Monte-Carlo reweighting

As shown e.g. in the measurement of fragmentation functions in pp at $\sqrt{s} =$ 7 TeV, the PYTHIA6 MC describes the jet fragmentation with an accuracy of 10–20%. This was seen also when comparing raw reconstructed data with raw reconstructed MC in our measurement. Furthermore, there is also a difference in the fragmentation functions between pp simulation and Pb+Pb simulation up to 5%. Consequently, in order to define the response matrices for the unfolding, both MC samples were reweighted separately to match the data in pp collisions. The reweighting factors were defined from a parameterization of the ratios of the raw reconstructed data to raw reconstructed MC and were applied as p_{T}-dependent weights assigned to each particle entering the measurement (that is each MC track entering a given histogram enters with an additional weight).

While Bayesian or SVD unfolding are not very sensitive to the differences in the shape of the MC and data, it is better to make the MC more close to the real data by applying this reweighting. Systematic uncertainty connected with the unfolding and reweighting is discussed in Sec. 4.4.

4.4 Systematic uncertainties

The systematics uncertainties related with jet energy scale (JES), jet energy resolution (JER), charged tracks reconstruction and unfolding procedure were evaluated separately for each centrality and rapidity bin for distributions and their ratios. The size of combined systematic uncertainty and it's sources for selected centrality and rapidity bins are in Fig. 4.7 and more in A.9.

The systematic uncertainty related to the JES consists of two contributions: the *pp* [94] and the heavy-ion JES uncertainty [95]. The jet energy scale uncertainty was evaluated by shifting the transverse momentum of reconstructed jets as:

$$p'_{\mathrm{T}} = p_{\mathrm{T}} \cdot (1 \pm U^{\mathrm{JES}}(p_{\mathrm{T}}, y)) \tag{4.13}$$

where $U^{\mathrm{JES}}(p_{\mathrm{T}}, y)$ is ether the *pp* or the heavy-ion transverse momentum and rapidity dependent JES uncertainty. The $D(p_{\mathrm{T}})$ and $D(z)$ distributions with shifted p'_{T} were obtained for each rapidity and centrality bin and then unfolded and compared to the original distributions. The JES uncertainty is usually below 2% in *pp* collisions but can reach up to 4% and 6% at high p_{T} and z, respectively. In Pb+Pb collisions, the JES uncertainty can reach up to 15% at the largest p_{T} or z but typically the modulation is the same as in *pp*. In the ratios, the JES uncertainty partially cancels and it is typically below 1% and at high p_{T} it is below 10%.

To cover for a possible disagreement between JER in the simulation and data, the JER systematic uncertainty was obtained by modifying the response matrix which was generated with the reconstructed jets p_{T} smeared by an uncertainty estimated as a function of rapidity and jet p_{T} [94]. The JER uncertainty is below 1% but it can reach up to 6% at high p_{T} or z.

The track reconstruction was performed with the "standard" sets of selection criteria, for more details see Sec. 4.3. The track reconstruction systematics uncertainty was obtained by performing the analysis with "loose" and "tight" sets of of tracks selection criteria separately for each pseudorapidity bin in *pp* collisions and additionally for each centrality bin in heavy-ion collisions. The selection criteria are summarized in Tables 4.2, 4.3 together with the "standard" sets of cuts. The variation of tracking efficiencies for heavy-ion collisions are plotted in Fig. 4.6 for all three different sets of selection criteria. The "tight" criteria reduce the tracking efficiency by a 15–20% and "loose" selection criteria enhance tracking efficiency by 5–10%. The track reconstruction systematic uncertainty is typically less then 4% and it is the largest at low and intermediate p_{T} or z. Additionally, the second systematics uncertainty due to track reconstruction is related with the parametrisation of tracking efficiencies that is less then 2%.

The systematic uncertainty related to the unfolding procedure has two components. The first one is based on the different number of iteration used in the unfolding. The number of iterations was varied by ± 1. For the second one, the data were unfolded with the response matrix that was reweighted to match the data. These uncertainties were found negligible and typically are below 1%. To determine the total systematic uncertainty, the systematic uncertainties from all different sources were added in quadrature.

Heavy-ion			
Parameter	Loose	Standard	Tight
#SCT hits	$>= 6$	$>= 7$	$>= 8$
#Pixel hits	$>= 1$	$>= 2$	$>= 3$
Pixel B-layer hit	–	if expected	if expected
d_0/σ_{d_0}	< 3.5	< 3	< 2.5
$z_0 \sin\theta/\sigma_{z_0 \sin\theta}$	< 3.5	< 3	< 2.5
Proton-proton			
Parameter	Loose	Standard	Tight
#SCT hits	$>= 6$	$>= 6$	$>= 7$
#Pixel hits	$>= 1$	$>= 1$	$>= 1$
Pixel b-layer hit	if expected	if expected	if expected
#Pixel holes	–	–	$= 0$
#SCT holes	–	–	< 2
$\lvert z_0 \sin(\theta)\rvert$ [mm]	< 2.0	< 1.5	< 1.0
χ^2/ndf	–	–	< 6

Table 4.2: Different tracking selection criteria used for the estimate of one of sources of systematic uncertainties due to tracking. The impact parameter d_0, used in *pp* collisions, is summarized in Tab. 4.3.

Parametrisation of the impact parameter d_0 [mm]			
	Loose	Standard	Tight
d_0(1 GeV)	0.9	0.6	0.4
d_0(10 GeV)	0.4	0.3	0.2
d_0(100 GeV)	0.2	0.2	0.2
Parameters of the fit			
Parameter	Loose	Standard	Tight
a_0	0.94	0.47	0.29
a_1	-0.14	-0.15	-0.37
a_2	0.18	0.19	0.20
a_3	$0.85 \cdot 10^{-3}$	$0.33 \cdot 10^{-3}$	$-0.16 \cdot 10^{-4}$

Table 4.3: The different tracking selection criteria of the impact parameter d_0 used for the estimate of one of sources of systematic uncertainties in *pp* collisions. The impart parameter was parametrised by Eq. 4.9 with four free parameters a_i. The fitting parametrisation was set to meet the criteria of the impact parameter d_0 stated in the upper table. The results of the fits are then listed in the lower part of the table.

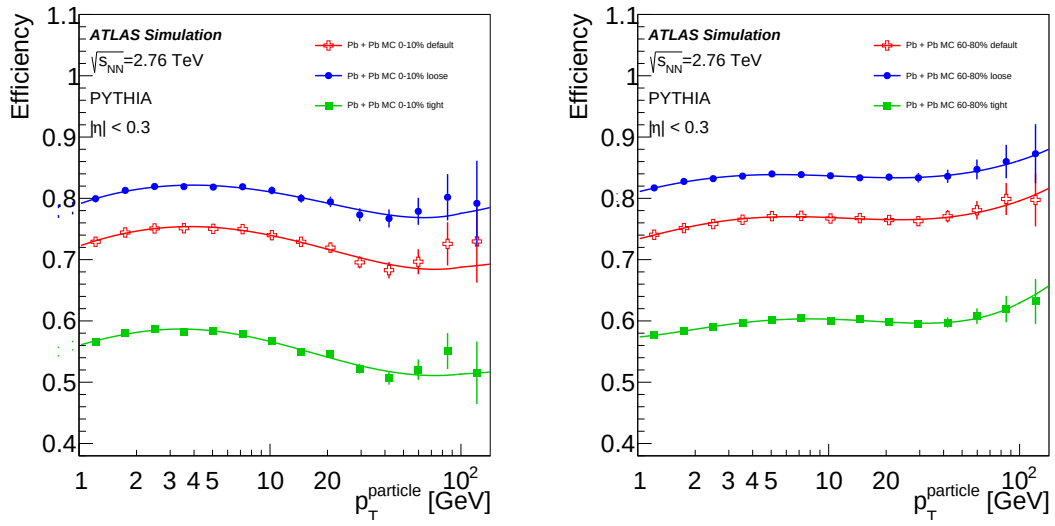

Figure 4.6: Tracking efficiencies along with the parametrization for "standard", "loose" and "tight" sets of selection criteria for central (left) and peripheral (right) heavy-ion collisions in jets with $|y| < 0.3$.

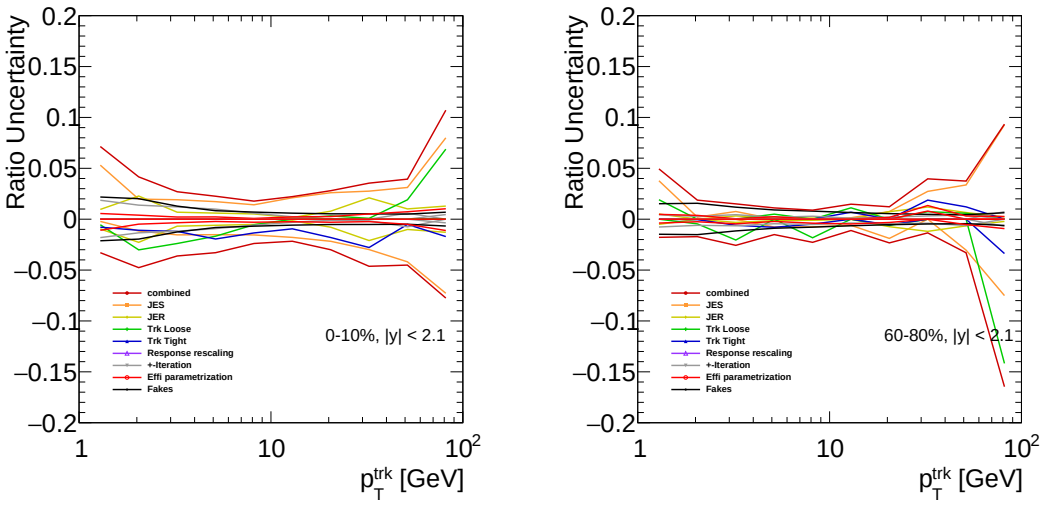

Figure 4.7: Size of the positive and negative systematic uncertainty and it's sources for $R_{D(p_{\mathrm{T}})}$ ratios in inclusive rapidity bin for jets with $p_{\mathrm{T}} > 100$ GeV for central (left) and peripheral (right) collisions.

4.5 Results

In this section we present results of the measurement. The measurement of the jet internal structure is performed differentially in the jet momentum and jet rapidity and for two collision systems, pp and Pb+Pb. In the case of Pb+Pb collisions, the measurement is performed in seven bins of centrality of the collision, $0-10\%,\ 10-20\%,\ 20-30\%,\ 30-40\%,\ 40-50\%,\ 50-60\%$, and $60-80\%$.

The measured distributions are evaluated in four different jet rapidity intervals: $|y| < 2.1$, $|y| < 0.3$, $0.3 < |y| < 0.8$, and $1.2 < |y| < 2.1$. The rapidity interval of $0.8 < |y| < 1.2$ is not considered in the analysis since localized drops in the efficiency corresponding to the transition between the SCT barrel and end-cap do not allow to obtain result with sufficient precision. The distributions are also evaluated in four different jet p_{T} intervals: $p_{\mathrm{T}} = 100 - 398$ GeV, $p_{\mathrm{T}} = 100 - 126$ GeV, $p_{\mathrm{T}} = 126 - 158$ GeV, and $p_{\mathrm{T}} = 158 - 398$ GeV. These intervals were chosen to correspond intervals selected in the measurement of jet nuclear modification factor [12].

The content of this section is following: Sec. 4.5.1 presents the raw $D(p_{\mathrm{T}})$ distributions in MC. Sec. 4.5.2 presents the raw distributions measured in the data. Sec. 4.5.3 introduces the unfolding procedure and presents unfolded distributions in MC. Sec. 4.5.4 presents the unfolded distributions measured in the data, that is the central result of this study.

4.5.1 Raw distributions in Monte Carlo

In this section, we evaluate different ratios in MC to demonstrate the impact of detector effects on the measured distributions and to advocate the strategy used in this analysis. There are two types of ratios that one can do in MC to better understand the impact of detector effects:

- Ratio of raw reconstructed distributions to truth distributions.
- Ratio of raw reconstructed to truth distributions where the reconstructed jet p_{T} was replaced by the truth jet p_{T}.

These ratios are discussed in next two subsections.

Ratio of reconstructed distributions to truth distributions

The Monte Carlo ratios of raw reconstructed fragmentation distributions to the same quantity evaluated in the truth provide a basic information about the impact of detector effects on the measured distributions. We start-off showing the "out-of-box" ratios where we apply only basic corrections: standard jet energy scale calibration, tracking efficiency correction (see Sec. 4.3.2), and subtraction of UE distributions (see Sec. 4.3.3). The former two are the standard corrections applied e.g. in the study of inclusive jet spectra [12, 11] or inclusive spectra of charged particles [91], the subtraction of UE distribution is characteristic for fragmentation studies. The results for different centralities and different rapidity selections are shown in Fig. 4.8. In an ideal world this ratio would be unity. However, this is clearly not the case. In the next sections we will discuss the sources of this "non-closure" and the strategy how to correct for it.

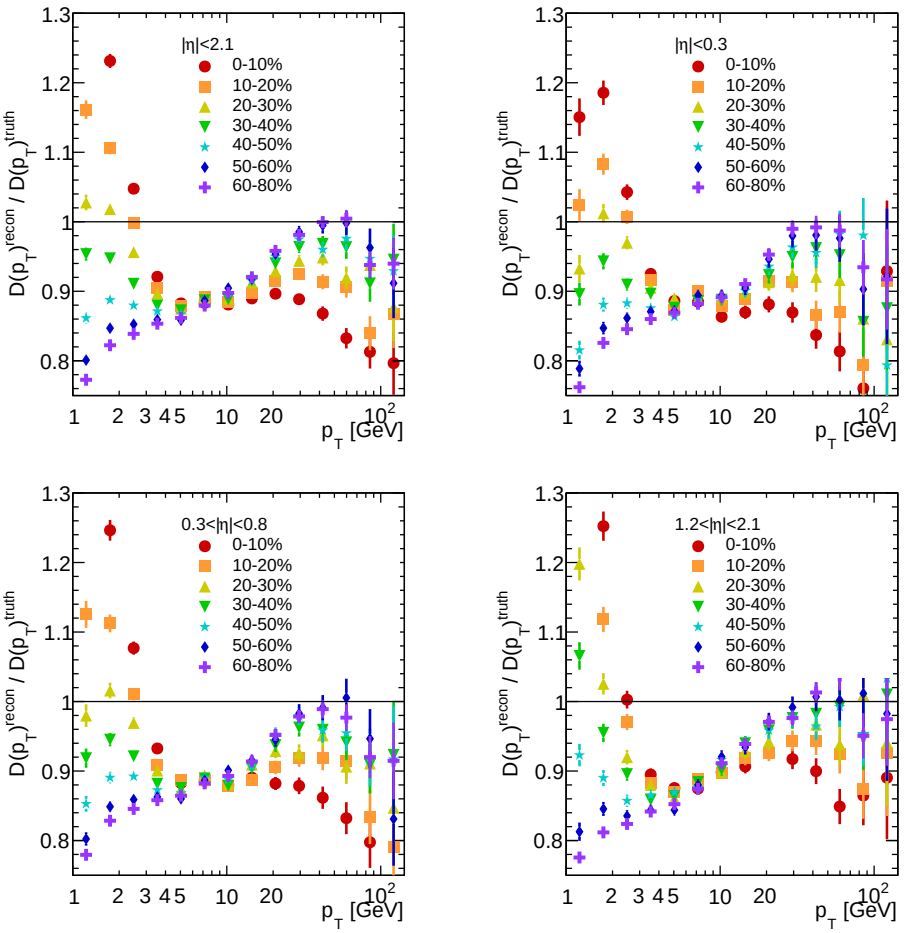

Figure 4.8: The ratio of MC reconstructed $D(p_{\mathrm{T}})$ distributions to the truth $D(p_{\mathrm{T}})$ distributions. Only standard basic corrections were applied on reconstructed distributions (for more details see the text). The distributions are evaluated for jets with $p_{\mathrm{T}} > 100$ GeV. Four panels show four different rapidity selections, different markers show distributions evaluated for different centrality bins as labelled in the legend.

Ratio of reconstructed to truth distributions with replaced reconstructed jet p_{T} by truth jet p_{T}

To understand the impact of different effects on the reconstructed to truth ratios, we can factorize out the impact of the jet energy resolution (JER) on those ratios by replacing the reconstructed jet p_{T} by a truth jet p_{T}. This leaves the reconstructed distributions being affected only by UE subtraction and track momentum resolution. The result is shown in Fig. 4.9. One can see that the ratio recovers the unity (compared to Fig. 4.8) except at low p_{T} and at very high p_{T}. At high-p_{T} the track momentum resolution comes into the play (if the track momentum is also replaced by a momentum of a corresponding truth particle, the ratio is unity within statistical uncertainties in the whole p_{T} region). The departure from unity seen at low p_{T} is due to the fact that UE correction factors described in Sec. 4.3.3 cannot work correctly once the jet sample is selected based on the cut on truth p_{T} instead of reconstructed p_{T}.

Figure 4.9 does not represent any closure test, but in comparison with Fig. 4.8

(no replacement of the jet p_{T}), it demonstrates that the measured distributions are influenced mainly by the JER and that the impact of track momentum resolution is small (but still needs to be unfolded). The real "closure test" of the ability to go from the reconstructed level back to the hadron level is presented in the next section after the unfolding is introduced.

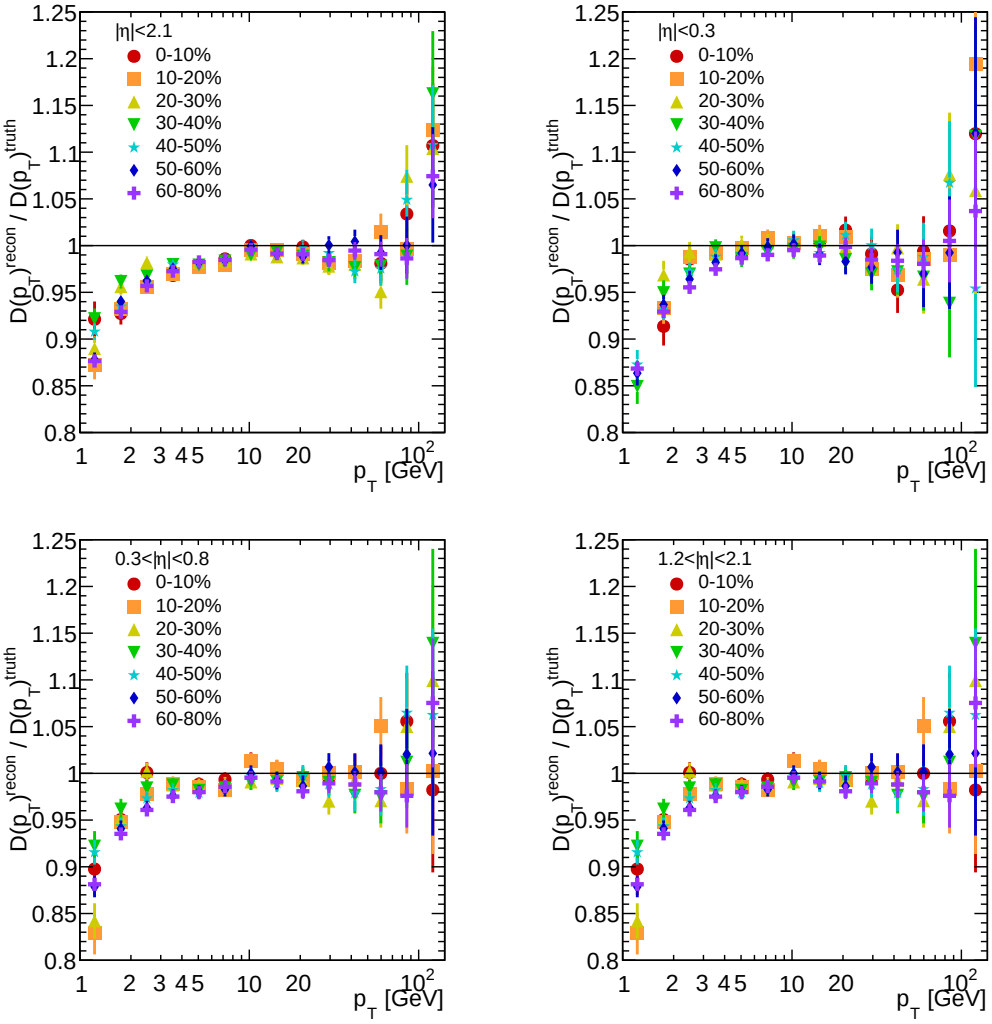

Figure 4.9: The ratio of MC reconstructed $D(p_{\mathrm{T}})$ distributions to the truth $D(p_{\mathrm{T}})$ distributions. The p_{T} of reconstructed jets was replaced by the p_{T} of truth jet (for more details see the text). The distributions are evaluated for jets with $p_{\mathrm{T}} >$ 100 GeV. Four panels show four different rapidity selections, different markers show distributions evaluated for different centrality bins as labelled in the legend.

4.5.2 Raw distributions in data

After building a confidence in the reconstruction procedure as discussed in Sec. 4.5.1, one can proceed with evaluating effects in the data. The fragmentation distribution were measured in the Pb+Pb and *pp* data. The *pp* collisions were used as a reference to quantify the effects of the jet quenching in heavy-ion collisions. The ratios were evaluated of fragmentation distributions measured in different centrality bins with respect to distributions measured in the *pp* collisions.

Fig. 4.10 shows the ratios of $D(p_{\mathrm{T}})$ distributions, $R_{D(p_{\mathrm{T}})}$, in seven centrality bins and four different rapidity selections.

These raw ratios are of course affected by the detector effects which remain to be unfolded. However, even at the raw level, we may conclude to see a characteristic behavior of these ratios, similar to that previously observed in [9], which is the following: the yields of charged particles at low p_{T} ($p_{\mathrm{T}} < 4$ GeV) are enhanced, yields of charged particles are suppressed in the intermediate p_{T} region ($4 < p_{\mathrm{T}} < 20$ GeV), and then the yields are again enhanced in the high p_{T} region ($p_{\mathrm{T}} > 20$ GeV).

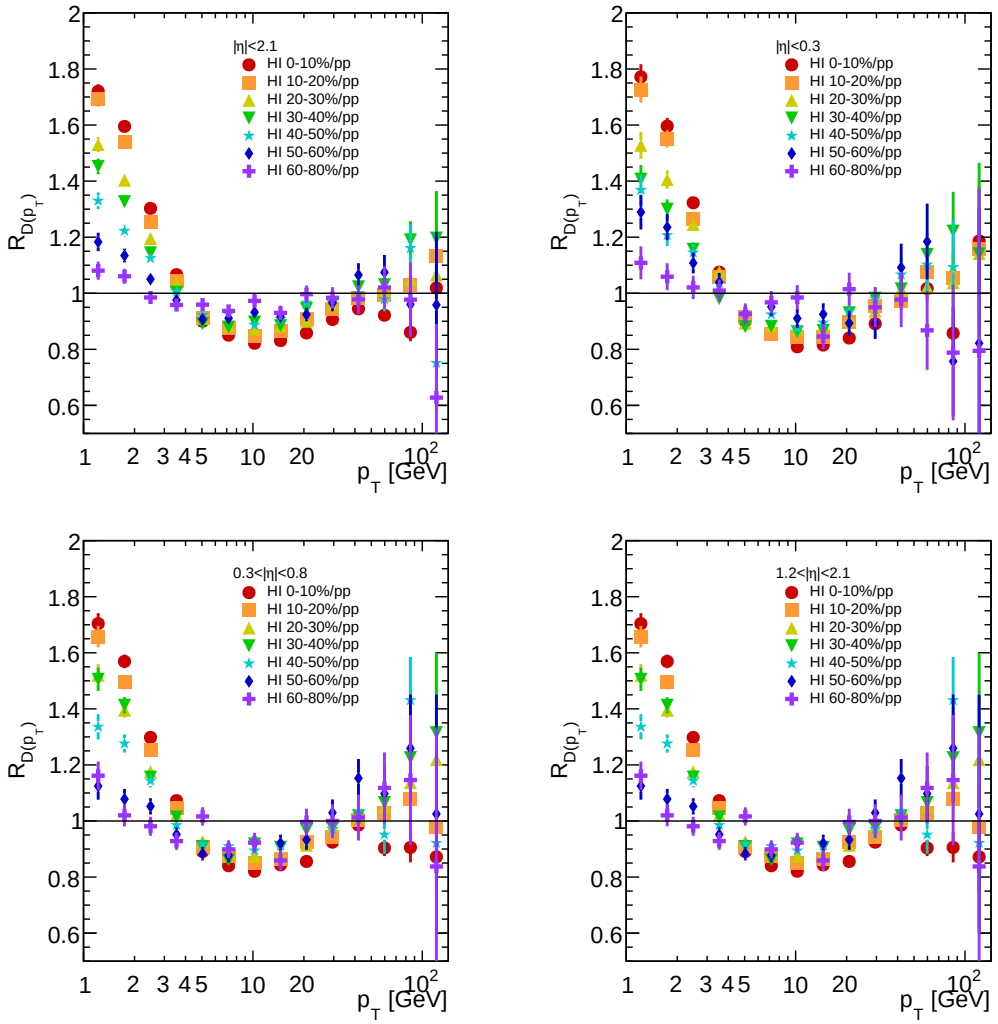

Figure 4.10: The ratio of raw $D(p_{\mathrm{T}})$ distributions measured in the heavy-ion collisions to $D(p_{\mathrm{T}})$ distributions measured in pp collisions for jets with $p_{\mathrm{T}} > 100$ GeV. Four panels show four different rapidity selections, different markers show distributions evaluated for different centrality bins as labelled in the legend.

4.5.3 Unfolding distributions in MC

To obtain the final results one has to correct for the detector effects by performing the unfolding. The two-dimensional Bayesian unfolding from the `RooUnfold` software package [87] based on Bayes theorem [86] was used to correct for the

finite resolution of the jet energy and track momentum simultaneously. Because the fragmentation functions are measured per jet, it is also necessary to unfold the jet spectra that were unfolded by a one-dimensional Bayesian unfolding.

To be able to perform a two-dimensional unfolding, four-dimensional response matrices had to be constructed using truth particle p_{T}, track p_{T}, truth jet p_{T} and reconstructed jet p_{T}. The response matrices were built for all the rapidity and centrality bins separately. An example of two-dimensional projections of the four-dimensional response matrices are shown in Fig. 4.11 together with profiles along the x-axis for Pb+Pb collisions for 0–10% centrality bin. The black line represents the diagonal. Because jets have worse momentum resolution than tracks, the response matrix for tracks is more narrow than for jets and has a smaller deviation from the mean values. At high-p_{T} the track response matrix is more off-diagonal because of the track momentum resolution.

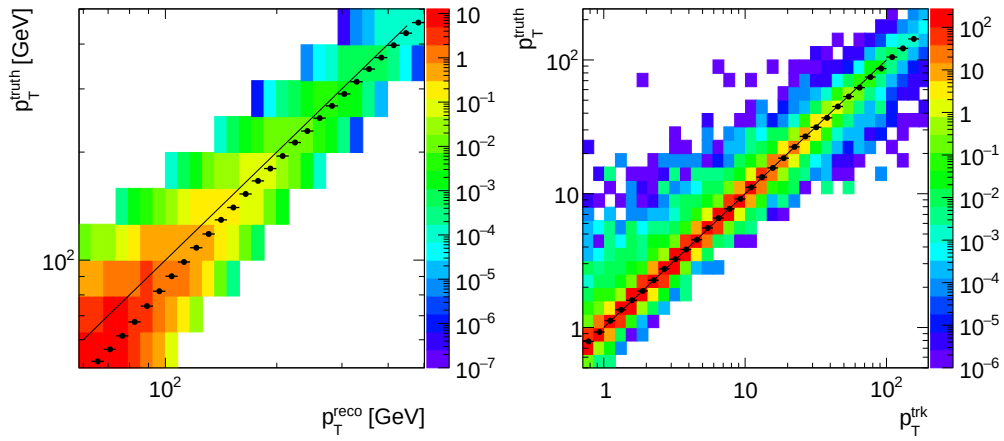

Figure 4.11: The two-dimensional projections from four-dimensional response matrices evaluated in Pb+Pb MC inclusive in rapidity for 0–10% central collisions. Left: 2D response matrix for jets. Right: 2D response matrix for tracks with jets $p_{\mathrm{T}} > 60$ GeV. Black markers show a profile along the x-axis. Black line is to guide the eye to see the diagonal.

To demonstrate the performance of the unfolding in MC, it is important to evaluate the ratio of unfolded reconstructed distributions to the truth distributions. The ratios for $D(p_{\mathrm{T}})$ and $D(z)$ distributions for all the rapidity and centrality bins in heavy-ions collisions as well as for all the rapidity bins for pp collisions are shown in Figs. 4.12 and 4.13. The ratios are within the statistical uncertainties within the unity. It demonstrates that the detector effects were fully corrected as well as the impact of the UE to the measured distributions. Based on the stability of the result to the number of iterations, the number of iterations was chosen to be five for all the centrality and rapidity bins both in Pb+Pb and pp collisions except for the 0-10% centrality bin where eight iterations were used. Unfolding of the jet spectra, used for the normalisation of the $D(p_{\mathrm{T}})$ and $D(z)$ distribution, is shown in Fig. 4.14.

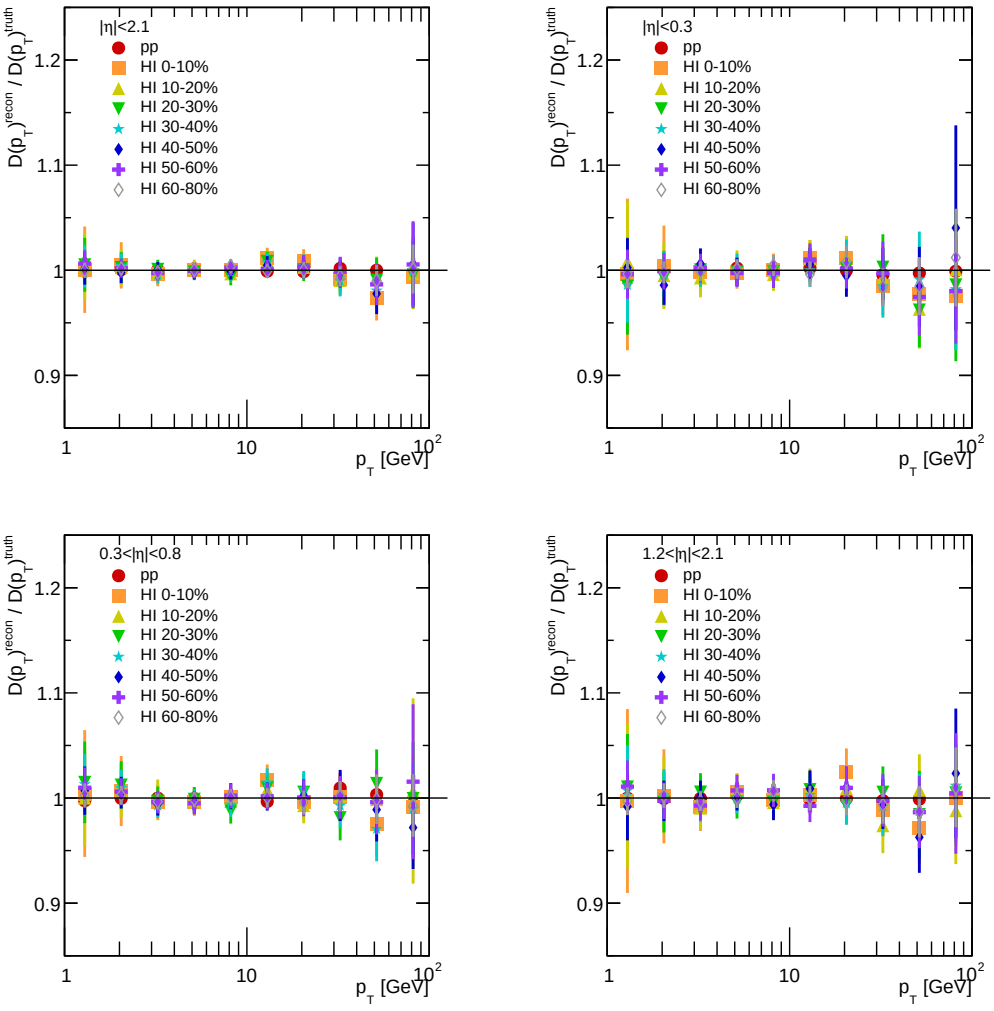

Figure 4.12: The ratio of MC reconstructed unfolded $D(p_{\mathrm{T}})$ distributions to the truth $D(p_{\mathrm{T}})$ distributions for jets with $p_{\mathrm{T}} > 100$ GeV. Four panels show four different rapidity selections, different markers show distributions evaluated for different centrality bins as labelled in the legend.

4.5.4 Unfolded distributions in data

This section presents the main result of the study. We plot the final result along with the systematic uncertainties which are discussed in details in Sec. 4.4.

The $D(p_{\mathrm{T}})$ and $D(z)$ distributions corrected to the hadron level by the unfolding procedure described in the previous section are shown in Fig. 4.15 and Fig. 4.16, respectively. Different panels show distributions evaluated for different rapidity intervals for jets with $100 < p_{\mathrm{T}} < 398$ GeV. The shaded band represents total systematic uncertainty, the error bars represent statistical uncertainties. The distributions exhibit a difference in shape between central heavy-ion collisions and peripheral heavy-ion collisions or the pp reference. To quantify this difference the ratios of $D(p_{\mathrm{T}})$ and $D(z)$ distributions measured in heavy-ion collisions to those measured in pp collisions were calculated and termed $R_{D(p_{\mathrm{T}})}$ and $R_{D(z)}$, respectively, following nomenclature introduced in Ref. [9].

The $R_{D(p_{\mathrm{T}})}$ and $R_{D(z)}$ distributions are shown in Figs. 4.17–4.20. Figure 4.17

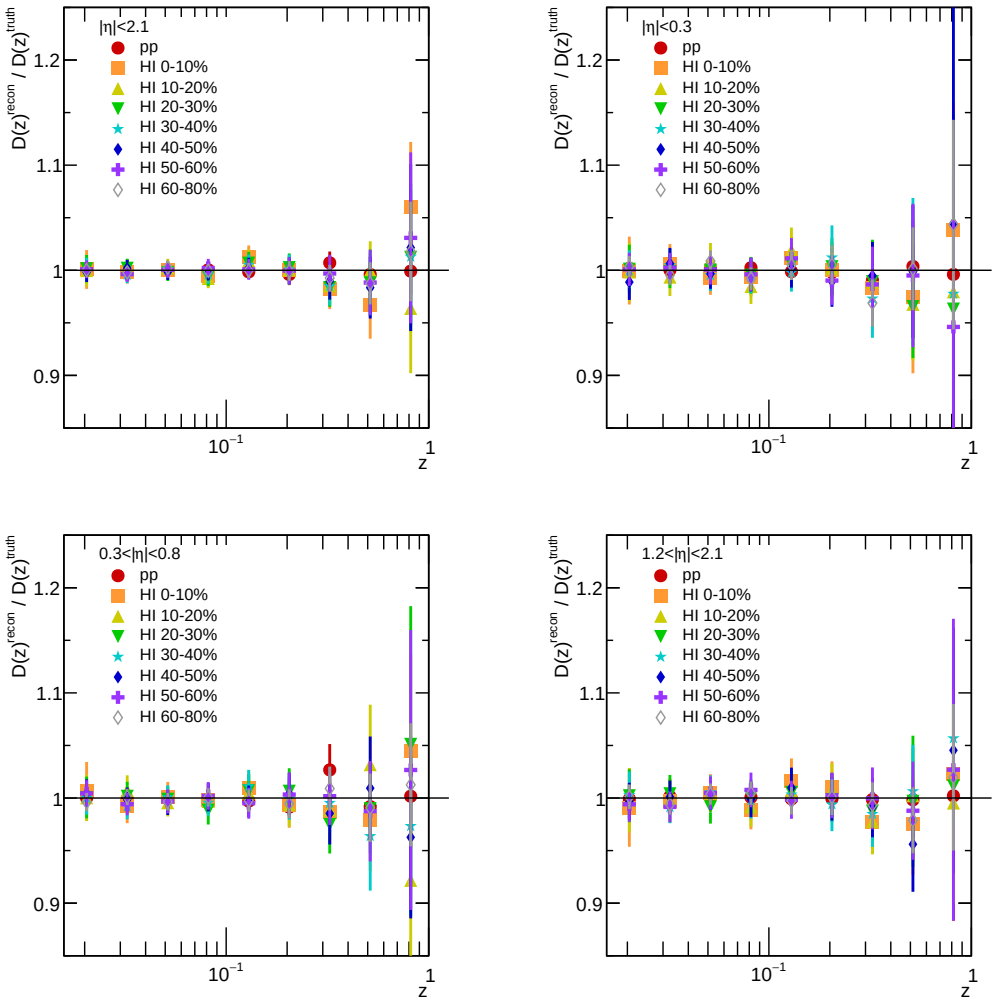

Figure 4.13: The ratio of MC reconstructed unfolded $D(z)$ distributions to the truth $D(z)$ distributions for jets with $p_{\mathrm{T}} > 100$ GeV. Four panels show four different rapidity selections, different markers show distributions evaluated for different centrality bins as labelled in the legend.

shows the $R_{D(p_{\mathrm{T}})}$ distributions for four selections in collision centrality, namely $0-10\%$, $20-30\%$, $30-40\%$ and $60-80\%$, and for four rapidity intervals of jets with $p_{\mathrm{T}}^{\mathrm{jet}}$ in the interval of 100–398 GeV. These ratios show an enhancement in fragment yield in central collisions for $p_{\mathrm{T}}^{\mathrm{ch}} < 4$ GeV, a reduction in fragment yields for $4 < p_{\mathrm{T}}^{\mathrm{ch}} < 25$ GeV and an enhancement in the fragment yield for $p_{\mathrm{T}}^{\mathrm{ch}} > 25$ GeV. The magnitude of these modifications decreases for more peripheral collisions. A similar observation can be made also for the $R_{D(z)}$ distributions shown in Fig. 4.18. The characteristic shape of these ratios was also seen in the previous study [9] where the $60-80\%$ bin was used as a reference. Figures 4.17 and 4.18 show that the difference in the modifications between different rapidity selections is marginal for fragments with $p_{\mathrm{T}}^{\mathrm{ch}} < 25$ GeV and $z < 0.25$, respectively. Only at high $p_{\mathrm{T}}^{\mathrm{ch}}$ or high z a change in the trend may be observed, where the enhancement is systematically lower for more forward jets compared to jets measured in the central rapidity region. Figure 4.19 and 4.20 show the $R_{D(p_{\mathrm{T}})}$ and $R_{D(z)}$ distributions, respectively, both for four $p_{\mathrm{T}}^{\mathrm{jet}}$ intervals of jets

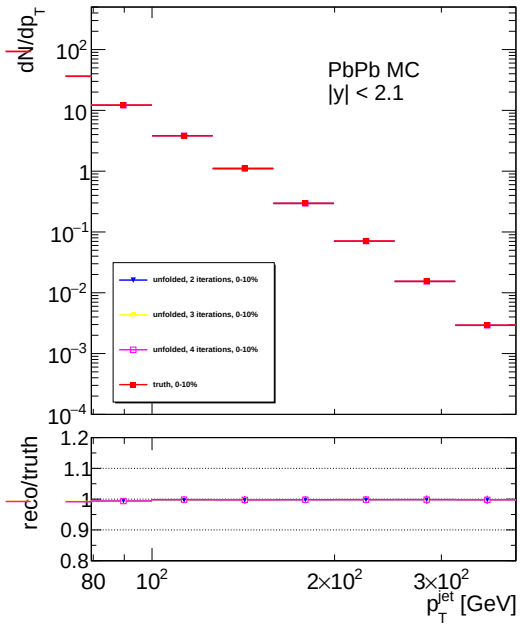

Figure 4.14: Jet spectra for central 0–10% Pb+Pb collisions in MC. Upper panel: Unfolded jet spectra for different number of iteration together with the truth spectra. Lower panel: Ratio of unfolded to truth jet spectra.

with $|y| < 2.1$.

To better quantify the trends seen in the ratios, the differences between integrals of $D(p_{\mathrm{T}})$ distributions measured in heavy-ion collisions and the integrals of $D(p_{\mathrm{T}})$ distributions measured in pp collisions, N^{ch}, was evaluated,

$$N^{\mathrm{ch}} \equiv \int_{p_{\mathrm{T,min}}}^{p_{\mathrm{T,max}}} \left(D(p_{\mathrm{T}})|_{\mathrm{cent}} - D(p_{\mathrm{T}})|_{\mathrm{pp}} \right) \mathrm{d}p_{\mathrm{T}}. \tag{4.14}$$

Here 'cent' represents one of seven centrality bins. Three ranges defined by values of $p_{\mathrm{T,min}}$ and $p_{\mathrm{T,max}}$ were chosen to match the observations in $R_{D(p_{\mathrm{T}})}$, namely $1-4$ GeV, $4-25$ GeV, and $25-100$ GeV. Thus three values of N^{ch} were obtained for each centrality bin which represent the number of particles carrying: (1) the excess seen in heavy-ion collisions for particles with $1 < p_{\mathrm{T}} < 4$ GeV, (2) a depletion seen for particles with $4 < p_{\mathrm{T}} < 25$ GeV, and (3) the enhancement seen for particles with $25 < p_{\mathrm{T}} < 100$ GeV. Further, the difference in integrals of the first moment of the $D(p_{\mathrm{T}})$ distributions, $P_{\mathrm{T}}^{\mathrm{ch}}$, were also evaluated,

$$P_{\mathrm{T}}^{\mathrm{ch}} \equiv \int_{p_{\mathrm{T,min}}}^{p_{\mathrm{T,max}}} \left(D(p_{\mathrm{T}})|_{\mathrm{cent}} - D(p_{\mathrm{T}})|_{\mathrm{pp}} \right) p_{\mathrm{T}} \, \mathrm{d}p_{\mathrm{T}}. \tag{4.15}$$

These differences represent the total transverse momentum of particles carrying the excess or the depletion observed in $R_{D(p_{\mathrm{T}})}$ distributions.

The result of performing this calculation is shown in Fig. 4.21 where the differences of integrals are plotted as a function of number of participants calculated using the Glauber model analysis of the $\Sigma E_{\mathrm{T}}^{\mathrm{FCal}}$ [69, 96, 64]. The relation between centrality and number of participants is shown in Tab. 4.4.

A clear, almost logarithmic, increase of yields of particles with low transverse momenta with increasing centrality is seen. In contrast, the intermediate-$p_{\mathrm{T}}^{\mathrm{ch}}$

Centrality	N_{part}
0-10%	356
10-20%	261
20-30%	186
30-40%	129
40-50%	86
50-60%	53
60-80%	23

Table 4.4: The relation between centrality and the number of participants.

Centrality	0-10%	10-20%	20-30%	30-40%	40-50%	50-60%	60-80%
$P_{\mathrm{T}}^{\mathrm{ch}}$ [GeV]	$0.9^{+0.9}_{-1.7}$	$1.0^{+0.8}_{-1.3}$	$-0.0^{+0.7}_{-1.1}$	$-0.6^{+0.8}_{-0.8}$	$-0.5^{+1.0}_{-1.2}$	$-1.4^{+1.0}_{-1.2}$	$-0.8^{+1.3}_{-1.4}$
N^{ch}	$0.7^{+0.1}_{-0.2}$	$0.9^{+0.1}_{-0.1}$	$0.7^{+0.1}_{-0.1}$	$0.5^{+0.1}_{-0.2}$	$0.4^{+0.1}_{-0.1}$	$0.2^{+0.1}_{-0.2}$	$0.0^{+0.1}_{-0.1}$

Table 4.5: The difference in the total momentum, $P_{\mathrm{T}}^{\mathrm{ch}}$, and the total change in the yield of charged particles, N^{ch}, evaluated over the full range of charged particle transverse momenta, $1 < p_{\mathrm{T}}^{\mathrm{ch}} < 100$ GeV.

region exhibits less significant modifications with varying centrality. The yield at high $p_{\mathrm{T}}^{\mathrm{ch}}$ shows a mild increase with increasing centrality, however with smaller significance. The changes in the total transverse momentum follow the trends seen in the yields. The significance of the increase of the total transverse momentum in the high-$p_{\mathrm{T}}^{\mathrm{ch}}$ region is higher than the significance of the increase of yields of charged particles seen in the same region.

The difference in the total momentum can be evaluated also over the full range of charged particle transverse momenta, $1 < p_{\mathrm{T}}^{\mathrm{ch}} < 100$ GeV. It may be expected that such $P_{\mathrm{T}}^{\mathrm{ch}}$ should be identical to zero since the same range of the $p_{\mathrm{T}}^{\mathrm{jet}}$ is used in Pb+Pb and *pp* collisions. The result of this evaluation is presented in the second row of Tab. 4.5. Indeed, the $P_{\mathrm{T}}^{\mathrm{ch}}$ evaluated over the full range of charged particle transverse momenta is consistent with zero within one standard deviation of combined statistical and systematic uncertainties. The potential residual deviations from zero can be due to the difference in the shape of $p_{\mathrm{T}}^{\mathrm{jet}}$ spectra between *pp* and Pb+Pb collisions [12] which leads to a difference in the mean $p_{\mathrm{T}}^{\mathrm{jet}}$ between Pb+Pb and *pp*.

The total change in the yield of charged particles can also be evaluated by integrating the $D(p_{\mathrm{T}})$ distributions over the full range of charged particle transverse momenta. In this case we do not expect to see the same yields of charged particles in Pb+Pb and *pp* collisions since this quantity may change as a result of the jet quenching. The resulting N^{ch} is summarized in the third row of Tab. 4.5.

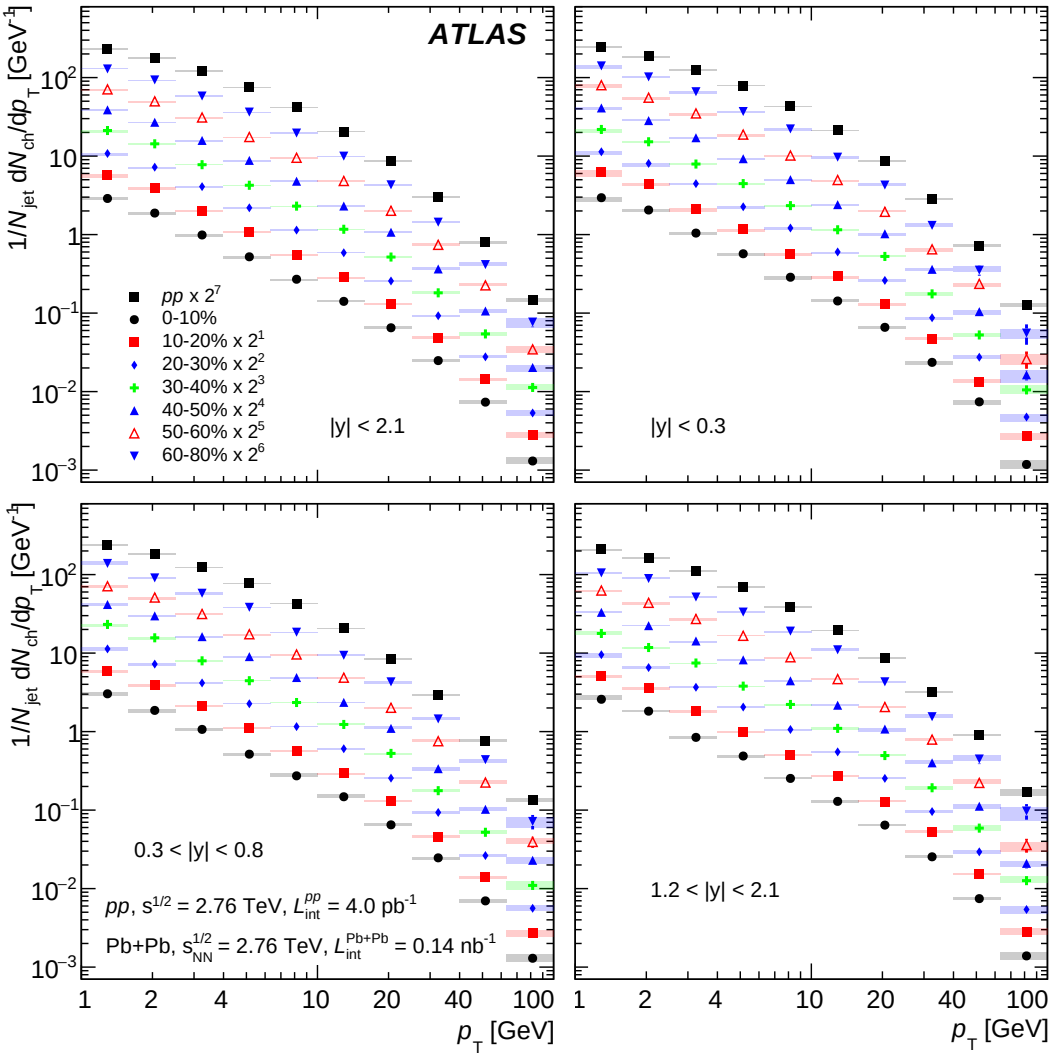

Figure 4.15: Unfolded charged particle transverse momentum distributions, $D(p_{\mathrm{T}})$, measured in pp collisions and for seven centrality bins measured in Pb+Pb collisions. Four panels show $D(p_{\mathrm{T}})$ distributions with different selection on jet rapidity for jets with p_{T} in the interval of $100 - 398$ GeV. The error bars on the data points indicate statistical uncertainties while the shaded bands indicate systematic uncertainties.

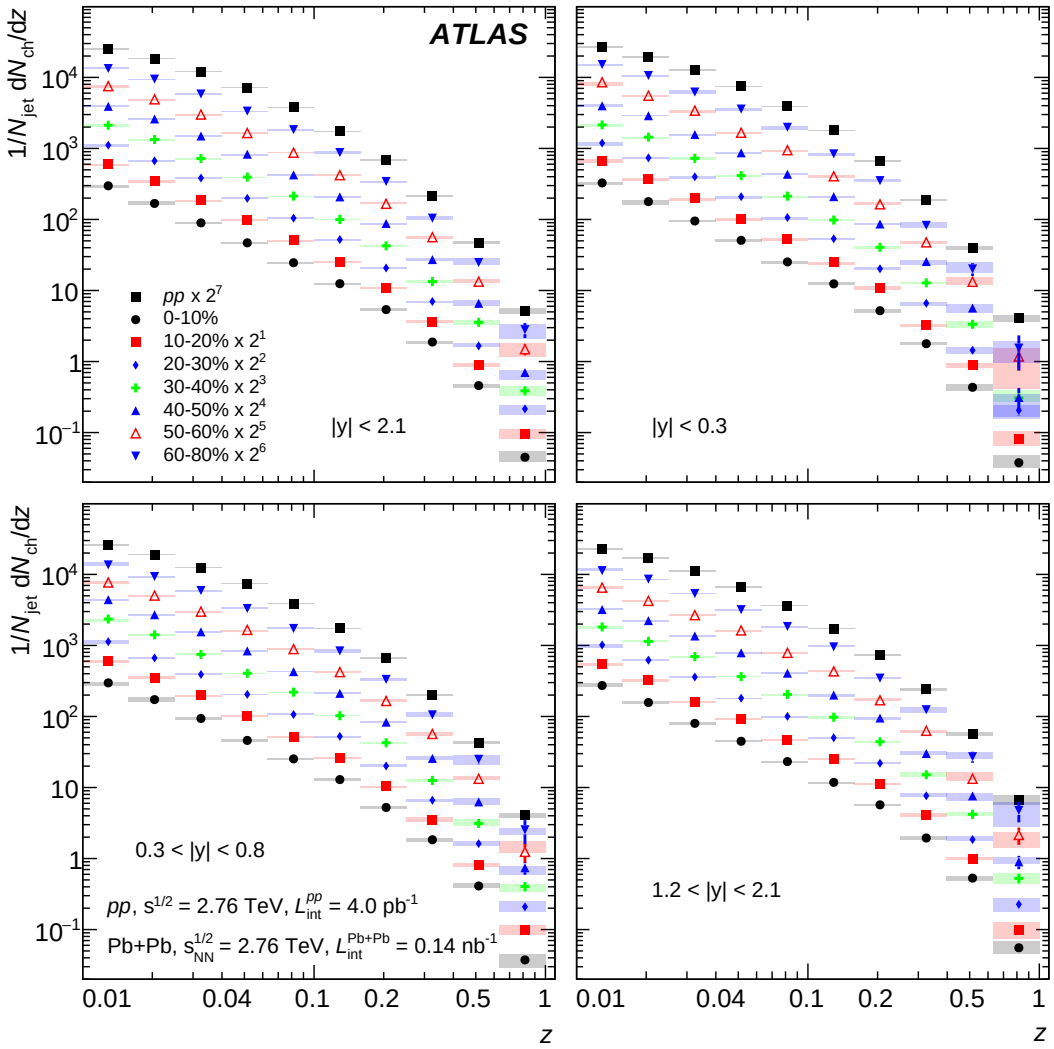

Figure 4.16: Unfolded distributions of longitudinal momentum fraction, $D(z)$, measured in pp collisions and for seven centrality bins measured in Pb+Pb collisions. Four panels show $D(z)$ distributions with different selection on jet rapidity for jets with p_{T} in the interval of $100 - 398$ GeV. The error bars on the data points indicate statistical uncertainties while the shaded bands indicate systematic uncertainties.

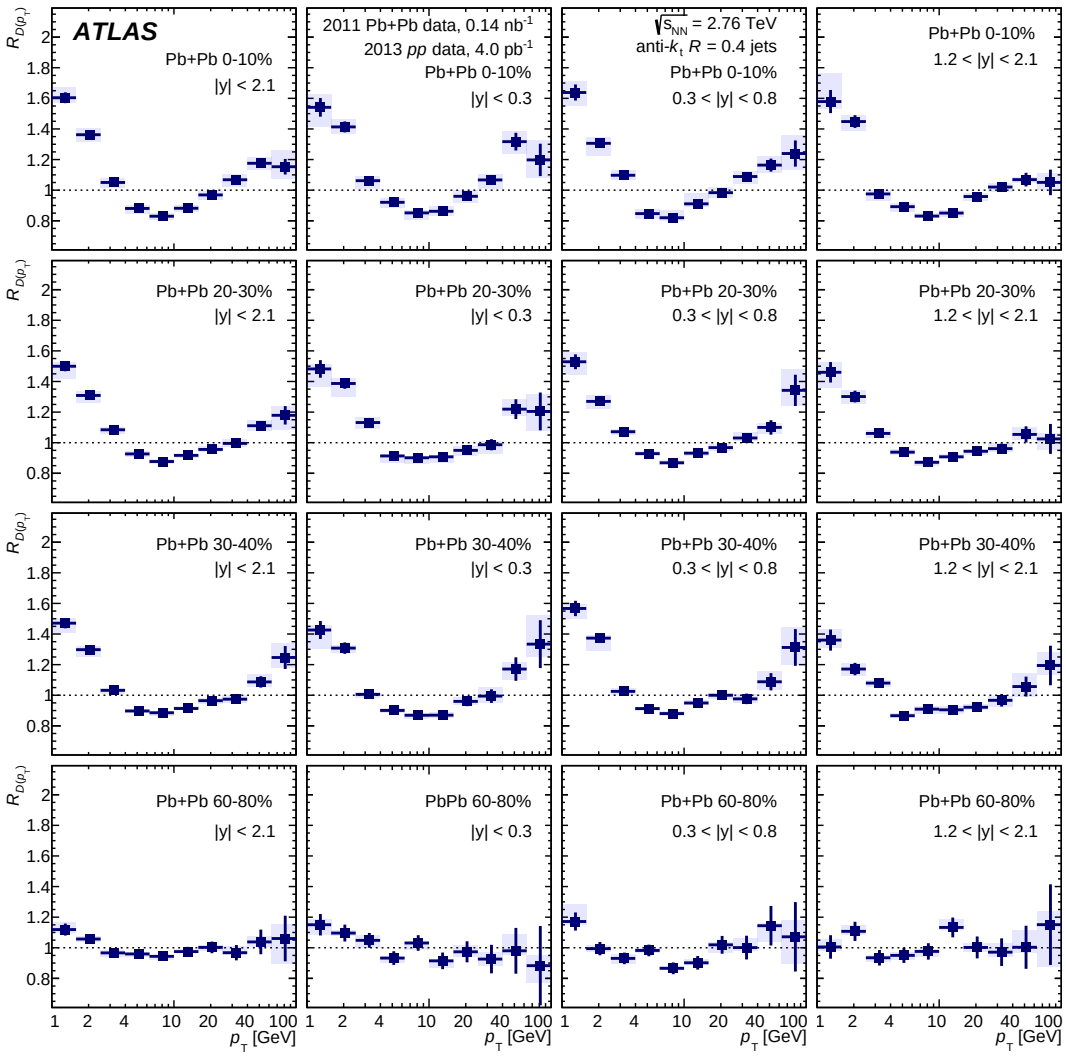

Figure 4.17: The ratio of unfolded $D(p_{\mathrm{T}})$ distributions measured in heavy-ion collisions to unfolded $D(p_{\mathrm{T}})$ distributions measured in pp collisions, $R_{D(p_{\mathrm{T}})}$. $R_{D(p_{\mathrm{T}})}$ distributions are evaluated in four different centrality bins (rows) and four different selections on jet rapidity of jets with $100 < p_{\mathrm{T}} < 398$ GeV (columns). The error bars on the data points indicate statistical uncertainties while the shaded bands indicate systematic uncertainties.

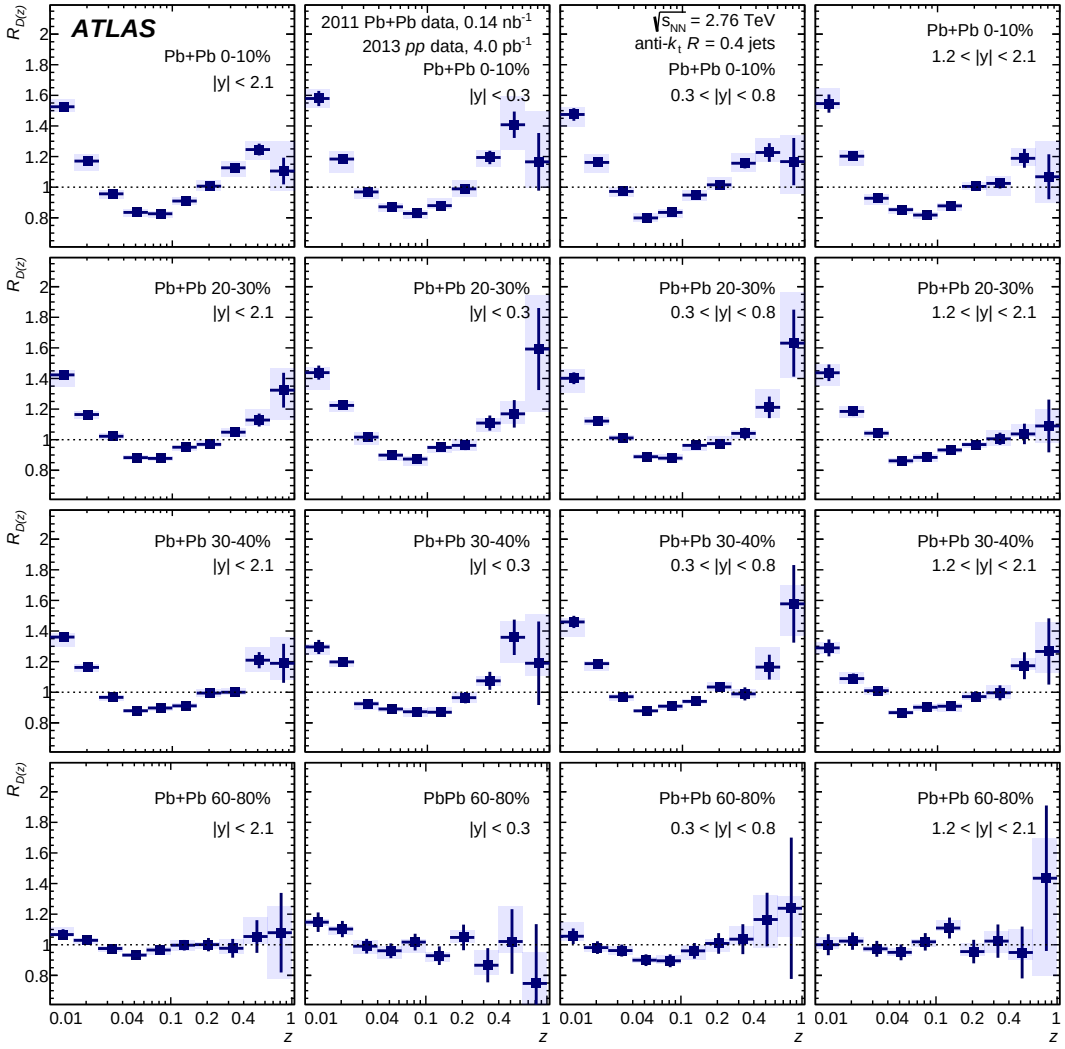

Figure 4.18: The ratio of unfolded $D(z)$ distributions measured in heavy-ion collisions to unfolded $D(z)$ distributions measured in pp collisions, $R_{D(z)}$. $R_{D(z)}$ distributions are evaluated in four different centrality bins (rows) and four different selections on jet rapidity of jets with $100 < p_{\mathrm{T}} < 398$ GeV (columns). The error bars on the data points indicate statistical uncertainties while the shaded bands indicate systematic uncertainties.

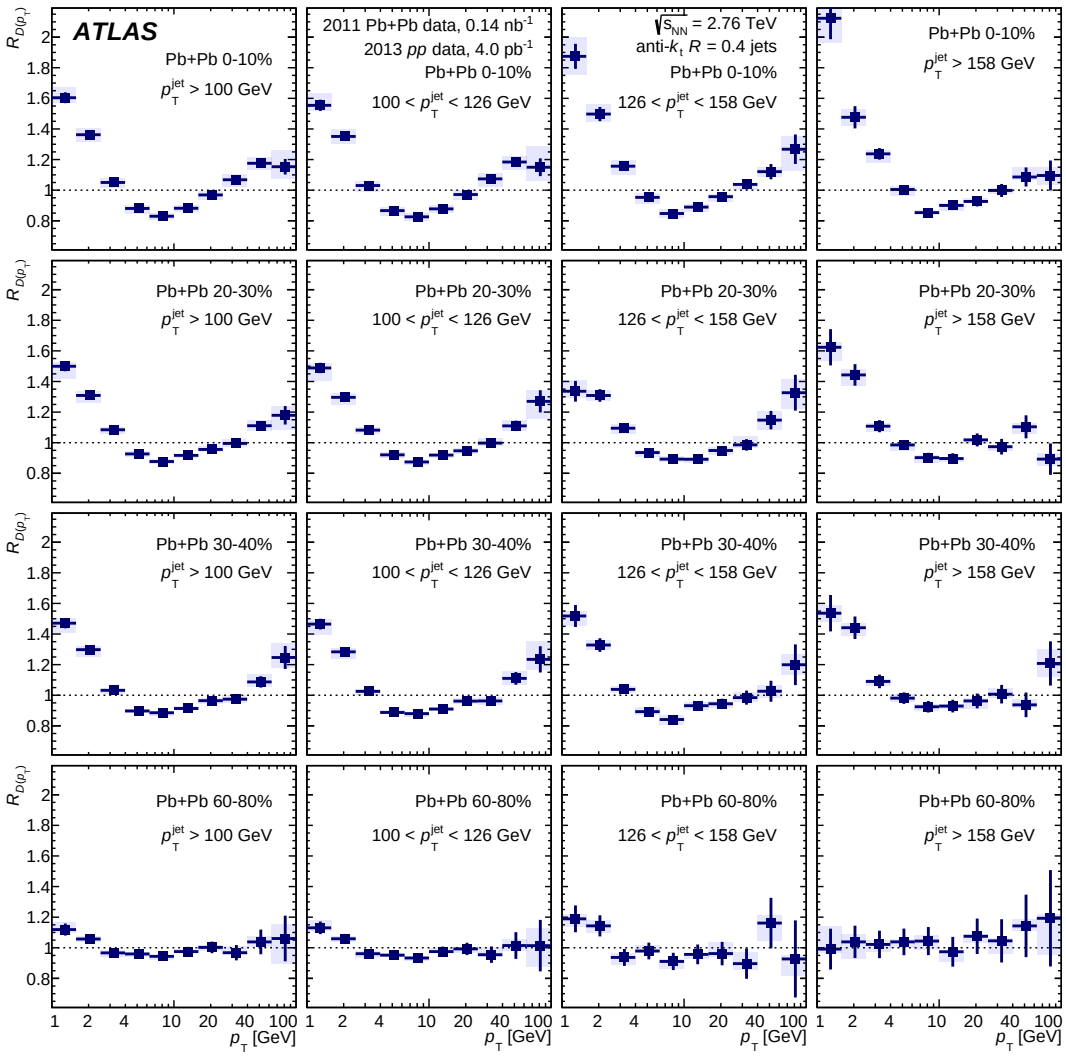

Figure 4.19: The ratio of unfolded $D(p_{\mathrm{T}})$ distributions measured in heavy-ion collisions to unfolded $D(p_{\mathrm{T}})$ distributions measured in pp collisions, $R_{D(p_{\mathrm{T}})}$. $R_{D(p_{\mathrm{T}})}$ distributions are evaluated in four different centrality bins (rows) and four different selections on jet p_{T} of jets with $|y| < 2.1$ (columns). The error bars on the data points indicate statistical uncertainties while the shaded bands indicate systematic uncertainties.

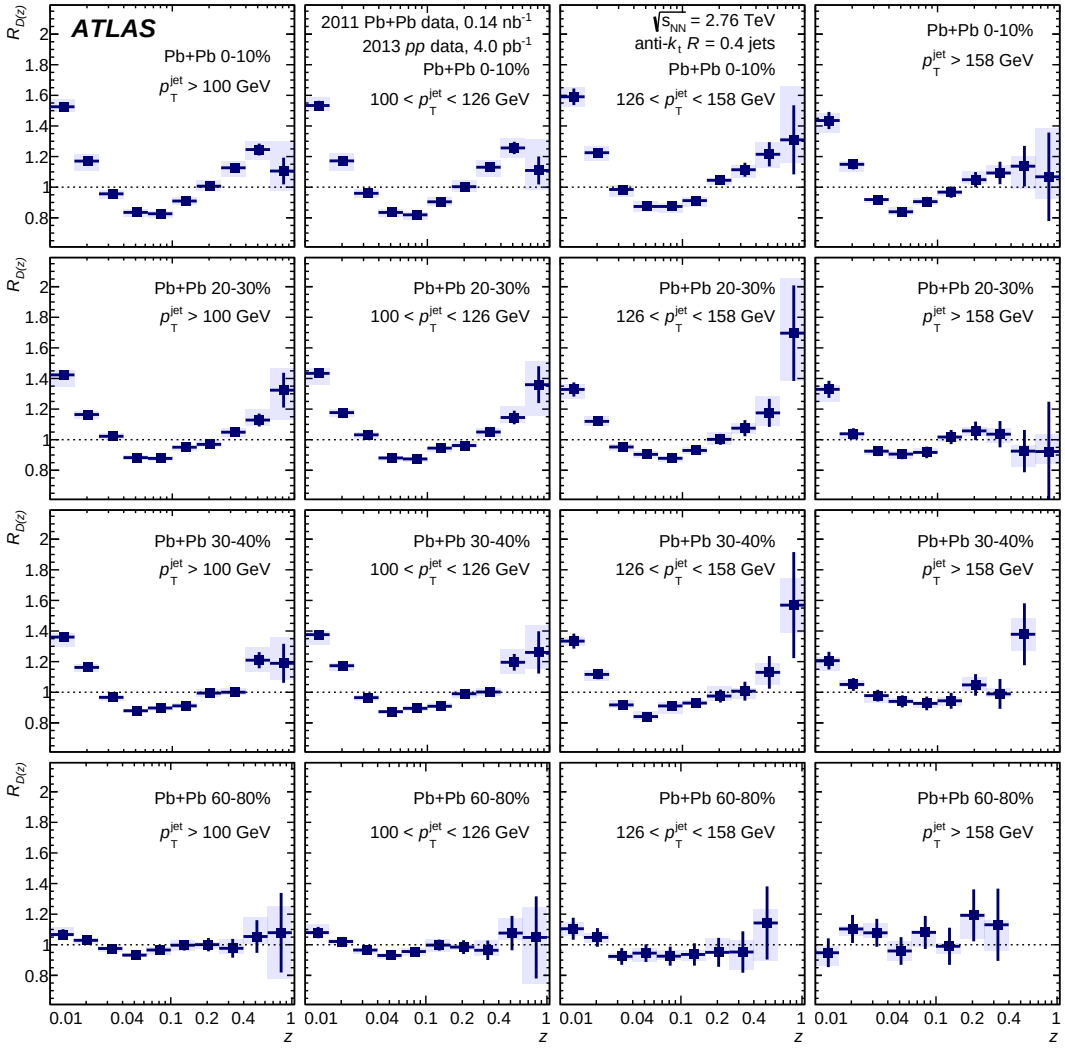

Figure 4.20: The ratio of unfolded $D(z)$ distributions measured in heavy-ion collisions to unfolded $D(z)$ distributions measured in pp collisions, $R_{D(z)}$. $R_{D(z)}$ distributions are evaluated in four different centrality bins (rows) and four different selections on jet p_{T} of jets with $|y| < 2.1$ (columns). The error bars on the data points indicate statistical uncertainties while the shaded bands indicate systematic uncertainties.

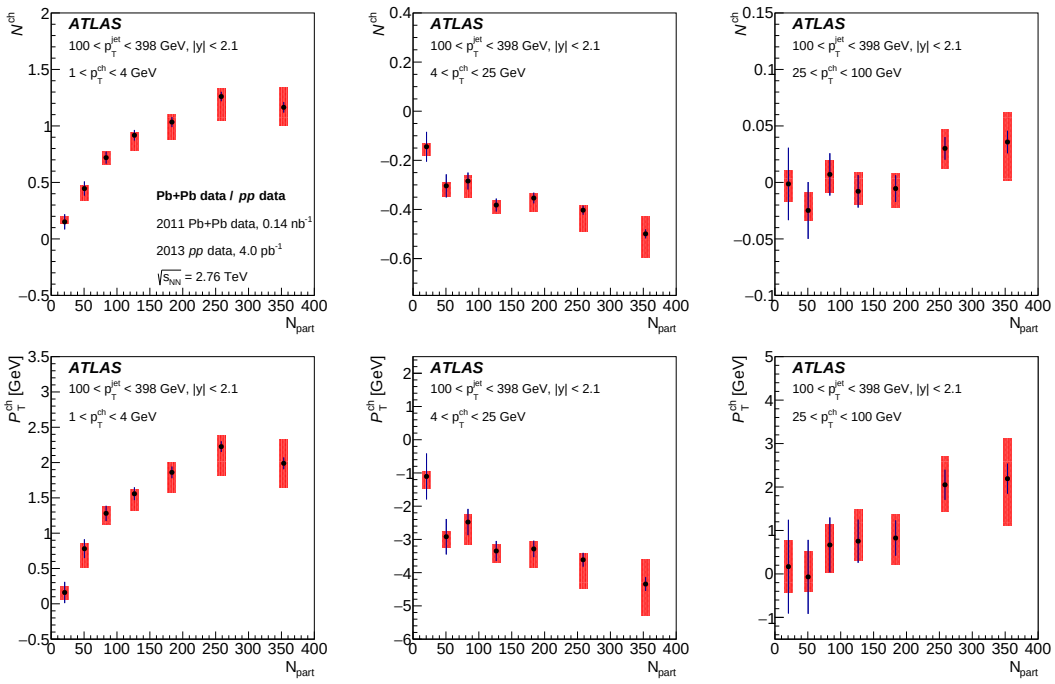

Figure 4.21: Upper panels: difference in the total yield of particles in a given $p_{\mathrm{T}}^{\mathrm{ch}}$ interval (indicated in the legend) measured in Pb+Pb and the total yield of particles in the same $p_{\mathrm{T}}^{\mathrm{ch}}$ interval measured in pp collisions, N^{ch}. Lower panels: difference in the total transverse momentum of particles in a given $p_{\mathrm{T}}^{\mathrm{ch}}$ interval measured in Pb+Pb and the total transverse momentum of particles measured in pp, $P_{\mathrm{T}}^{\mathrm{ch}}$. The differences are evaluated as a function of number of participating nucleons. The error bars on the data points indicate statistical uncertainties while the shaded bands indicate systematic uncertainties.

5. Measurement of inclusive jet suppression

In this chapter we describe the new measurement of the jet yields and jet nuclear modification factor. The main goal of this analysis is to reproduce and extend the previously published measurement of nuclear modification factor of jets [12] in the new center-of-mass energy.

Measurements of the modification of jet observables as a function of collision centrality can provide insight into the mechanism of the jet quenching. Generally, the energy loss of partons traversing QGP will result in a systematic reduction in the jet yield at fixed jet p_{T}[1]. Thus, the hard scattering rates are suppressed in central collisions relative to peripheral or pp collisions as measured previously [11, 12]. This can be quantified by the nuclear modification factor, R_{AA}, introduced in Sec. 1.7.

An R_{AA} of ≈ 0.5 in 0-10% central collisions was reported in Pb+Pb measurements at $\sqrt{s_{\mathrm{NN}}} = 2.76$ TeV [12]. This result indicates a suppression of jet yields by roughly a factor of two in central collisions with respect to pp collisions at the same center-of-mass energy. Furthermore, that study showed several interesting features:

- R_{AA} was observed to increase only very slowly with increasing jet p_{T}
- R_{AA} exhibited no significant rapidity dependence
- significant suppression ($R_{\mathrm{AA}} \approx 0.8$) was measured in 60-80% peripheral collisions.

More information can be found in Ref. [12] and a brief summary is also provided in Sec. 6.2. The new study addresses the stability of above mentioned features with respect to changing the center of mass energy. It also provides a precision measurement of the R_{AA} at high-p_{T} which should help to constrain models of the jet quenching.

This chapter is organized as follows: Sec. 5.1 describes data samples used for the analysis together with the event selection. Sec. 5.2 summarizes the actual analysis and unfolding procedure. Sec. 5.3 describes the systematic uncertainties and Sec. 5.4 presents the results of the measurement. Jet reconstruction in heavy-ion collision for jet R_{AA} measurement is previously describes in Sec. 3.2.

Analysis presented in this chapter was published in Ref. [15].

[1] In this chapter we use symbol p_{T} for jet p_{T} instead of the charged particle momentum as used in the jet fragmentation measurement in the previous chapter.

5.1 Data samples and event selection

5.1.1 Collision data, trigger and event selection

The collision data used in this analysis was recorded in the LHC run 2 during fall 2015. The run consisted of 25.4 pb^{-1} pp collisions at $\sqrt{s}$ = 5.02 TeV and 0.52 nb^{-1} Pb+Pb collisions at the same center-of-mass energy.

This analysis used the data from the Hard Probes (HP) stream. The HP stream consists of different High Level Triggers (HLT) triggering on high-p_{T} jets, muons, electrons, and photons. The HLT jet candidate events are first identified at L1. These L1 "seeds" are passed to the HLT where the jet trigger algorithm is used for the final selection. In pp collisions jets were triggered using jets built from topoclusters and no underlying event subtraction was performed. In Pb+Pb collisions jets were triggered using jets built from towers and the heavy-ion UE subtraction was performed. The final trigger jets were calibrated to the hadronic level. The efficiency of all jet triggers in use are shown in Fig. 5.1 for both, pp and Pb+Pb collisions. More plots on the trigger performance are included in Figs. B.1-B.3 in Appendix B.

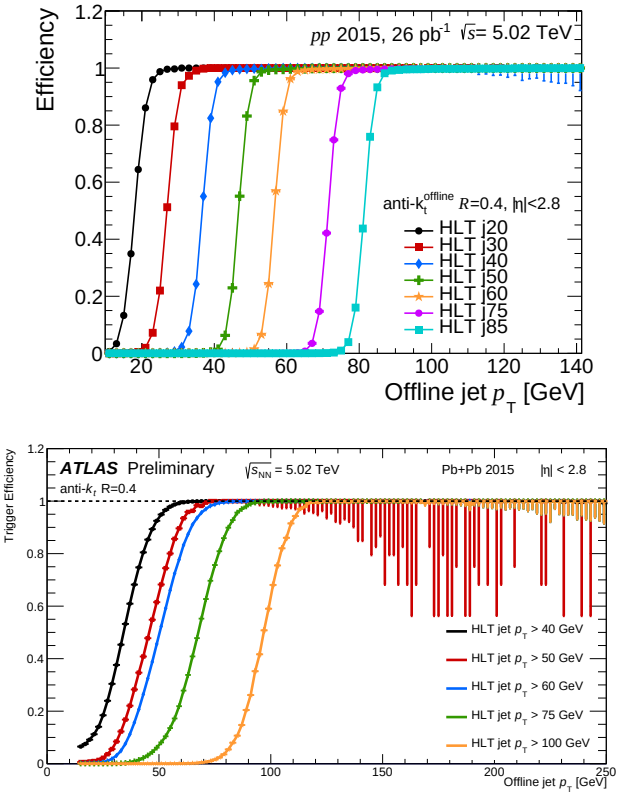

Figure 5.1: Left: trigger efficiencies for $R = 0.4$ offline jets for pp HLT jet triggers in pp collisions at 5.02 TeV. Right: trigger efficiencies for $R = 0.4$ offline jets for Pb+Pb HLT jets in Pb+Pb collisions at 5.02 TeV.

Jets that are entering this analysis are selected from jet triggers in the region of jet p_{T} for which the triggers are fully efficient (i.e. the efficiency is greater than 99.9%). The list of offline reconstructed jet p_{T} intervals with triggers that are used in those intervals is summarized in Table 5.1 for pp collisions and in

trigger	$p_{\mathrm{T}}^{\mathrm{jet}}$ (GeV)
HLT_j30_L1TE5	$34.1 - 44.5$
HLT_j40_L1TE10	$44.5 - 59.0$
HLT_j50_L1J12	$59.0 - 70.0$
HLT_j60_L1J15	$70.0 - 79.0$
HLT_j75_L1J20	$79.0 - 89.0$
HLT_j85	> 89.0

Table 5.1: Triggers used in the analysis of 2015 *pp* data and the corresponding $p_{\mathrm{T}}^{\mathrm{jet}}$ ranges.

trigger	$p_{\mathrm{T}}^{\mathrm{jet}}$ (GeV)
HLT_j50_ion_L1TE20	$68.1 - 79.4$
HLT_j60_ion_L1TE50	$79.4 - 89.1$
HLT_j75_ion_L1TE50	> 89.1

Table 5.2: Triggers used in the analysis of 2015 Pb+Pb data and the corresponding $p_{\mathrm{T}}^{\mathrm{jet}}$ ranges.

Table 5.2 for Pb+Pb collisions. The number of jets was corrected by prescale factors obtained from ATLAS tool for the luminosity calculating, `Lumicalc`.

The jet cross section as a function of run number (red line) and the luminosity recorded by each run (blue line) is shown in Fig. 5.2 for Pb+Pb and *pp* events. The cross section should be constant as a function of run number. The inconsistencies here indicate that a small fraction of the Pb+Pb data (less than 1%) was not analysed which is due to broken datasets.

5.1.2 Monte-Carlo sample

Three MC datasets are used in this study. The first one is MC15 POWHEG + PYHTHIA8 dijet sample at $\sqrt{s} = 5.02$ TeV. Second one consists of the same signal dijet events as those used in the first sample but embedded into the minimum bias heavy-ion collisions. The minimum bias heavy ion data were collected for this overlay MC during the 2015 run. The events were recorded by a dedicated minimum bias trigger. The signal from this trigger was combined with the signal from POWHEG+PYHTHIA8 at the digitization stage, and then reconstructed as a combined event. All samples use the A14 ATLAS tune and the NNPDF23LO pdfs [97].

5.1.3 Jet *pp* Cleaning

The *pp* jets were cleaned using the standard cleaning tool defined by ATLAS JetEtMiss group to remove the background in the events due to non-collision backgrounds and noise. The cut level was set to "BadLoose" which is recommended by JetEtMiss group. More information on the cleaning can be found in Ref. [93].

The efficiency for this cleaning was evaluated using the tag and probe method. The tag and probe method utilizes symmetric dijets pair within $\Delta\Phi > 3.0$ and

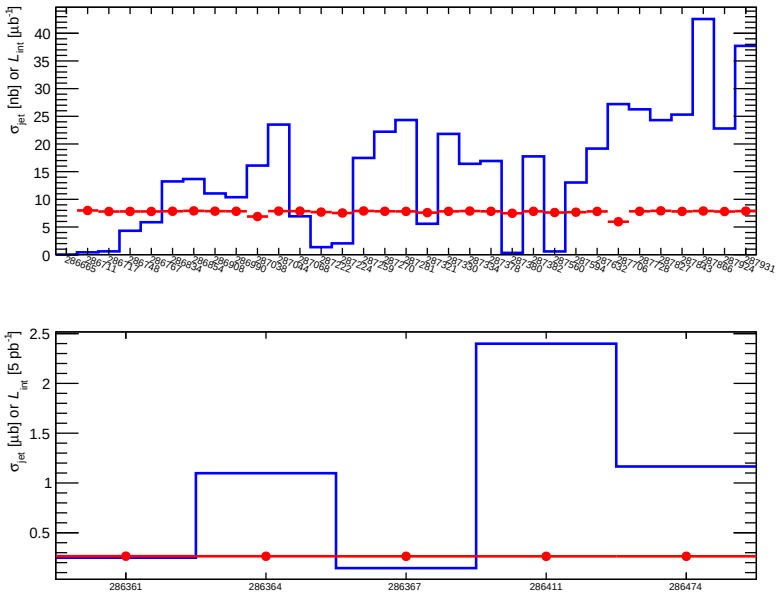

Figure 5.2: The jet cross section (red line) and the recorded luminosity (blue line) as a function of run number for the Pb+Pb data (upper panel) and for pp data (lower panel).

$A_J = (p_{T1} - p_{T2})/(p_{T1} + p_{T2}) < 0.3$ where one jet has to pass the cleaning cut (the probe). The method keeps track of the other jet passed the cut (tag).

5.2 Data analysis

5.2.1 Raw inclusive jet yields and jet R_{AA}

The jet spectra and jet R_{AA} are measured for jets with $p_{\mathrm{T}} > 100$ GeV, in following bins of centrality: 0–10%, 10–20%, 20–30%, 30–40%, 40–50% 50–60%, 60–70%, and 70–80% and in following bins of jet rapidity: $|y| < 0.3$, $0.3 < |y| < 0.8$, $0.8 < |y| < 1.2$, $1.2 < |y| < 1.6$, $1.6 < |y| < 2.1$, $2.1 < |y| < 2.8$, $|y| < 2.8$. Subset of these selections is selected for the final presentation of the result. Table 5.3 shows the number of participants for different centrality bins. Table 5.4 shows the relation between centrality and the ratio of number of binary collisions.

Centrality range	N_{part}	N_{part} Abs Err	T_{AA} [1/mb]	T_{AA} Abs Err
70–80%	15.39	1.01	0.22	0.02
60–70%	30.59	1.55	0.56	0.04
50–60%	53.90	1.98	1.27	0.07
40–50%	86.99	2.34	2.63	0.11
30–40%	131.40	2.58	4.94	0.15
20–30%	189.19	2.78	8.63	0.17
10–20%	264.06	2.82	14.33	0.17
0–10%	358.79	2.20	23.35	0.20

Table 5.3: The relation between centrality, number of participants and between the nuclear thickness function with their uncertainties.

centrality ratio	R_{coll}	R_{coll} Abs Err
50-60% / 60-80%	3.24	0.07
40-50% / 60-80%	6.68	0.26
30-40% / 60-80%	12.54	0.65
20-30% / 60-80%	21.91	1.37
10-20% / 60-80%	36.36	2.61
0-10% / 60-80%	59.24	4.70

Table 5.4: The relation between centrality and the ratio of number of binary collisions with their uncertainties.

The $\eta - \phi$ distributions for jets with p_{T} greater than 100 GeV are shown in Figure 5.3 for *pp* and Pb+Pb collisions (with the most central and peripheral centrality bin shown). Figure 5.4 overlays the rapidity distribution for *pp* and various centrality bins in Pb+Pb. The spectrum is smooth except for some irregularities that are indicative of regions of transition in the ATLAS calorimeter and holes that are corrected for in the analysis. The rapidity bins used in this analysis were chosen to follow these irregularities such that the response does not change dramatically within a given rapidity bin. They also follow the selection used for the first jet R_{AA} result published in Ref. [12]. The hole is removed by taking out jets in the region $0 < y < 1$ and $\pi/4 < \phi < 11\pi/32$ and then scaling the remaining jets in that rapidity region by the amount removed in ϕ: $(2\pi/(2\pi - 3\pi/32)$. This is done in both the data and for matched reconstructed jets in the MC in Pb+Pb and *pp* collisions.

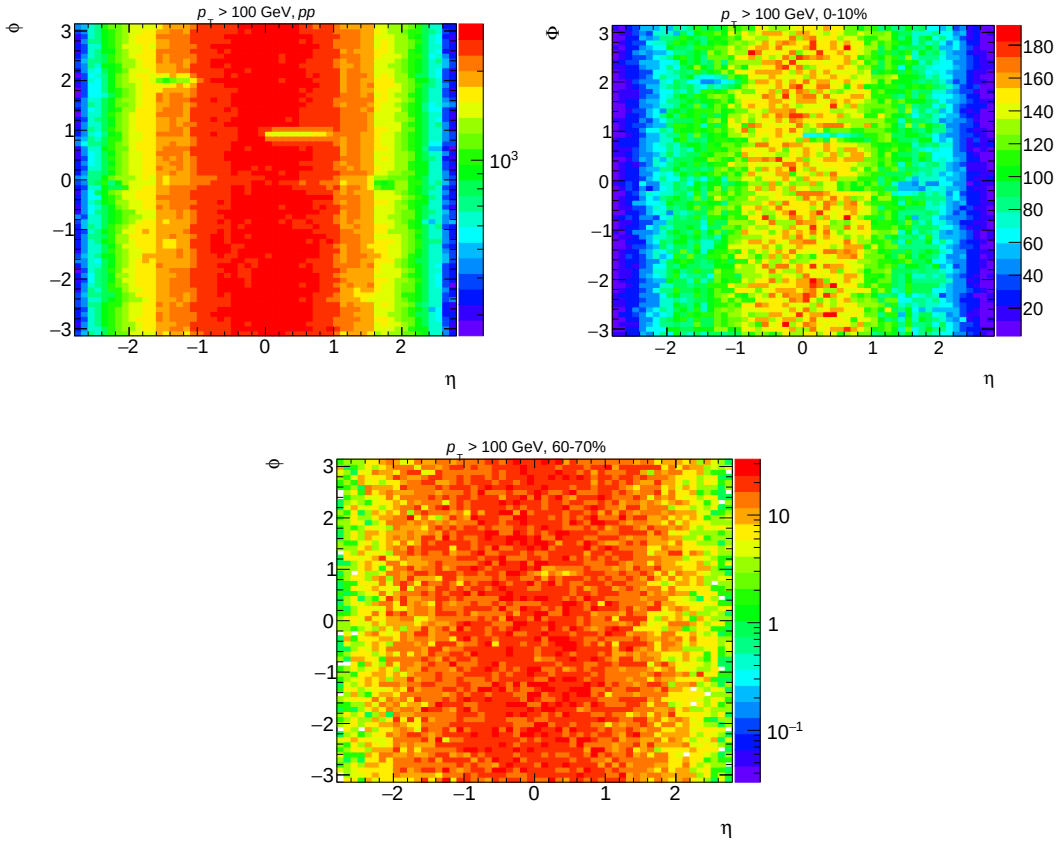

Figure 5.3: The $\eta - \phi$ distribution for $R = 0.4$ jets with jet $p_{\mathrm{T}} > 100$ GeV and $|y| < 2.8$ in pp data (upper left), Pb+Pb data in 0–10% (upper right), and Pb+Pb data in 60–70% (lower).

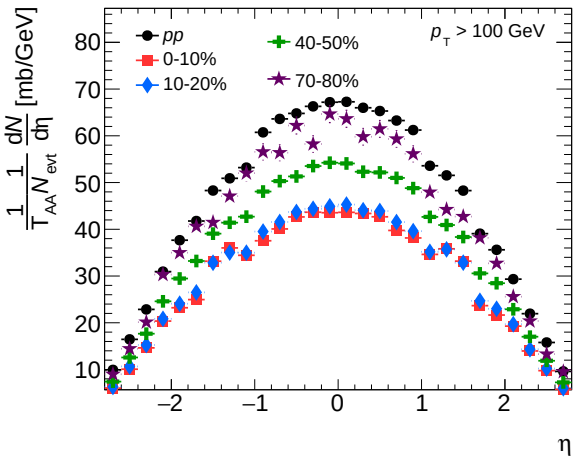

Figure 5.4: The pseudorapidity distribution for $R = 0.4$ jets with $p_{\mathrm{T}} > 100$ GeV in pp data (teal) and Pb+Pb in 0–10% (black), 20–30% (red), 40–50% (blue) and 60–70% (green).

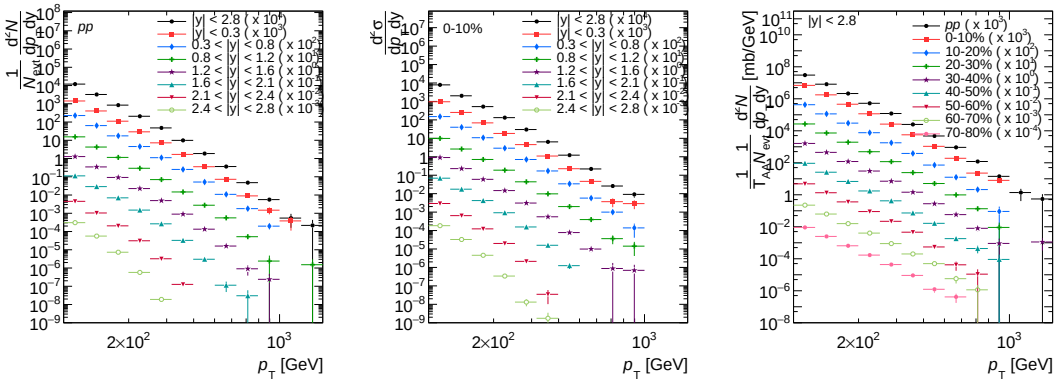

Figure 5.5: The raw jet p_{T} distribution for $R = 0.4$ jets with $p_{\mathrm{T}} > 100$ GeV in $|y| < 0.3$ (black), $0.3 < |y| < 0.8$ (red), $0.8 < |y| < 1.2$ (blue), $1.2 < |y| < 1.6$ (green), $1.6 < |y| < 2.1$ (purple), $2.1 < |y| < 2.4$ (teal), and $2.4 < |y| < 2.8$ (maroon) for pp on the left and Pb+Pb 0–10% in the middle. The jet p_{T} distribution for $|y| < 2.8$ for pp (pink) and Pb+Pb 0–10% (black), 10–20% (red), 20–30% (blue), 30–40% (green), 40–50% (purple), 50–60% (teal), 60–70% (maroon), and 70–80% (light green) on the right.

The jet p_{T} distributions before unfolding are shown in Figure 5.5 for bins in rapidity and centrality for Pb+Pb and pp collisions. The distributions in bins of centrality overlaid with pp in the full rapidity range are also shown. A clear and expected rapidity dependence is shown where the distributions are steeper in the more forward rapidity bins which is expected.

The data is compared to the MC before unfolding. Before the Pb+Pb MC can be compared to the data it has to be re-weighted by the $\Sigma E_{\mathrm{T}}^{\mathrm{FCal}}$ distribution as show in Figure 5.6 because of the L1 TE trigger thresholds in the MC overlay. The tail a high values of $\Sigma E_{\mathrm{T}}^{\mathrm{FCal}}$ is due to pile-up so a cut is made at $\Sigma E_{\mathrm{T}}^{\mathrm{FCal}} = 4.9$ TeV to remove pile-up in the data and MC. Since the centrality bin starting at 0.1% has $\Sigma E_{\mathrm{T}}^{\mathrm{FCal}}$ of 4.54 TeV the most trivial estimate tells that this cut removes less then 1% of real events in 0–10% centrality bin. Exponential and polynomial extrapolations of $\Sigma E_{\mathrm{T}}^{\mathrm{FCal}}$ values say that there are no real events with $\Sigma E_{\mathrm{T}}^{\mathrm{FCal}} > 4.9$ TeV in the collected data sample of a given statistics. The upper estimate of the pile-up contribution in the region of $\Sigma E_{\mathrm{T}}^{\mathrm{FCal}} < 4.9$ TeV can be based on extrapolating pile-up rates detected in the region of $\Sigma E_{\mathrm{T}}^{\mathrm{FCal}} > 4.9$ TeV to the region of the measurement. This estimate says that the residual pile-up contribution should be smaller than 0.1%. Thus we conclude that the cut above is sufficient for removing the pileup contribution.

Finally, the Pb+Pb MC needs to be re-weighted by the pp MC to get the correct POWHEG weights [2] so that the p_{T} distribution represents a cross-section that can be compared directly to the data. This is done by taking the ratio of the pp to Pb+Pb MC in each centrality bin. This is shown in Figure 5.7 where the left panel is the ratio in the most central collisions and the middle is the ratio in the most peripheral collisions. The right panel shows the average ratio as a function of centrality. This is applied on a jet-by-jet basis using the ratio as a

[2]POWHEG weights are missing in the Pb+Pb MC due a bug in the overlay.

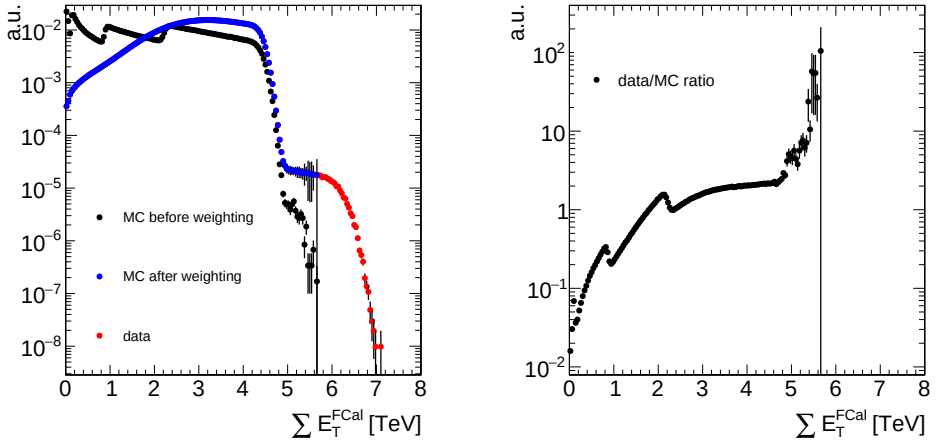

Figure 5.6: The left panel shows the event multiplicity as a function of $\Sigma E_{\mathrm{T}}^{\mathrm{FCal}}$ in MC (black) and data (red) for Pb+Pb collisions. The right panel is the ratio of the data to MC. This ratio is then applied to the MC and the result is shown in blue on the left panel.

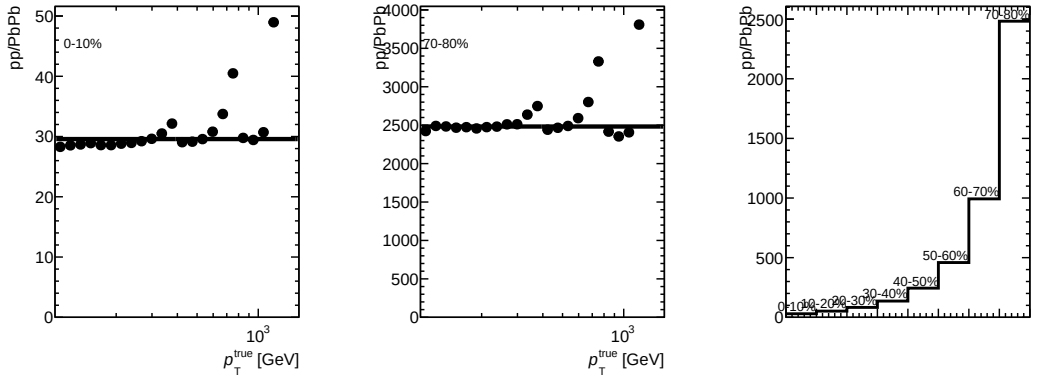

Figure 5.7: The left panel shows ratio of truth jet spectra *pp* to that in Pb+Pb MC as a function of the truth jet p_{T} in 0–10%. The middle panel shows the same thing but for 70–80%. The right panel shows the average ratio as a function of the centrality.

function of jet p_{T} to correct for the difference in shape between Pb+Pb and *pp* collisions along with the overall scale.

Fig. 5.8 shows the jet p_{T} distributions and the ratio of the data to the truth in the MC for *pp* and 0–10% centrality bin in Pb+Pb collisions as well as the overlay and the ratio of the data to the reconstructed jet p_{T} distribution in the MC for *pp* and 0–10% centrality bins in Pb+Pb collisions. These differences are a combination of resolution effects and the intrinsic difference between the MC and real data.

The raw jet R_{AA} is shown in Fig. 5.9 for different centrality selections spanning from the most central (0–10%) to the most peripheral (70–80%) and five different rapidity selections used in this analysis. This figure shows a clear suppression with centrality which is the largest in the most central collisions. Figure also indicates that the Pb+Pb raw distributions are not as steep as the *pp* distributions which

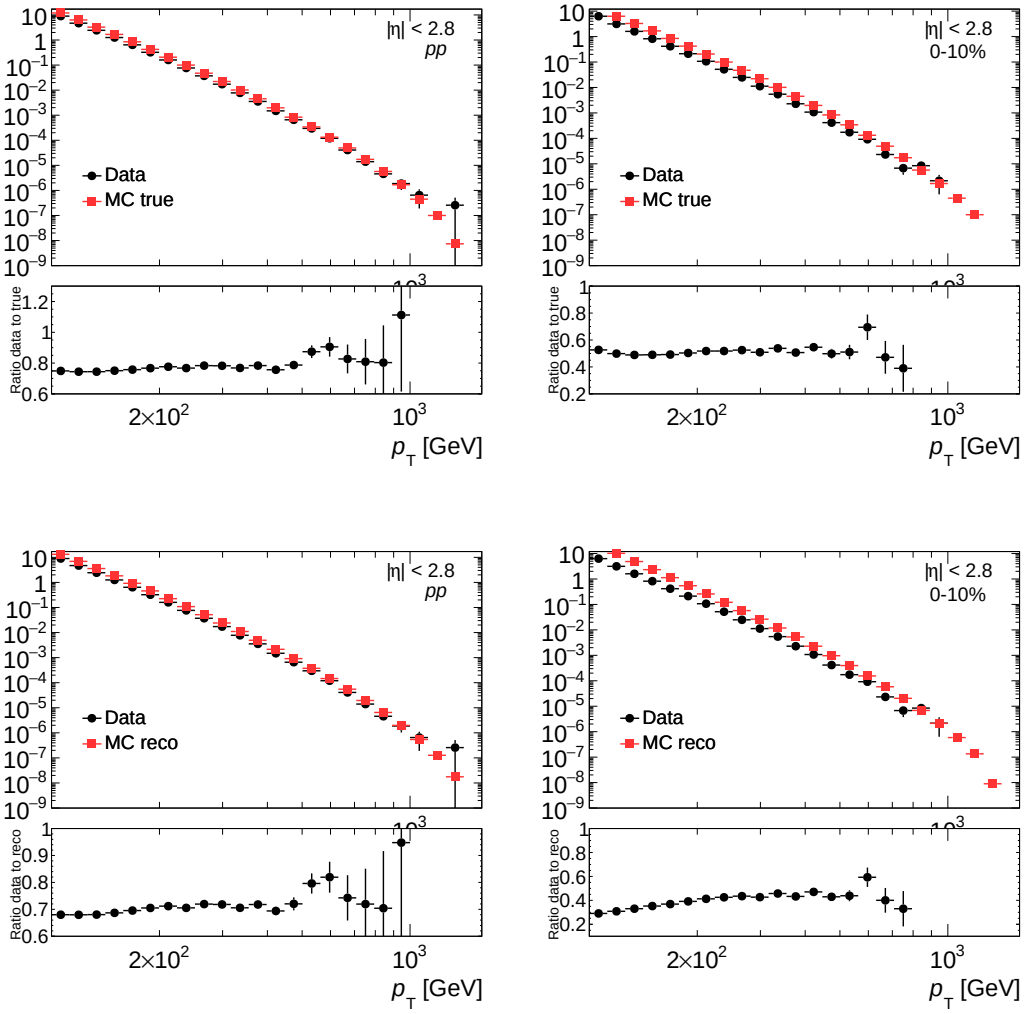

Figure 5.8: The jet p_{T} distribution for $R = 0.4$ jets with $p_{\mathrm{T}} > 100$ GeV and $|y| < 2.8$ in data (black) and MC truth (red) for pp collisions (upper left panel) and for 0–10% Pb+Pb collisions (upper right panel). The jet p_{T} distribution for $R = 0.4$ jets with $p_{\mathrm{T}} > 100$ GeV and $|y| < 2.8$ in data (black) and reconstructed MC (red) for pp collisions (lower left panel) and for 0–10% Pb+Pb collisions (lower right panel).

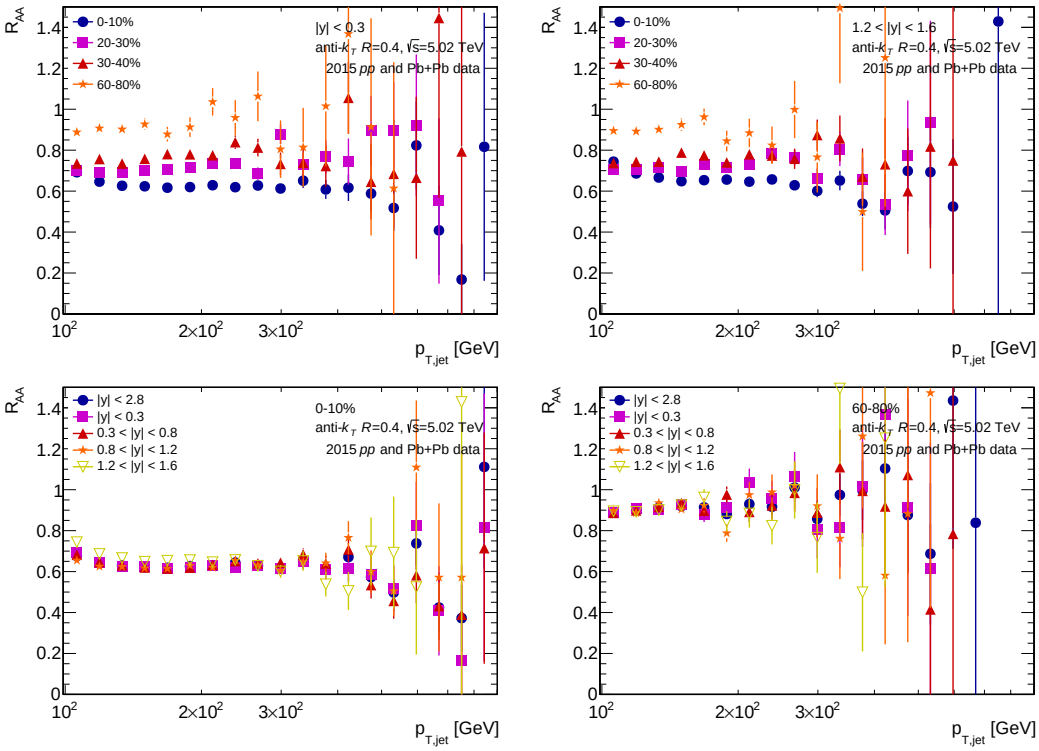

Figure 5.9: The raw jet R_{AA} for $R = 0.4$ jets with $p_{\mathrm{T}} > 100$ GeV in for $|y| < 0.3$ (upper left panel) and $1.2 < |y| < 1.6$ (upper right panel) for four centrality selections as indicated in the legend. The raw R_{AA} in 0–10% (lower left panel) and 60–80% (lower right panel) for various rapidity selections as indicated in the legend.

gives the raw R_{AA} a small jet p_{T} dependence. This trend does not change once the distributions are unfolded as shown in the next section.

5.2.2 Unfolding

The jet spectra are unfolded using the 1D Bayesian unfolding based on Bayes theorem [86] from the `RooUnfold` software package [87]. The spectra are unfolded in *pp* and in Pb+Pb collisions in 8 bins of centrality used in this analysis. The results are unfolded to account for bin migration due to the finite jet energy resolution and other residual effects such as small non-closure in JES.

The response is built from truth level jets that are match to reconstructed jets in the MC. The truth level jets are selected to have $p_{\mathrm{T}} > 40$ GeV. These are then matched to reconstructed MC jets in the event $p_{\mathrm{T}} > 80$ GeV within $\Delta R < 0.2$. The reconstructed jets in the MC receive the same reconstruction and JES/JER level calibrations and corrections as the data. The response matrices are evaluated separately for *pp* and Pb+Pb collisions and separately for each rapidity and centrality bin. Example of response matrices is shown in Fig. 5.10 for *pp* , 0–10% and 60–80% Pb+Pb.

The responses are reweighted to better represent the data. This allows the unfolding to do less work while iterating and thus may reduce the systematic uncertainties. The reweighting is done by taking the ratio of the reconstructed data to the MC and fitting it as a function of jet p_{T} by a first order polynomial

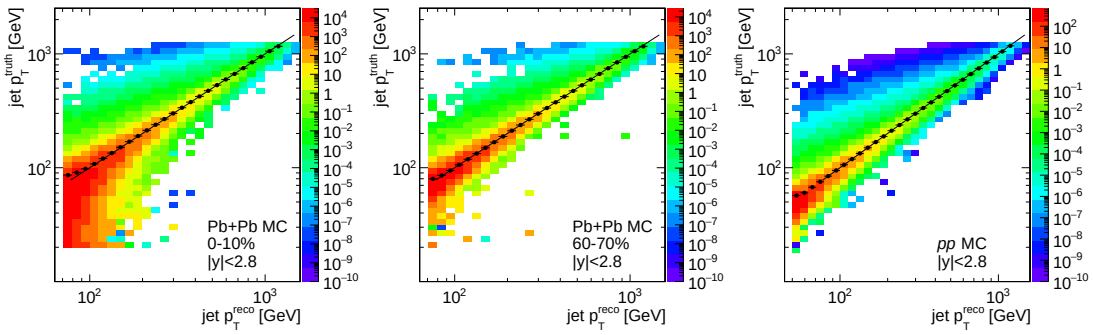

Figure 5.10: Example of response matrices for jets in $|y| < 2.8$. Left panel: Pb+Pb 0–10%, Middle panel: Pb+Pb 60–70%, Right panel: *pp*.

function as shown in Fig. 5.11. This is done in each centrality and rapidity bin in the analysis. The slope and offset are saved for each bin. These are summarized in Fig. 5.12. Then each of these weights is applied to the MC as a function of the truth jet p_{T}. This new reweighted MC is then used to unfold the data which is show in Fig. 5.13. This is the ratio of the unfolded result with the reweighting to without the reweighting for different choise of number of iterations. The result is within 2% and converges after 2-3 iterations. Choice of the number of iteration for the final unfolding was done based on the stability of the result to the number of iterations. It was found that three iterations are sufficient for all the centrality and rapidity bins both in Pb+Pb and *pp* collisions. The illustration of stability of unfolding is shown in Fig. 5.14.

The unfolding procedure is verified by evaluating the closure test in the MC which is defined as a ratio between unfolded MC distributions and MC truth distributions. This was done by splitting the MC in half and using one half to fill the response and the other half as the "data" to unfold. The "data" was unfolded using response from half the MC and this result was compared to the original truth spectrum. The closure is below 2% for all the rapidity and centrality bins in the kinematic selection except for the 60-70% centrality bin where the closure test is within 5%. considered for the analysis. The example of the closure test is shown in Fig. 5.15 for three centrality bins in heavy-ion collisions.

The unfolding procedure was further tested by performing the refolding. Refolding is multiplying the unfolded result by the response matrix and comparing this so called refolded distribution with the raw data. If the unfolding is stable no too large deviations between the raw data and refolded distributions should occur. This is indeed the case as shown in Fig. 5.16.

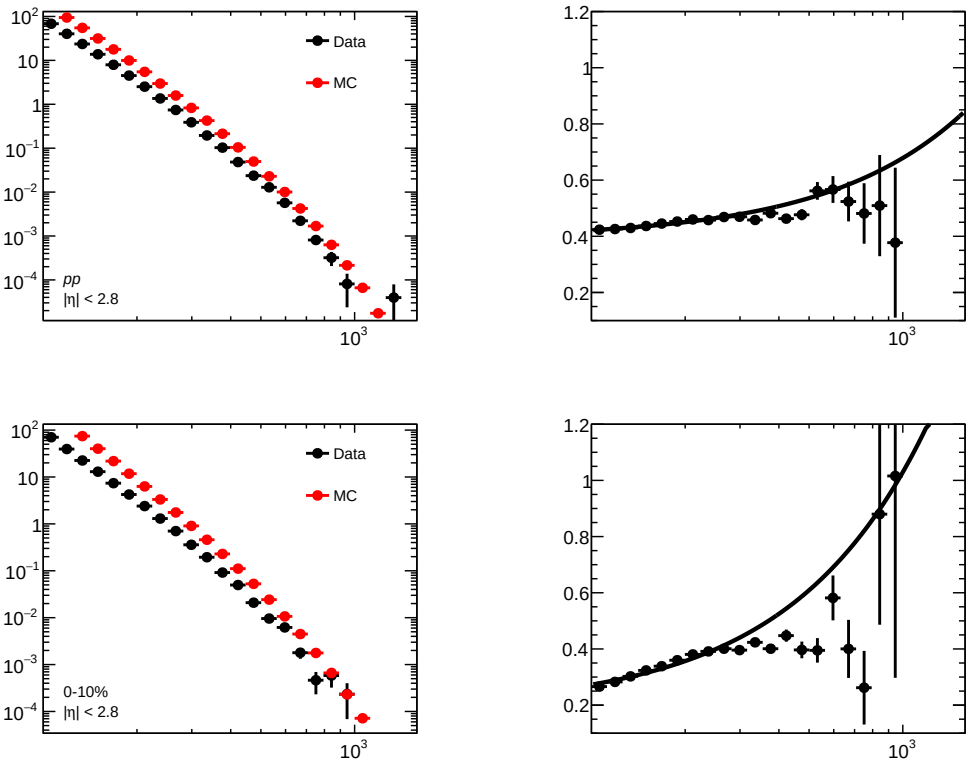

Figure 5.11: The panels on the left show jet p_{T} distributions of data and MC for pp (upper left) and 0–10% centrality bin in Pb+Pb collisions (lower left) for jets with $p_{\mathrm{T}} > 100$ GeV and $|y| < 2.8$. The panels on the right side show the ratio of data to MC together with the linear fit for pp (upper right) and 0–10% in Pb+Pb collisions (lower right).

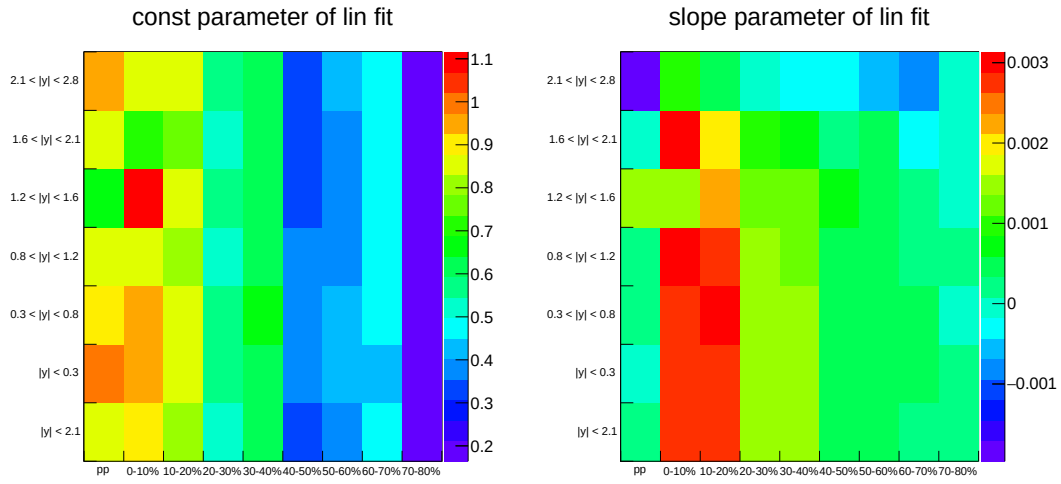

Figure 5.12: The left panel shows the values of the offset in the linear fit of the data/MC ratios in each rapidity and centrality bin in the analysis for pp and Pb+Pb collisions. The right panel is the same thing but for the slope of the linear fit.

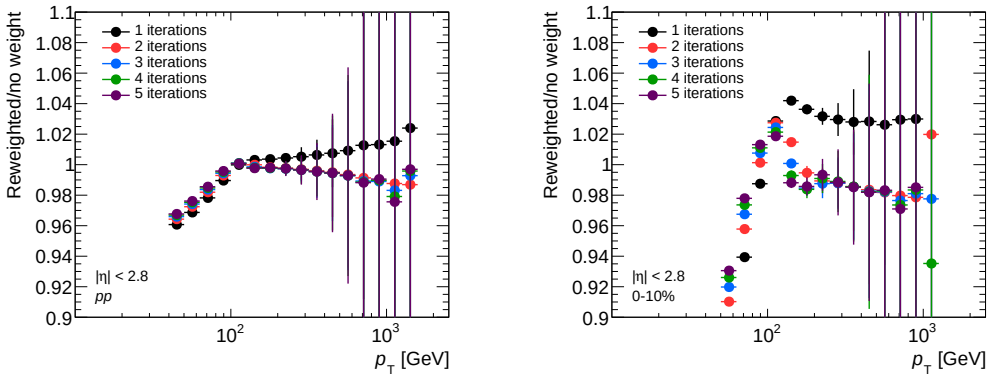

Figure 5.13: The ratio of the unfolded result with and without reweighting as a function of number of iterations for *pp* on the left and 0–10% Pb+Pb on the right.

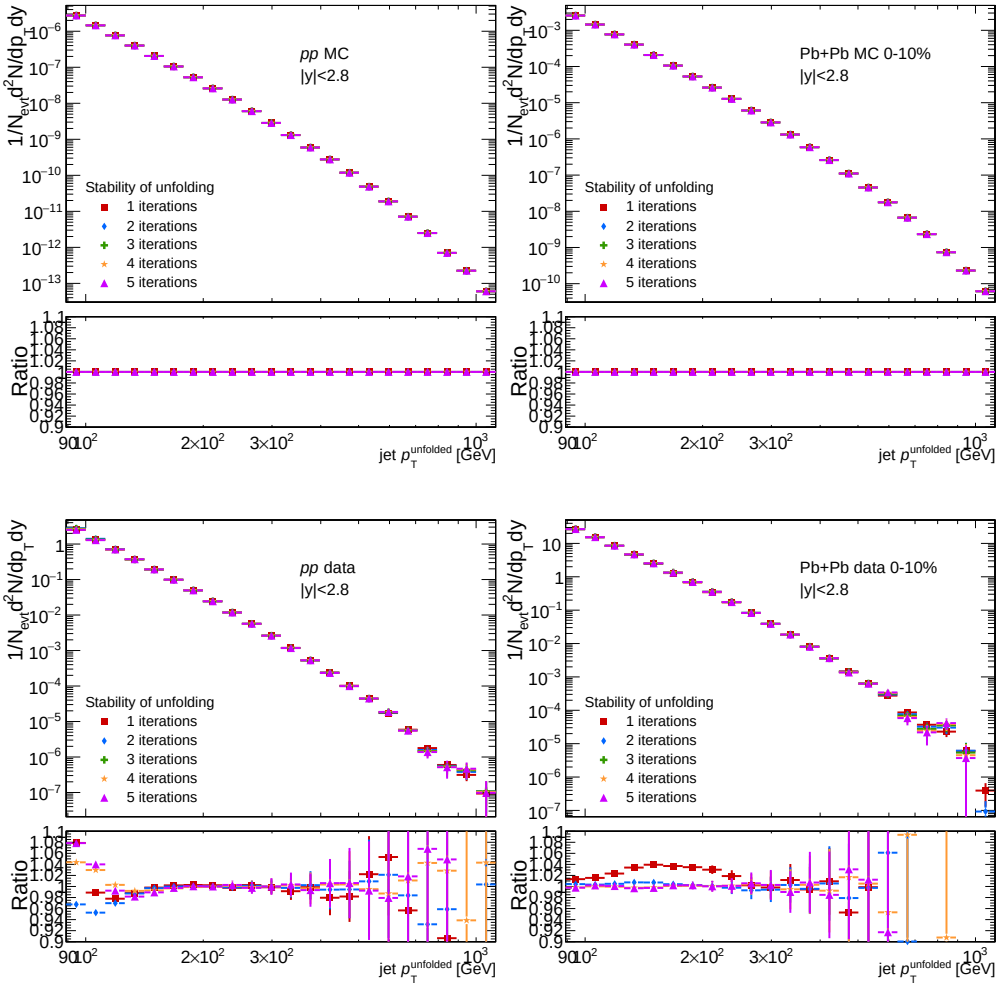

Figure 5.14: Stability of the unfolding in terms of jet spectra for different choice of number of iterations (see the legend). Ratios show spectra unfolded using a given number of iterations with respect to 3 iterations (same color/marker code as in the case of spectra) 0–10% Pb+Pb MC (upper right), *pp* MC (upper left), 0–10% Pb+Pb data (lower right), *pp* data (lower left).

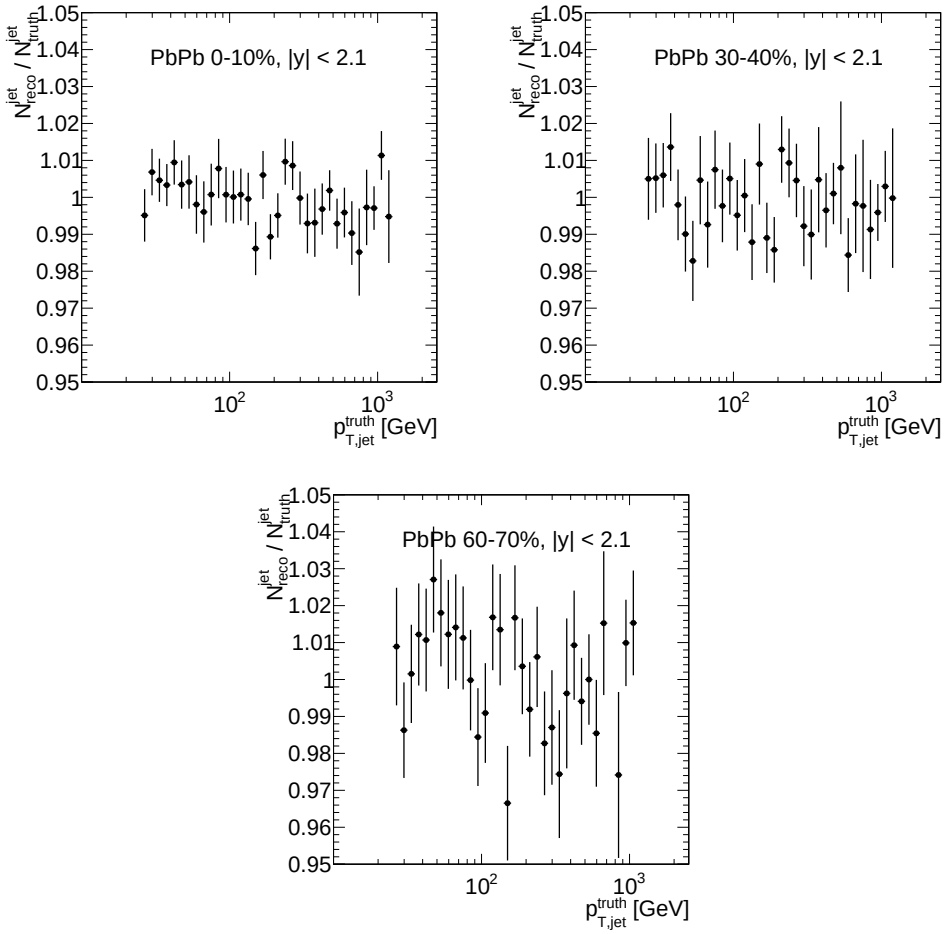

Figure 5.15: Example of the closure test (ratio of unfolded to truth distributions) in Pb+Pb MC in three different centrality intervals.

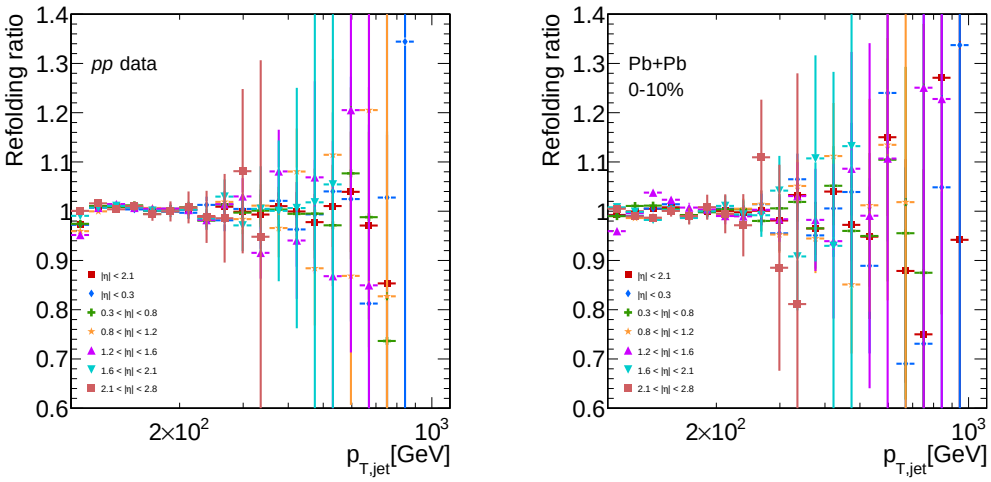

Figure 5.16: Ratio of refolded to raw distributions (refolding) for *pp* (left) and 0–10% central Pb+Pb collisions (right) both for jet with $p_{\mathrm{T}} > 100$ GeV.

5.3 Systematic uncertainties

Following sources of systematic uncertainties were identified for this analysis: jet energy scale, jet energy resolution, uncertainty due to the unfolding procedure, uncertainty on the determination of the T_{AA} factors and the uncertainty on the *pp* luminosity.

Uncertainties of the R_{AA} can be categorized into two classes. Uncertainties that are common for the numerator and denominator of R_{AA} and uncertainties that differ between the numerator and denominator of the R_{AA}. For uncertainties common to both the numerator and denominator of the R_{AA}, the uncertainties were taken as correlated. Thus, for such uncertainties corresponding uncertainty on the ratio, $r = A/B$ was taken as:

$$\pm\, \delta r|_{\mathrm{C}} \equiv \frac{A \pm \delta A}{B \pm \delta B} - \frac{A}{B}\,. \tag{5.1}$$

For uncorrelated uncertainties, the uncertainty was propagated using the usual method:

$$\delta r|_{\mathrm{U}} \equiv \frac{A}{B}\sqrt{\left(\frac{\delta A}{A}\right)^2 + \left(\frac{\delta B}{B}\right)^2}\,. \tag{5.2}$$

In general, when shown as a function of transverse momentum or rapidity, systematic uncertainties that are correlated between points are combined and the total correlated uncertainty is indicated by shaded boxes. Uncorrelated uncertainties are indicated by open boxes and the individual data points are allowed to move independently from one another inside these boxes. An example of uncertainties for the jet cross-section in *pp* collisions, jet yields in 0–10% Pb+Pb collisions and R_{AA} in 0–10% (all for $|y| < 2.8$) are shown in Fig. 5.18 (not plotted is the uncertainty due to T_{AA} and luminosity). In the following subsections we describe individual sources of these uncertainties.

5.3.1 Jet energy scale

The strategy for determining JES and its uncertainty for heavy ion jets is discussed in details in Ref. [95]. Here we will summarize the main aspects of this procedure. The JES for heavy ion jets was established by calibrating them to jets with standard *pp* calibration, so called EM+JES jets. This calibration was performed in 8 TeV *pp* data where the absolute energy scale and its uncertainty has previously been evaluated. This JES was then adapted to other beam energies. The components of JES uncertainty are following: baseline, flavor, cross-calibration, and quenching.

The baseline component is obtained from the corresponding uncertainty for the EM+JES jets (the globally reduced set of nuisance parameters (NP) were used). The flavor components include the flavor composition and flavor response components. These components are derived using the same procedure as for the EM+JES jets, but the flavor fractions are evaluated at the appropriate center-of-mass energy. The cross-calibration serves as an alternative derivation of the in-situ calibration [3] of HI jets while also accounting for any residual differences

[3] Data driven calibration for the difference in the JES between the data and MC.

arising from the difference in the reconstruction procedures themselves. These components of JES uncertainty were found correlated between Pb+Pb and pp collisions. A break down of uncertainties due to JES on pp cross-section is shown in Fig. 5.17.

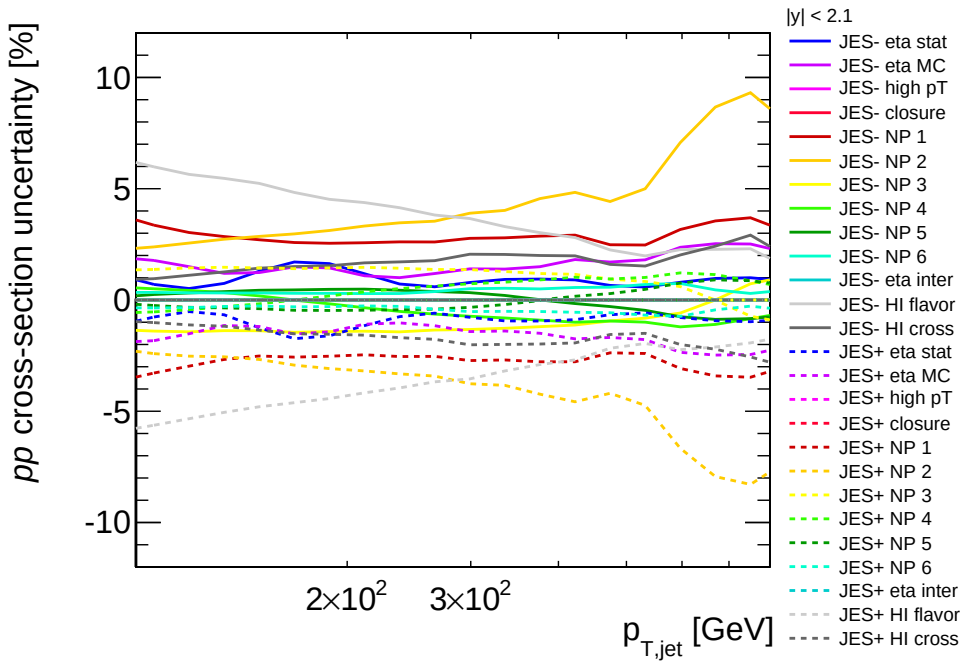

Figure 5.17: A break down of uncertainties due to JES on pp cross-section.

The quenching component reflects a modification of parton showers by the Pb+Pb environment. The resulting jets may have different flavor compositions, or more generally different particle content. The impact of this on the JES was estimated using a data driven study of the ratio of p_{T} of calorimeter jet to the p_{T} of corresponding track jet, defined as r_{trk}. A double ratio,

$$\frac{r_{trk}(Data)/r_{trk}(MC)|_{HI}}{r_{trk}(Data)/r_{trk}(MC)|_{pp}}, \tag{5.3}$$

was evaluated and it was found that a typical difference between $0-10\%$ centrality bin and pp is 0.5%. This difference further linearly decreases with decreasing centrality. This difference was then reflected as an independent uncorrelated component of the JES uncertainty.

For each component of the JES uncertainty the MC reconstruction is run separately and a new response matrix is obtained by shifting the p_{T} of jet as follows

$$p_{\mathrm{T}}^{\star,\mathrm{reco}} = p_{\mathrm{T}}^{\mathrm{reco}}(1 \pm U^{\mathrm{JES}}(p_{\mathrm{T}}, y)). \tag{5.4}$$

where $p_{\mathrm{T}}^{\star,\mathrm{reco}}$ is new jet p_{T} related to a given uncertainty $U^{\mathrm{JES}}(p_{\mathrm{T}}, y)$. These response matrices are then used to unfold the data. A difference between the data unfolded with the new response matrix and the original data is used to determine the systematic uncertainty according to formulae given at the beginning of this section.

5.3.2 Jet energy resolution

Similarly to the JES uncertainty, the systematic uncertainty due the jet energy resolution was also obtained by performing the unfolding with modified response matrices. The modified response matrices were generated for both the *pp* and Pb+Pb collisions using the ATLAS standard JER uncertainty provider tool which provides uncertainty on the fractional resolution, $\sigma_{\mathrm{JER}}^{\mathrm{syst}}$ as a function of jet p_{T} and rapidity. An additional uncertainty which is specific for heavy-ion jet collections was used. Both of these components were used to smear the reconstructed jet p_{T} as follows

$$p_{\mathrm{T}}^{\star,\mathrm{reco}} = p_{\mathrm{T}}^{\mathrm{reco}} \times \mathcal{N}(1, \sigma_{\mathrm{JER}}^{\mathrm{eff}}) \,, \tag{5.5}$$

where $\mathcal{N}(1, \sigma_{\mathrm{JER}}^{\mathrm{eff}})$ is the normal distribution with the effective resolution $\sigma_{\mathrm{JER}}^{\mathrm{eff}} = \sqrt{(\sigma_{\mathrm{JER}} + \sigma_{\mathrm{JER}}^{\mathrm{syst}})^2 - \sigma_{\mathrm{JER}}^2}$.

5.3.3 Unfolding

To minimize the differences between the data and the MC, the response matrices used for the unfolding of the data were reweighted by a ratio of raw reconstructed jet spectra in the data to raw reconstructed jet spectra in the MC as described in Sec. 5.2.2. These reweighted response matrices were used to obtain all the results including the estimates of uncertainties described above. The difference between the data unfolded with the reweighted response matrices and the data unfolded with response matrices without the reweighting was used to calculate the uncertainty due to the unfolding procedure.

5.3.4 T_{AA} and luminosity

The uncertainty on the T_{AA} arise from geometric modeling uncertainty (e.g. nucleon-nucleon inelastic cross-section, Woods-Saxon parameterization of the nucleon positions) and the uncertainty on the fraction of selected inelastic Pb+Pb collisions (the "efficiency" uncertainty). The values of these uncertainties along with T_{AA} are tabulated in Tab. 5.3.

The integrated luminosity determined for 2015 *pp* data was calibrated based on data from dedicated beam-separation scans, known as Van der Meer scans. Determination of systematic uncertainty followed the procedure described in [98] leading to relative uncertainty $\delta\mathcal{L}/\mathcal{L} = 5.4\%$. These uncertainties were evaluated by colleagues from the "global" working group and luminosity working group.

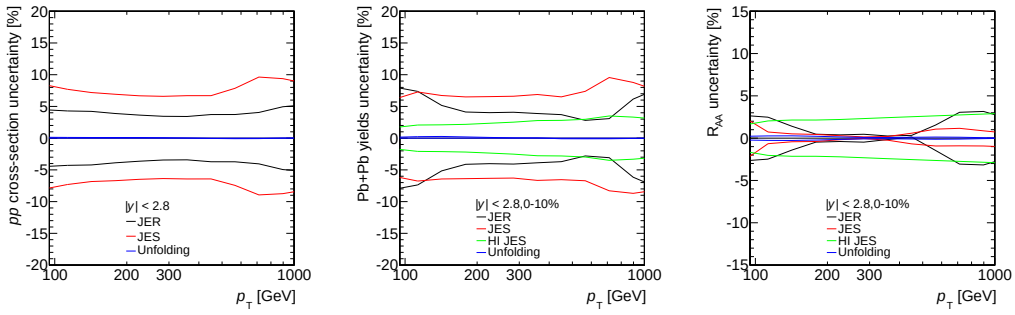

Figure 5.18: Typical systematic uncertainties, for *pp* jet cross-section (left), Pb+Pb yields (middle), and R_{AA} (right).

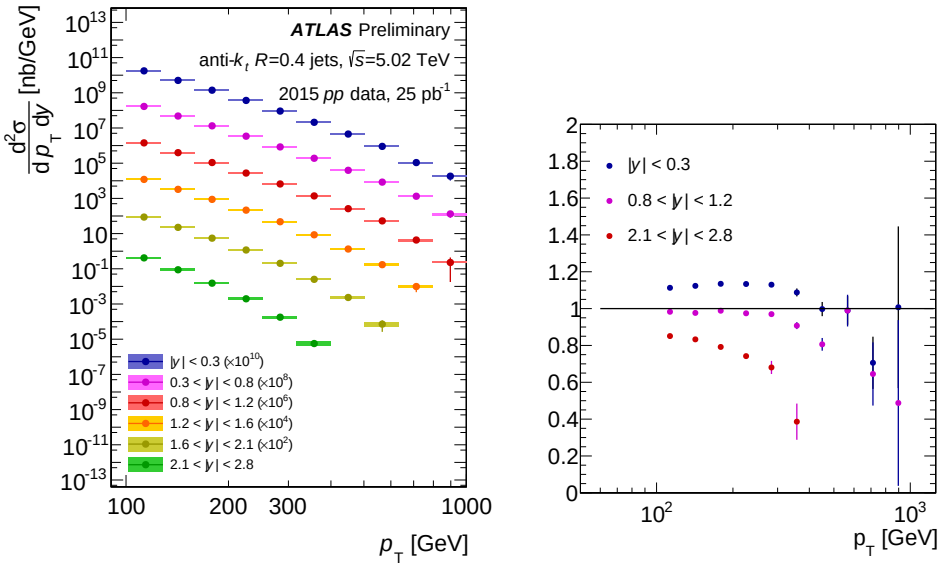

Figure 5.19: Left: Inclusive jet cross-section in *pp* data for several rapidity selections (markers) scaled by successive powers of 10^2. Right: Data to MC ratio of inclusive jet cross-sections for three rapidity bins.

5.4 Results

5.4.1 Inclusive jet cross-section in *pp* collisions and jet yields in Pb+Pb collisions

The unfolded inclusive jet cross-section obtained from *pp* collision data is shown in the left panel of Fig. 5.19. The cross-section is reported for six bins in rapidity and compared to the MC expectation which comes from the cross-section of truth jets obtained from POWHEG+PYTHIA8 dataset specified in Sec. 5.1.2. The ratio between the data and MC is shown in the right panel of Fig. 5.19. The disagreement seen between the data and MC is similar in magnitude as that seen in 8 TeV inclusive jet cross-section analysis (see Fig. 9 in Ref. [99]).

Fig. 5.20 shows the Pb+Pb yields scaled by T_{AA} compared to *pp* cross-section for four selection in centrality and for jet rapidity of $|y| < 2.8$.

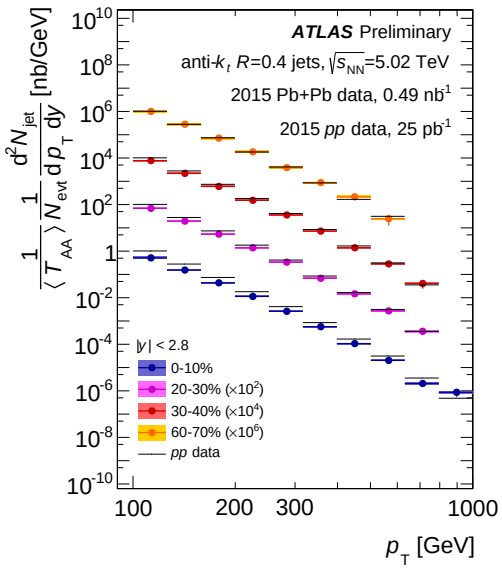

Figure 5.20: Per event jet yield in Pb+Pb collisions, multiplied by $1/T_{\mathrm{AA}}$, as a function of jet p_{T} scaled by successive powers of 10^2. The solid lines represent the pp cross-section for the same rapidity selection scaled by the same factor.

5.4.2 Unfolded jet R_{AA}

The nuclear modification factor evaluated as a function of jet p_{T} is shown in the upper panel of Fig. 5.21 for three centrality selections. The R_{AA} is evaluated for jets with p_{T} in the interval of 100–1000 GeV and $|y| < 2.8$. A clear suppression of the jet production in central Pb+Pb collisions with respect to pp collisions can be seen.

In 0–10% central collisions the R_{AA} reaches a value of approximately 0.45 near $p_{\mathrm{T}} = 100$ GeV. The R_{AA} is observed to grow slowly with increasing jet momentum reaching a value of ≈ 0.6 for jets with $p_{\mathrm{T}} \approx 800$ GeV. The error bars in the figure represent the statistical uncertainties. Shaded boxes represent fully correlated systematic uncertainties for which all the data-points can move upward or downward for a given change in the uncertainty. The open boxes then represent uncorrelated systematic uncertainties for which individual data-points can move within a given uncertainty box.

The R_{AA} evaluated for jets with $|y| < 2.1$ can be compared with the result of the previous measurement performed at $\sqrt{s_{\mathrm{NN}}} = 2.76$ TeV [12]. This is shown for the centrality selection of 0–10% in the lower panel of Fig. 5.21. The two measurements report the same magnitude of the R_{AA} within systematics uncertainties.

The rapidity dependence of the R_{AA} is shown in Fig. 5.22 by evaluating the ratio of the R_{AA} as a function of rapidity to the R_{AA} at $|y| < 0.3$. This representation was chosen because the systematic uncertainties almost completely cancel in the ratio. This is shown in bins of increasing values of jet p_{T} in four panels. The rapidity dependence is shown to be flat with rapidity at lower jet p_{T}. As the jet p_{T} is increased the R_{AA} decreases with rapidity which is seen most significantly in the highest jet p_{T} bin.

The $\langle N_{\mathrm{part}}\rangle$ dependence of the R_{AA} is shown in Fig. 5.23 for jets with $|y| < 2.8$

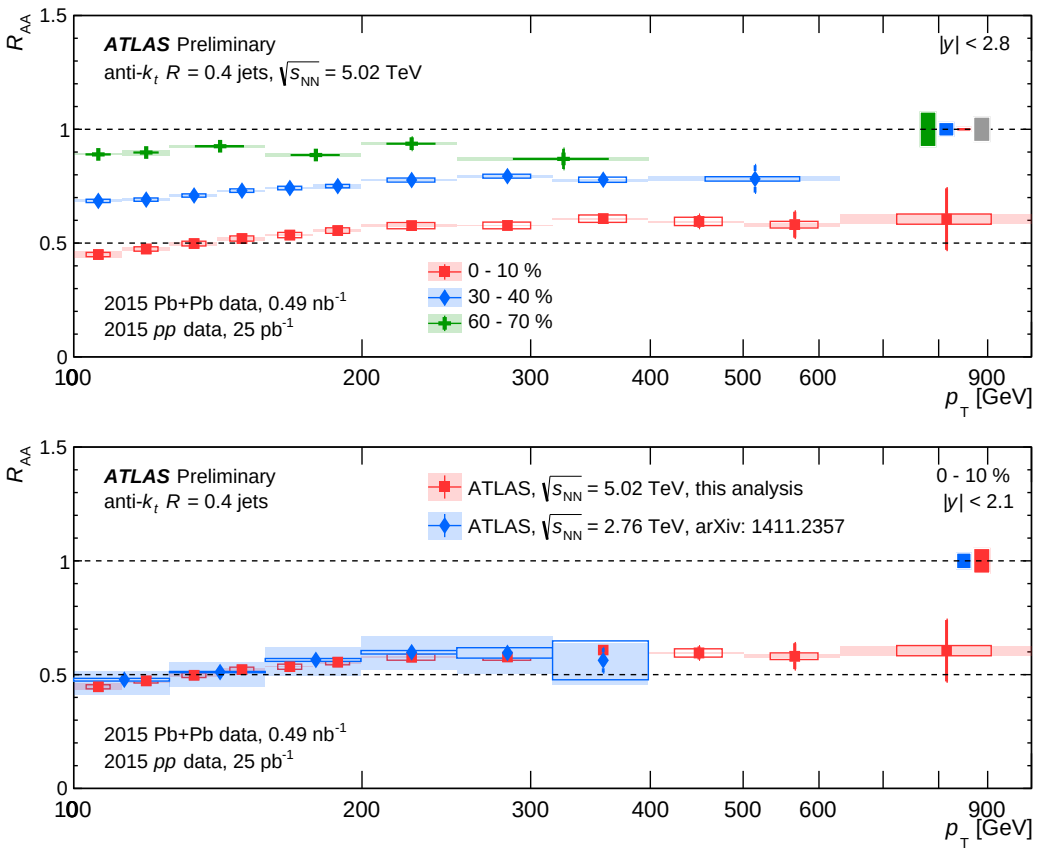

Figure 5.21: Upper panel: The R_{AA} as a function of jet p_{T} for jets with $|y| < 2.8$ for four centrality bins. Lower panel: The R_{AA} as a function of jet p_{T} for jets with $|y| < 2.1$ in 0–10% central collisions compared to the same quantity measured in $\sqrt{s_{\mathrm{NN}}} = 2.76$ Pb+Pb collisions published in Ref. [12]. The error bars represent statistical uncertainties, the shaded boxes around the data points represent correlated systematic uncertainties, open boxes represent uncorrelated systematic uncertainties. In the upper panel, the colored shaded boxes at unity represent T_{AA} uncertainties and the gray shaded box represents the uncertainty on pp luminosity. In the lower panel, the colored shaded boxes at unity represent the combined T_{AA} uncertainties with the uncertainties on pp luminosity.

and $p_{\mathrm{T}} = 100 - 125$ GeV. A smooth evolution of the R_{AA} is seen with the largest values in the most peripheral collision and the smallest values in the most central collisions. The error band here represents the correlated systematic uncertainties which include also the uncertainty on T_{AA}, the open boxes represent uncorrelated systematic uncertainties. The statistical uncertainties are smaller than the data points for all R_{AA} values.

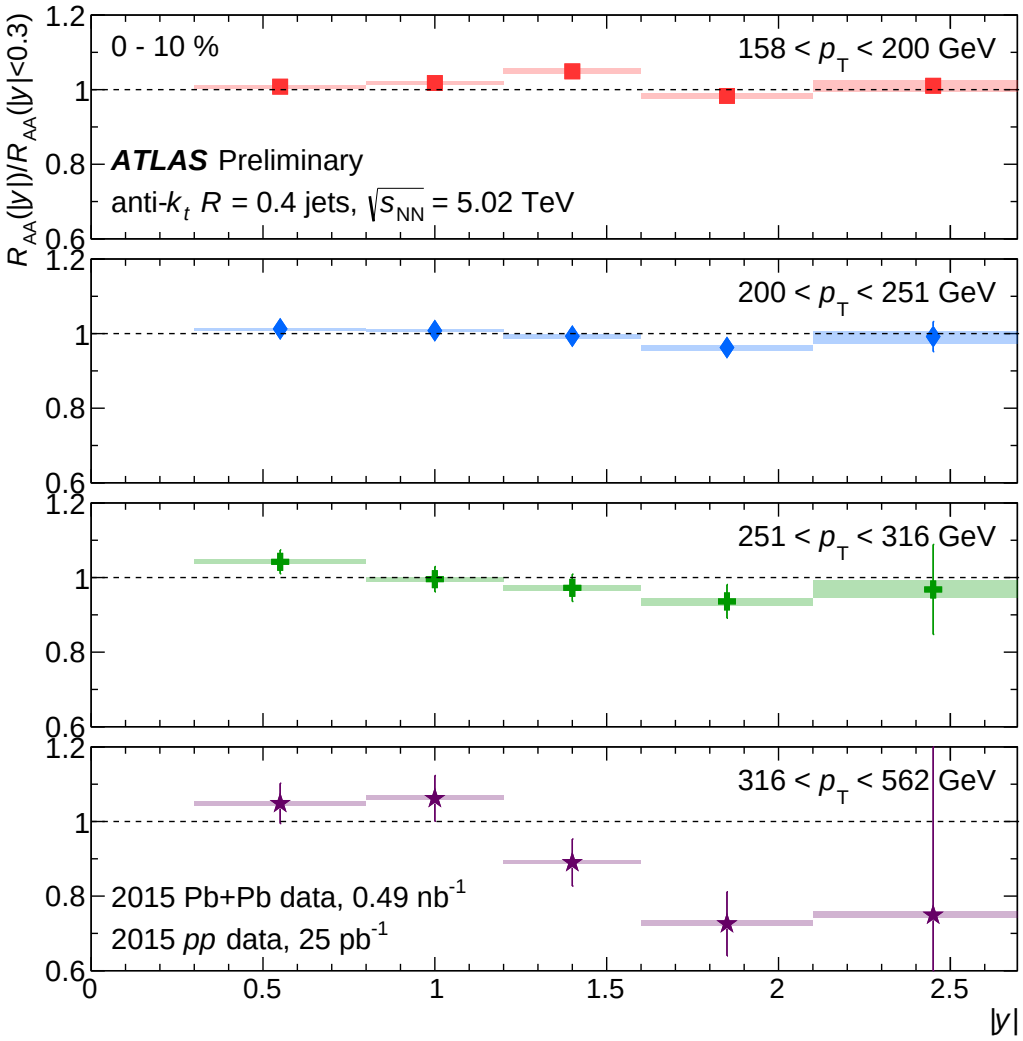

Figure 5.22: The ratio of the R_{AA} as a function of $|y|$ to the R_{AA} at $|y| < 0.3$ for jets with centrality of 0–10% in the following p_{T} bins on each panel: 158 $< p_{\mathrm{T}} <$ 200 GeV (red squares), 200 $< p_{\mathrm{T}} <$ 251 GeV (blue diamonds), 251 $< p_{\mathrm{T}} <$ 316 GeV (green crosses), and 316 $< p_{\mathrm{T}} <$ 562 GeV (purple stars). The error bars represent statistical uncertainties, the shaded boxes around the data points represent correlated systematic uncertainties.

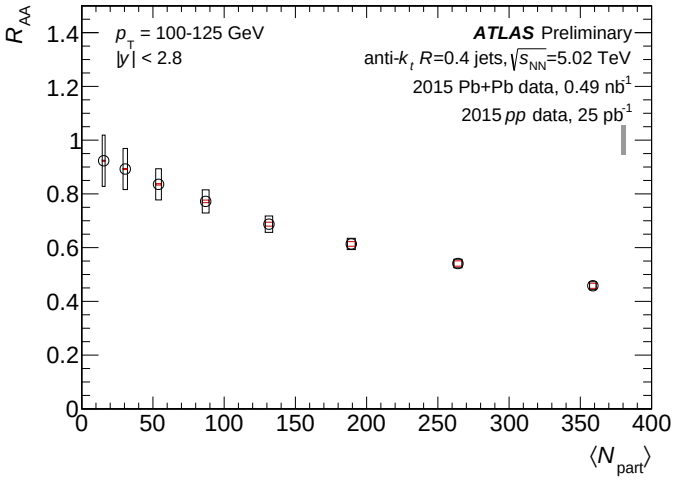

Figure 5.23: The R_{AA} for jets with $p_{\mathrm{T}} = 100 - 125$ GeV and $|y| < 2.8$ evaluated as a function of $\langle N_{\mathrm{part}} \rangle$. The error band represents the correlated systematic uncertainties, the open boxes represent uncorrelated systematic uncertainties. The statistical uncertainties are smaller than the data-points. Gray shaded box represents the uncertainty on pp luminosity.

6. Other results on fragmentation functions and nuclear modification factor at the LHC

This chapter contains a summary of selected results on the jet fragmentation functions and jet nuclear modification factor measured at the LHC in Pb+Pb and *pp* collisions with the ATLAS, CMS and ALICE detector.

6.1 Fragmentation functions

First measurement of fragmentation functions at $\sqrt{s_{\mathrm{NN}}} = 2.76$ TeV with the ATLAS detector

In the first measurement of the jet fragmentation by ATLAS [9], the jet fragmentation functions were measured for jets with the radius parameters $R = 0.2, 0.3,$ and 0.4 using a Pb+Pb data-set recorded in 2011 at $\sqrt{s_{\mathrm{NN}}} = 2.76$ TeV with an integrated luminosity of 0.14 nb^{-1}. The $D(z)$ and $D(p_{\mathrm{T}})$ distributions, introduced in Sec. 1.6, were presented for seven bins in collision centrality. Jet fragments having minimum p_{T} of 2 GeV were measured within an angular range of $\Delta R = 0.4$ from the jet axis. The minimum jet p_{T} requirements for the three sizes of jet were $p_{\mathrm{T}} > 85, 92,$ and 100 GeV, for $R = 0.2$, $R = 0.3$, and $R = 0.4$ jets, respectively. The fragmentation functions were unfolded using a one-dimensional Singular Value Decomposition (SVD) method [100] to remove the effects of charged particle and jet p_{T} resolution. Ratios of fragmentation functions in the different centrality bins to the 60–80% bin were presented and used to evaluate the medium caused modifications of the jet fragmentation. Those ratios, shown in Fig. 6.1, exhibited an enhancement in fragment yield in central collisions for $z \lesssim 0.04$, a reduction in fragment yield for $0.04 \lesssim z \lesssim 0.2$ and an enhancement in the fragment yield for $z > 0.4$. The modifications were found to decrease monotonically with decreasing collision centrality from 0–10% to 50–60%. A similar set of modifications was observed in the $D(p_{\mathrm{T}})$ distributions over corresponding p_{T} ranges.

Measurement of jet fragmentation in 5.02 TeV in Pb+Pb and *pp* collisions with the ATLAS detector

The preliminary measurement of the fragmentation in $\sqrt{s_{\mathrm{NN}}} = 5.02$ TeV for Pb+Pb and *pp* collisions with the ATLAS detector was done using data sets with an integrated luminosity of 0.49 nb^{-1} and 25 pb^{-1}, respectively [101]. The data samples were recorded in 2015. The measurement uses the efficiency corrected track with the $p_{\mathrm{T}} > 4$ GeV that were reconstructed from hits in the inner detector using the track reconstruction algorithm with settings optimized for the high hit density in heavy ion collisions. Jets are reconstructed with the anti-k_t jet finding algorithm with the distance parameter $R = 0.4$. The measurement was done for jets within the momentum range $126 < p_{\mathrm{T}}^{\mathrm{jet}} < 501$ GeV and rapidity $|y| < 2.1$

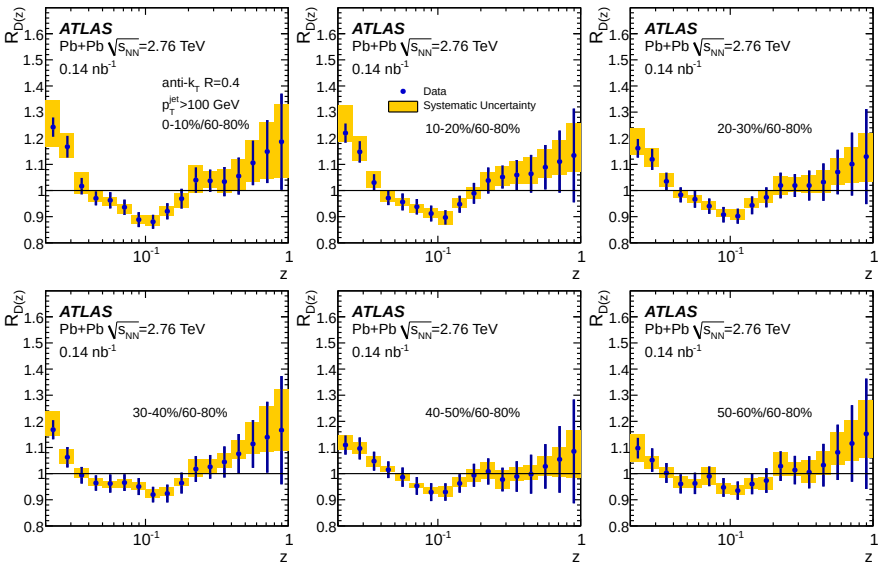

Figure 6.1: Ratios of $D(z)$ for six bins in collision centrality to those in peripheral (60-80%) collisions for $R = 0.4$ jets. The error bars on the data points indicate statistical uncertainties while the yellow shaded bands indicate systematic uncertainties [9].

such that all $R = 0.4$ jet cones are contained within the inner detector acceptance. Analysis used the same strategy as the analysis presented in Chapter 4.

The fragmentation functions were background subtracted and corrected for the detector effects using the two dimensional Bayesian unfolding. For the normalisation of the unfolded spectra, a one-dimensional Bayesian unfolding was used to correct the measured $p_{\mathrm{T}}^{\mathrm{jet}}$.

The trends of the modifications, described as ratio $R_{D(z)}$ defined by Eq. (4.8), are similar in all centralities with a suppression for z below approximately 0.3 and an enhancement at higher z, see Fig. 6.2. In the 0–10% central collisions the enhancement is approximately 20% at the highest z values and the suppression is approximately 15% at the lowest z values. This is qualitatively consistent with measurements at 2.76 TeV described in Chapter 4. Due to the 4 GeV track p_{T} cut in this analysis, there is no sensitivity to the low z enhancement which was seen at 2.76 TeV.

Measurement of jet fragmentation in lead-lead and proton-proton collisions at 2.76 TeV with the CMS detector

The difference in measurement of the fragmentation functions between CMS and ATLAS is that CMS uses a different definition of the fragmentation function, $D(\xi)$, which is defined as function ξ instead of z [10]:

$$D(\xi) \equiv \frac{1}{N_{\mathrm{jet}}} \frac{\mathrm{d}N_{\mathrm{track}}}{\mathrm{d}\xi}, \qquad z = \frac{p_{||}^{\mathrm{track}}}{p_{\mathrm{T}}^{\mathrm{jet}}}, \qquad \xi = \ln\frac{1}{z}, \tag{6.1}$$

where N_{jet} is the total number of jets, N_{track} is the number of charged particles associated with a jet, $p_{||}^{\mathrm{track}}$ is the momentum component of the track along the

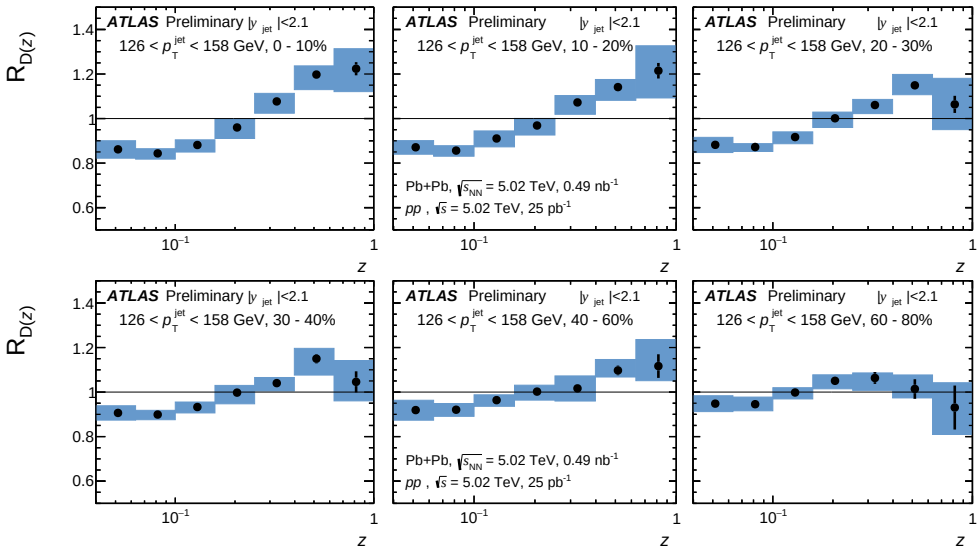

Figure 6.2: Centrality dependence of the unfolded ratios of $D(z)$ in Pb+Pb collisions to those in pp collisions measured with the ATLAS detector at $\sqrt{s_{\mathrm{NN}}} = 5.02$ TeV for $p_{\mathrm{T}}^{\mathrm{jet}}$of 126 to 158 GeV within rapidity $|y_{\mathrm{jet}}| < 2.1$. The statistical uncertainties are shown as bars and the systematic uncertainties are shown as shaded areas [101].

jet axis and $p_{\mathrm{T}}^{\mathrm{jet}}$ is the magnitude of the jet momentum.

CMS utilized Pb+Pb collisions collected in 2011 at $\sqrt{s_{\mathrm{NN}}} = 2.76$ TeV with integrated luminosity of 150 $\mu\mathrm{b}^{-1}$ and pp collisions recorded in 2013 at the same center-of-mass energy with an integrated luminosity of 5.3 pb^{-1}. Further, CMS used $R = 0.3$ jets within p_{T} range $100 < p_{\mathrm{T}}^{\mathrm{jet}} < 300$ GeV and pseudorapidity coverage of $0.3 < |\eta| < 2.0$ with tracks with $p_{\mathrm{T}}^{\mathrm{track}} > 1$ GeV within radius $\Delta R = 0.3$ between track and jet axis. Fragmentation functions were evaluated in five centrality bins: 0–10%, 10–30%, 30–50%, 50–70% and 70–100%. The event centrality was estimated by total energy deposition in Cherenkov hadron forward calorimeter. Main results are shown in Fig. 6.3. One can observe a significant enhancement in ratios of fragmentation functions in Pb+Pb to pp collisions for charged particles with $p_{\mathrm{T}}^{\mathrm{track}} < 3$ GeV that is observed for all $p_{\mathrm{T}}^{\mathrm{jet}}$ bins that were studied. One can also observe a depletion in the ration at intermediate $p_{\mathrm{T}}^{\mathrm{track}}$. Taken into account the differences in ATLAS and CMS measurements of the fragmentation functions and also the important fact that the CMS results are not unfolded to the particle level, a direct comparison with ATLAS results is not possible, though the trends are seemingly similar.

6.2 Jet nuclear modification factor

Nuclear modification factor, R_{AA}, defined in Sec. 1.7 is an established observable in heavy-ion physics and it was measured before by many collaborations. In this section we briefly describe the measurements of the nuclear modification factor at the LHC previously done with by ATLAS, CMS and ALICE experiments.

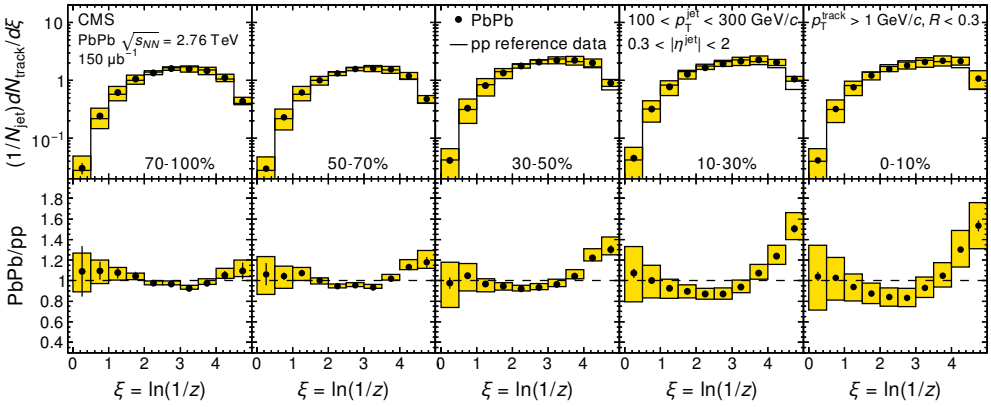

Figure 6.3: Ratios of $D(\xi)$ distributions for five bins in collision centrality to those in pp collisions for $R = 0.3$ jets within $100 < p^{\text{jet}} < 300$ GeV and $0.3 < |\eta| < 2.0$ measured with the CMS detector. The error bars on the data points indicate statistical uncertainties while the yellow shaded bands indicate systematic uncertainties [10].

Measurement of the Jet Size Dependence of Inclusive Jet Suppression in PbPb Collisions at $\sqrt{s_{\text{NN}}} = 2.76$ TeV with the ATLAS Detector

Before discussing the R_{AA}, we will first discuss the measurement of the central-to-peripheral nuclear modification factor, R_{CP} which was defined in Eq. (1.36). It was measured with the ATLAS detector at $\sqrt{s_{\text{NN}}} = 2.76$ TeV [11]. It utilizes 2010 data with the integrated luminosity of approximately 7 μb^{-1}. Jets were reconstructed with the anti-k_t jet-finding algorithm for four different values of the anti-k_t distance parameter, $R = 0.2, 0.3, 0.4$, and 0.5. Jets were measured within the p_{T} range of $38 < p_{\text{T}} < 210$ GeV and within the pseudorapitidy range of $|\eta| < 2.1$. R_{CP} was evaluated in six centrality bins: 0–10%, 10–20%, 20–30%, 30–40%, 40–50% and 50–60%. The measured p_{T} spectra of reconstructed jets were corrected for the underlying event and corrected for the effects of the bin migration by the singular value decomposition technique [100].

The centrality dependence of R_{CP} as a function of jet p_{T} for $R = 0.4$ jets is shown in Fig. 6.4. A weak, if any, variation with p_{T} was observed for all centralities. For the most central collisions, 0–10%, the R_{CP} values show a factor of approximately two suppression in the jet yield. For the peripheral collisions, 50–60%, R_{CP} values reach 0.9 for all jet p_{T} value. The jet radius dependence of the suppression is shown in Fig. 6.5 for the 0–10% centrality bin and for four jet p_{T} intervals (left) and for different centrality classes in the $158 < p_{\text{T}} < 182$ GeV bin (right). The results in Fig. 6.5 show a weak variation of R_{CP} with the distance parameter R but when taken into account the systematic errors, it is not significant.

Measurements of the Nuclear Modification Factor for Jets in Pb+Pb Collisions at $\sqrt{s_{\text{NN}}} = 2.76$ TeV with the ATLAS detector

ATLAS measured the jet nuclear modification factor, R_{AA}, at $\sqrt{s_{\text{NN}}} = 2.76$ TeV using Pb+Pb data with an integrated luminosity of 0.14 nb^{-1} recorded in 2011 and pp data with an integrated luminosity of 4.0 pb^{-1}collected in 2013 [12]. Jets

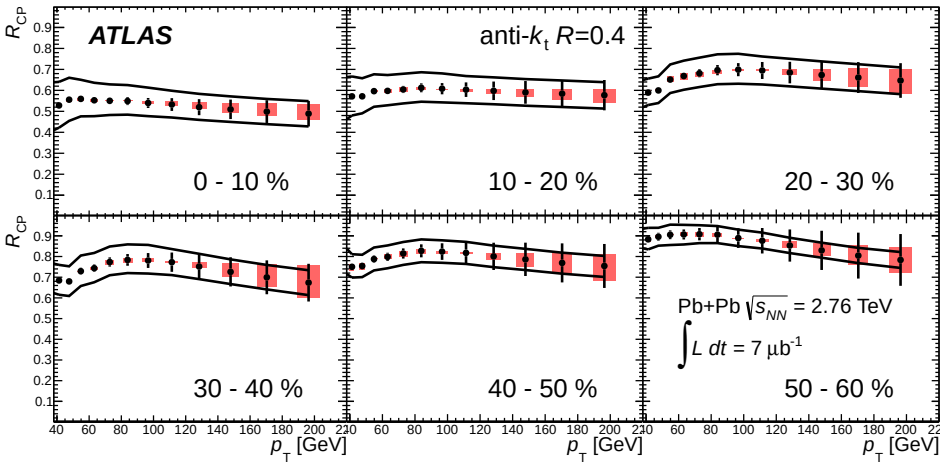

Figure 6.4: R_{CP} as a function of jet p_{T} for all centrality bins for $R = 0.4$ jets measured with the ATLAS detector. The error bars indicate statistical errors from the unfolding; the shaded boxes indicate point-to-point systematic errors that are only partially correlated. The solid lines indicate systematic errors that are fully correlated between all points. The horizontal width of the systematic error band is chosen for presentation purposes only [11].

were reconstructed with the anti-k_t algorithm with $R = 0.4$ and the spectra were measured over the kinematic range of $32 < p_{\mathrm{T}} < 500$ GeV, rapidity $|y| < 2.1$ and as a function of centrality. The jet R_{AA} as a function of p_{T} is shown in Fig. 6.6 on the left panel for different jet rapidity and centrality classes. Jet p_{T} dependence is observed to increase weakly with p_{T} except in the most peripheral bin. In the central collisions, 0–10%, the R_{AA} values show a factor of approximately two suppression in the jet yield. In the most peripheral bin, 60–80%, the jet yield in Pb+Pb collisions is still significantly suppressed with respect to the yield in pp collisions. The rapidity dependence is shown in the top right panel of Fig. 6.6, for jets with $80 < p_{\mathrm{T}} < 100$ GeV and for three centrality bins. The R_{AA} does not change within rapidity over the p_{T} range. The N_{part} dependence is shown on the bottom right panel for jets in the same p_{T} interval and with $|y| < 2.1$. The R_{AA} decreases gradually moving form the most peripheral to central collisions, where it reaches a value of approximately 0.4 for the 0–1% centrality bin.

Measurement of inclusive jet cross sections in pp and Pb+Pb collisions at $\sqrt{s_{\mathrm{NN}}} = 2.76$ TeV with the CMS detector

The CMS Collaboration also measured the jet R_{AA} using Pb+Pb collisions at $\sqrt{s_{\mathrm{NN}}} = 2.76$ TeV recorded in 2011 with an integrated luminosity of 166 $\mu\mathrm{b}^{-1}$ and pp collisions at the same center-of-mass energy recorded in 2013 with an integrated luminosity of 5.43 pb^{-1} [102]. Jets were reconstructed using the anti-k_t jet finding algorithm with $R = 0.2, 0.3, 0.4$ and only jets within momentum range of $70 < p_{\mathrm{T}} < 300$ GeV and pseudorapidity $|\eta| < 2.0$ were used. Results are shown in Fig. 6.7 for different centrality bins and for different distance parameters. The jet R_{AA} decreases with increasing collision centrality in the range of the measured jet p_{T}. Within the systematic uncertainty, the jet R_{AA} shows the same level of

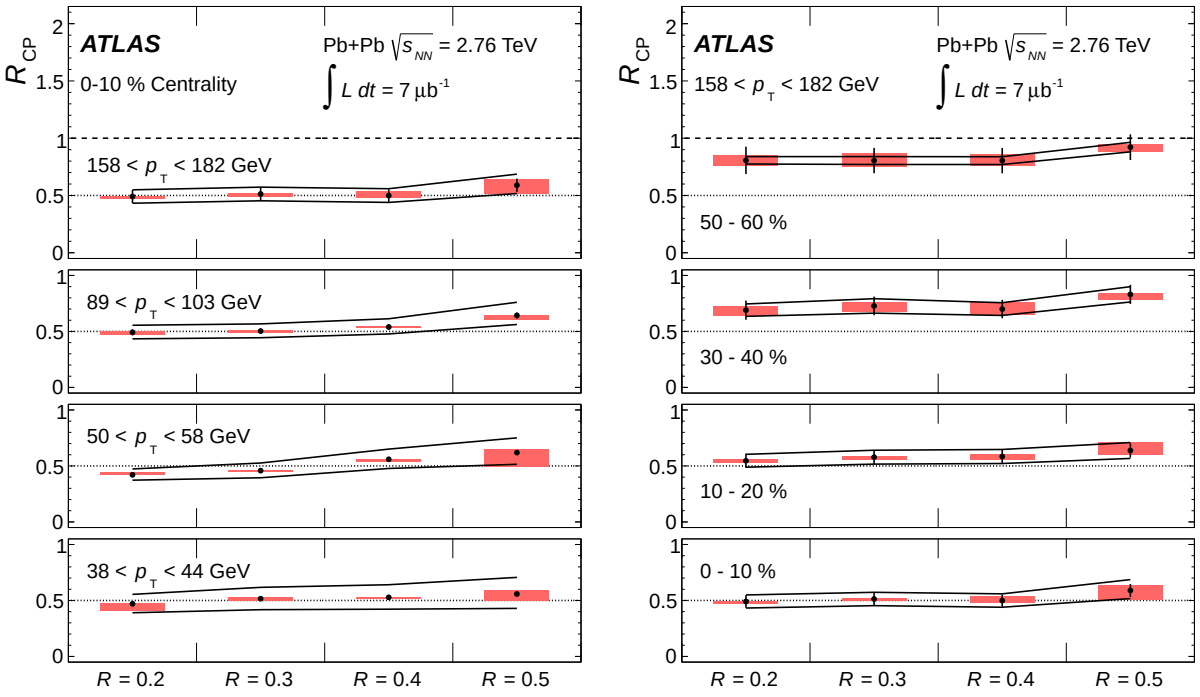

Figure 6.5: Left: R_{CP} in the 0–10% centrality bin as a function of jet radius for four bins of jet p_{T}. Right: R_{CP} as a function of jet radius for four centrality bins for the p_{T} interval $158 < p_{\mathrm{T}} < 182$ GeV. The measurement was done with the ATLAS detector. The error bars indicate statistical errors from the unfolding; the shaded boxes indicate point-to-point systematic errors that are only partially correlated. The solid lines indicate systematic errors that are fully correlated between all points. The horizontal width of the systematic error band is chosen for presentation purposes only. Dotted lines indicate $R_{\mathrm{CP}} = 0.5$, and the dashed lines on the top panels indicate $R_{\mathrm{CP}} = 1$ [11].

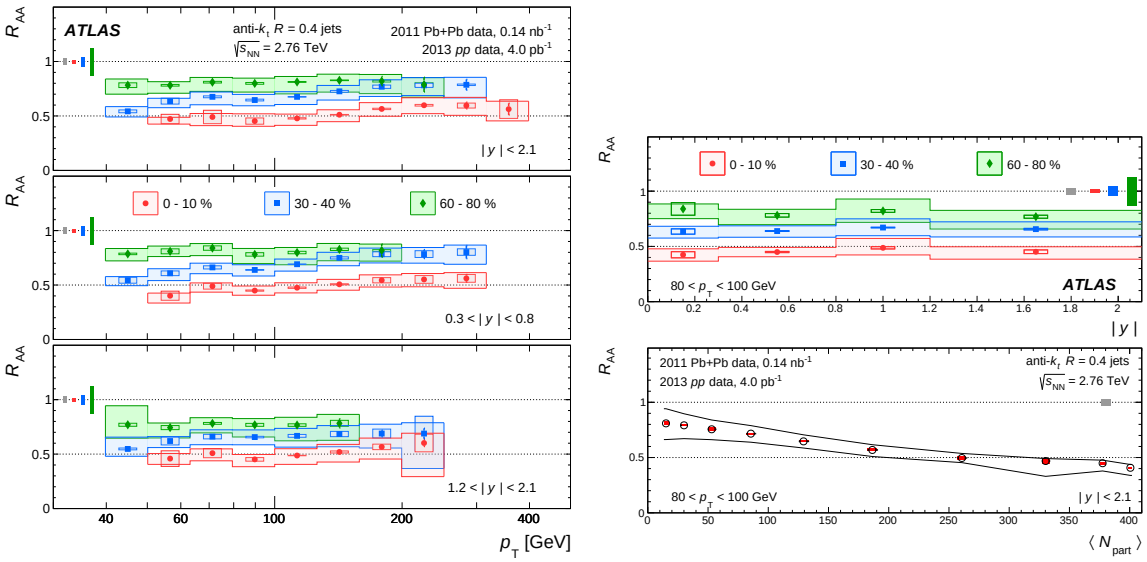

Figure 6.6: Left: Jet R_{AA} as a function of jet p_{T} in different centrality bins. Each panel shows a different range in $|y|$. Right: Jet R_{AA} for jets with $80 < p_{\mathrm{T}} < 100$ GeV as a function of $|y|$ for different centrality bins (top) and as a function of N_{part} for the $|y| < 2.1$ (bottom). The measurement was done with the ATLAS detector. The fractional luminosity and T_{AA} uncertainties are indicated separately as shaded boxes centred at one. The boxes, bands and error bars indicate uncorrelated systematic, correlated systematic and statistical uncertainties, respectively [12].

suppression for the three distance parameters. The pseudorapidity dependence was not studied.

Measurement of jet suppression in central Pb+Pb collisions at $\sqrt{s_{\mathrm{NN}}} = 2.76$ TeV with the ALICE detector

The ALICE Collaboration measured the nuclear modification factor as well [103]. The measurement utilized 15 μb^{-1} Pb+Pb data and 3.7 μb^{-1} pp data at $\sqrt{s_{\mathrm{NN}}} = 2.76$ TeV. The R_{AA} was measured using the transverse momentum spectrum of reconstructed jets in 0–10% and 10-30% Pb+Pb collisions. Jets were reconstructed from charged and neutral particles with the anti-k_t jet algorithm with the distance parameter $R = 0.2$. The jet spectra were measured within the pseudorapidity interval of $|\eta| < 0.5$ and in the momentum range of $40 < p_{\mathrm{T}} < 120$ GeV for 0–10% and in the range of $30 < p_{\mathrm{T}} < 120$ GeV for 10–30% collisions. Reconstructed jets were required to have a leading charge particle with $p_{\mathrm{T}} > 5$ GeV to suppress the combinatorial background in Pb+Pb collisions. The results are shown in Fig. 6.8 for 0–10% on the left panel and for the 10–30% on the right panel. A clear suppression of the jet yields in the Pb+Pb with respect to pp collisions is observed. The R_{AA} is independent of jet p_{T} within the uncertainties of the measurement. The suppression in 10–30% events is 0.35 ± 0.04, slightly less than in the most central events. The ALICE Collaboration compared the results to the calculation of two different jet quenching models, YaJEM [104] and JEWEL [105]. Both calculations are found to reproduce the jet suppression. YaJEM, however, exhibits a slightly steeper increase with jet p_{T} than the data.

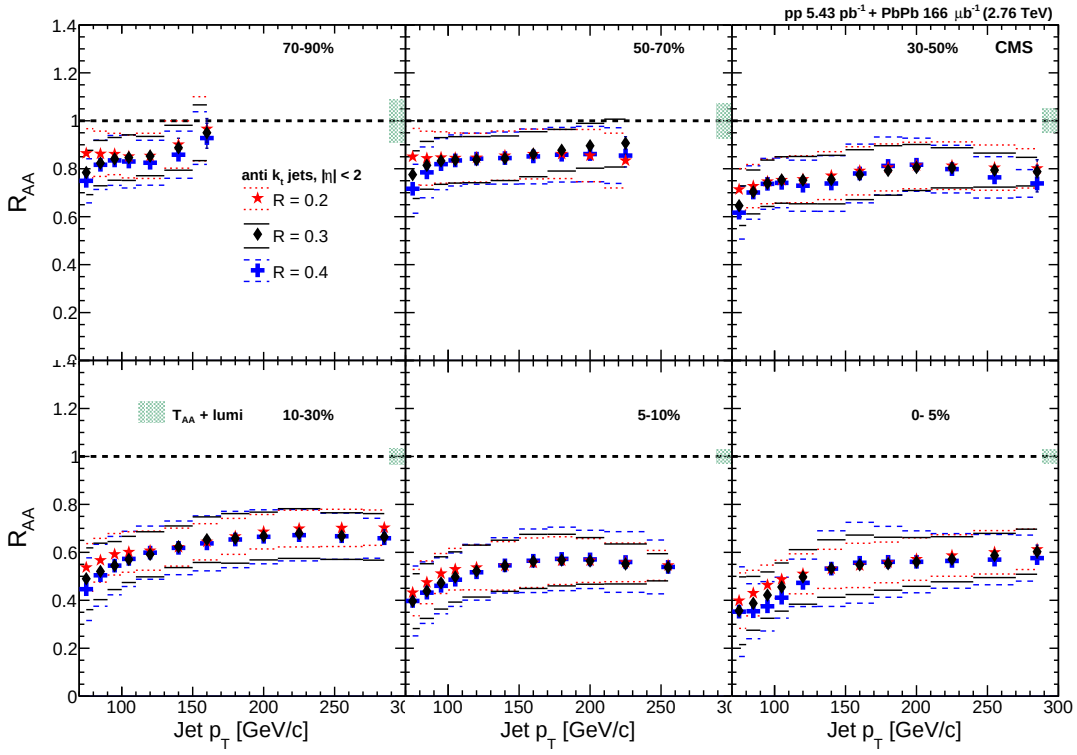

Figure 6.7: Jet R_{AA} for jets with $70 < p_{\mathrm{T}} < 300$ GeV as a function of jet p_{T} for different centrality bins and for different distance parameters $R = 0.2$ (red stars), 0.3 (black diamonds) and 0.4 (blue crosses) measured with the CMS detector. The vertical bars (smaller than the markers) indicate the statistical uncertainty and the systematic uncertainty represented by the bounds of the dotted, solid, and dashed horizontal lines. The uncertainty boxes at unity represent the T_{AA} and luminosity uncertainty [102].

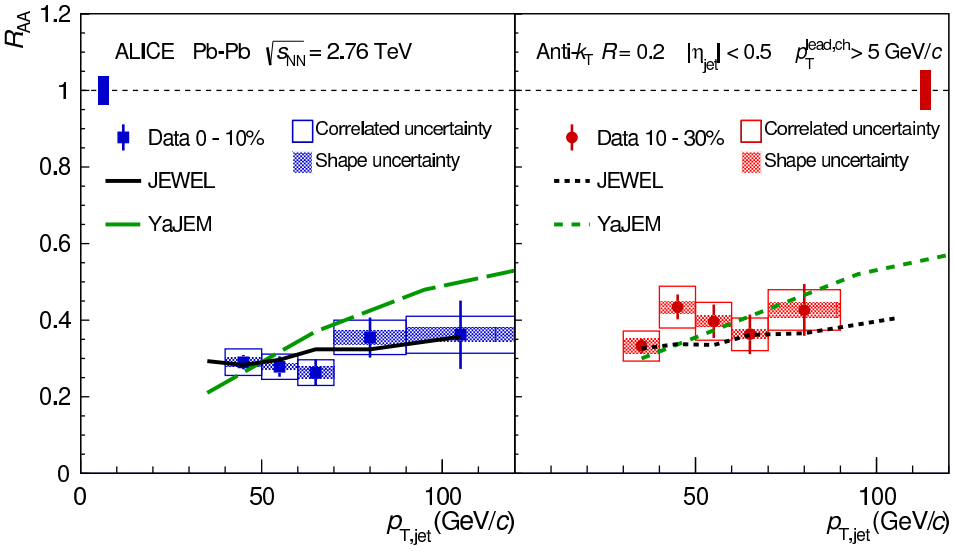

Figure 6.8: Jet R_{AA} for $R = 0.2$ jets with the leading track requirement of 5 GeV in 0–10% (left) and 10–30% (right) Pb+Pb collisions compared to calculation for YaJEM and JEWEL. The measurement was done with the ALICE detector. The boxes at $R_{\mathrm{AA}} = 1$ represent the systematic uncertainty on T_{AA} and pp luminosity [103].

Conclusion

This thesis presented a measurement of jet internal structure and inclusive jet suppression performed with the ATLAS detector at the LHC.

To study the jet fragmentation in details, the distributions of charged particle transverse momentum and longitudinal momentum fraction are measured in jets reconstructed using the anti-k_t algorithm with $R = 0.4$. These distributions are measured differentially in jet p_{T}, jet rapidity, and in both Pb+Pb and pp collisions at a centre-of-mass energy $\sqrt{s_{\mathrm{NN}}} = 2.76$ TeV per colliding nucleon pair. In the case of Pb+Pb collisions, the measurement is performed in bins of collision centrality. The Pb+Pb and pp data correspond to integrated luminosities of 0.14 nb^{-1} and 4.0 pb^{-1}, respectively. The distributions measured in pp collisions are used as a reference for the distributions measured in Pb+Pb collisions to evaluate the impact of the jet energy loss on the jet internal structure. The measurements cover the jet p_{T} range of $100 - 398$ GeV and use charged particles with $p_{\mathrm{T}} > 1$ GeV. The results are corrected to the hadron level.

The ratios of charged particle transverse momentum distributions measured in Pb+Pb collisions to those measured in pp exhibit an enhancement in fragment yield in central collisions for $1 < p_{\mathrm{T}}^{\mathrm{ch}} < 4$ GeV, a reduction in fragment yields for $4 < p_{\mathrm{T}}^{\mathrm{ch}} < 25$ GeV and an enhancement in the fragment yield for $p_{\mathrm{T}}^{\mathrm{ch}} > 25$ GeV. The magnitude of these modifications decreases towards more peripheral collisions. The similar observation can also be made for the distributions of longitudinal momentum fraction.

The centrality dependence of the magnitude of modifications was further quantified by evaluating the differences in integrals of charged particle transverse momentum distributions measured in Pb+Pb and pp collisions for the three characteristic $p_{\mathrm{T}}^{\mathrm{ch}}$ intervals. Further, the jet p_{T}- and rapidity dependence of the modifications in the jet internal structure was measured. No significant differences in modifications of the jet structure are observed among different $p_{\mathrm{T}}^{\mathrm{jet}}$ selections spanning the interval of $100 - 398$ GeV. No significant evolution in modifications of the jet internal structure as a function of rapidity is observed except for the change in the trends at high-$p_{\mathrm{T}}^{\mathrm{ch}}$. In the region of $p_{\mathrm{T}}^{\mathrm{ch}} \gtrsim 40$ GeV, some reduction of the enhancement for more forward jets is observed. These observations are however of a limited significance due to large statistical and systematic uncertainties. These results are described in details in Chapter 4 of this thesis.

Chapter 5 of this thesis presents a measurement of the jet cross-section in pp collisions, inclusive jet yields in Pb+Pb collisions and the jet R_{AA}. The measurement was performed utilizing 25 pb^{-1} pp and 0.49 nb^{-1} Pb+Pb collisions at the nucleon-nucleon centre-of-mass energy of $\sqrt{s_{\mathrm{NN}}} = 5.02$ TeV. The anti-k_t $R = 0.4$ jets were measured over the transverse momenta in the interval of 100–1000 GeV in six rapidity intervals spanning the range of $|y| < 2.8$. The jet yields measured in heavy-ion collisions scaled by the nuclear thickness function, T_{AA}, are observed to be suppressed with respect to the jet cross-section measured in pp collisions. The magnitude of the R_{AA} which quantifies this suppression, monotonically increases from central to peripheral collisions. The R_{AA} is flat with rapidity at low jet p_{T} and then decreases with rapidity at high jet p_{T}.

The rapidity dependence at high jet p_{T} is observed for the first time as a consequence of the availability of the high-statistics data set while the previous measurement was statistically limited at high jet p_{T} and forward rapidity. The magnitude of the suppression as well as its evolution with jet p_{T} and rapidity are consistent with those reported in the similar measurement performed in Pb+Pb collisions at $\sqrt{s_{\mathrm{NN}}} = 2.76$ TeV in the kinematic region where the two measurements overlap.

The new results presented in this thesis extend the previous measurements to significantly higher transverse momenta and larger rapidities of jets as well as improve on the precision of the measurement. This allows for precise and detailed comparisons of the data to theoretical models of the jet quenching. The new results can also be used as additional input needed for understanding the center-of-mass dependence of the jet suppression.

These new measurement of both internal jet structure and inclusive jet suppression presented in this thesis should improve our understanding of the in-medium modifications of parton showers and help to constrain the jet quenching models.

A. Appendix - Jet Fragmentation measurement

In this appendix we show some more figures related to the performance of the jet fragmentation measurement which are not included in the main body of the thesis (see Sec.4).

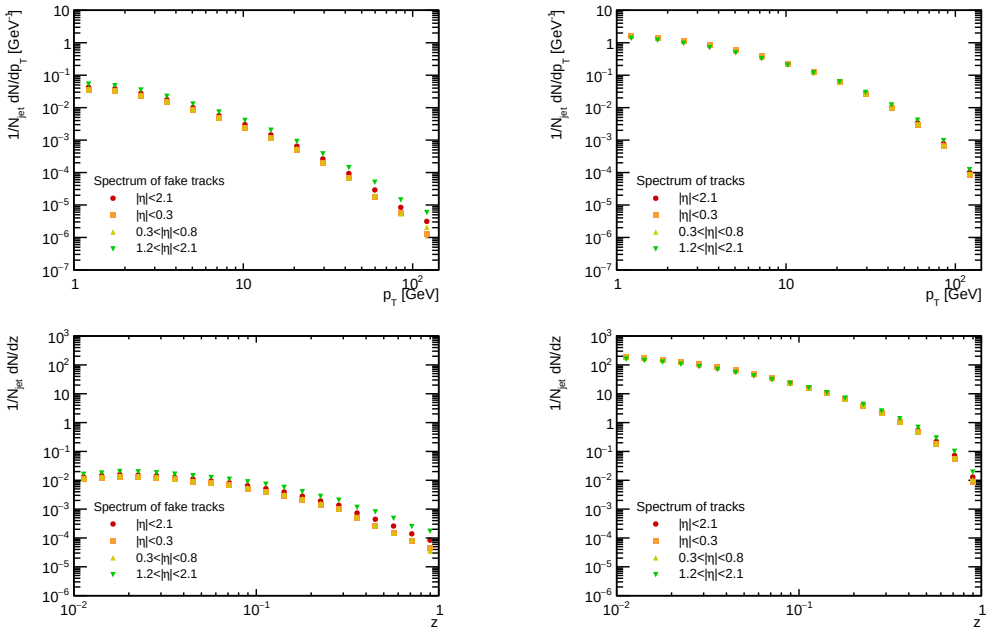

Figure A.1: Upper panel: $D(p_{\mathrm{T}})$ distributions of reconstructed fake tracks (left plot) and $D(p_{\mathrm{T}})$ distributions of reconstructed tracks (right plot) in MC in pp collisions for jets with $p_{\mathrm{T}} > 100$ GeV for four rapidity bins shown in the legend. Lower panel: $D(z)$ distributions of reconstructed fake tracks (left plot) and $D(z)$ distributions of reconstructed tracks (right plot) in MC in pp collisions for jets with $p_{\mathrm{T}} > 100$ GeV for four rapidity bins shown in the legend. Spectrum of fake tracks was obtained by requiring tracks not to match to the particles.

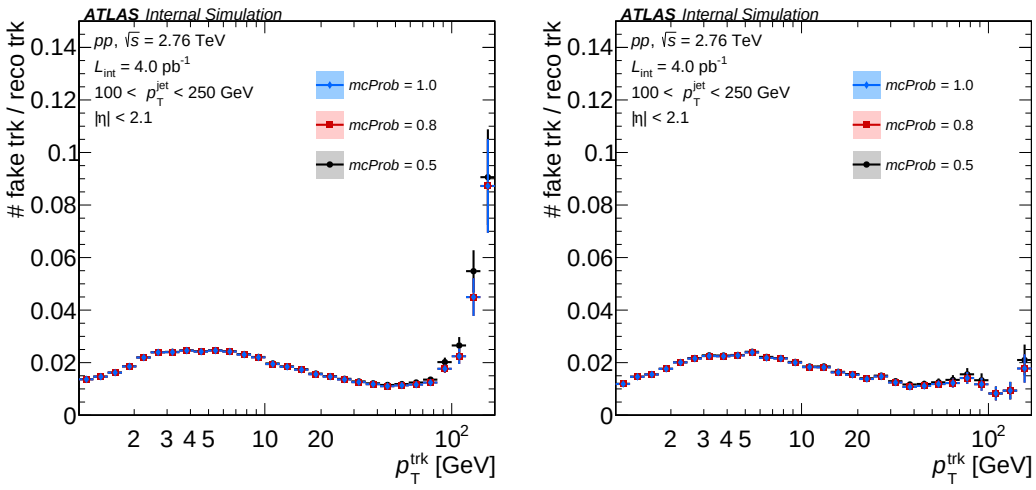

Figure A.2: Ratio of fake tracks to all reconstructed tracks as a function of $p_{\mathrm{T}}^{\mathrm{trk}}$ in pp MC for JZ2 sample (left panel) and JZ4 sample (right panel). Fake tracks were obtained by requesting tracks that do not match particles with three different values of matching parameter *mcProb* showed in the legend. For example $mcProb = 1.0$ means that the probability of matching track to the particle is 1. For both MC samples the fraction is lower that 5% for $p_{\mathrm{T}}^{\mathrm{trk}}$ up to 100 GeV. Measurement was done for jets with pseudorapidity $|\eta| < 2.1$ and $p_{\mathrm{T}}^{\mathrm{jet}}$ in the interval of 100 - 250 GeV. The error bars on the data point indicate statistical uncertainties.

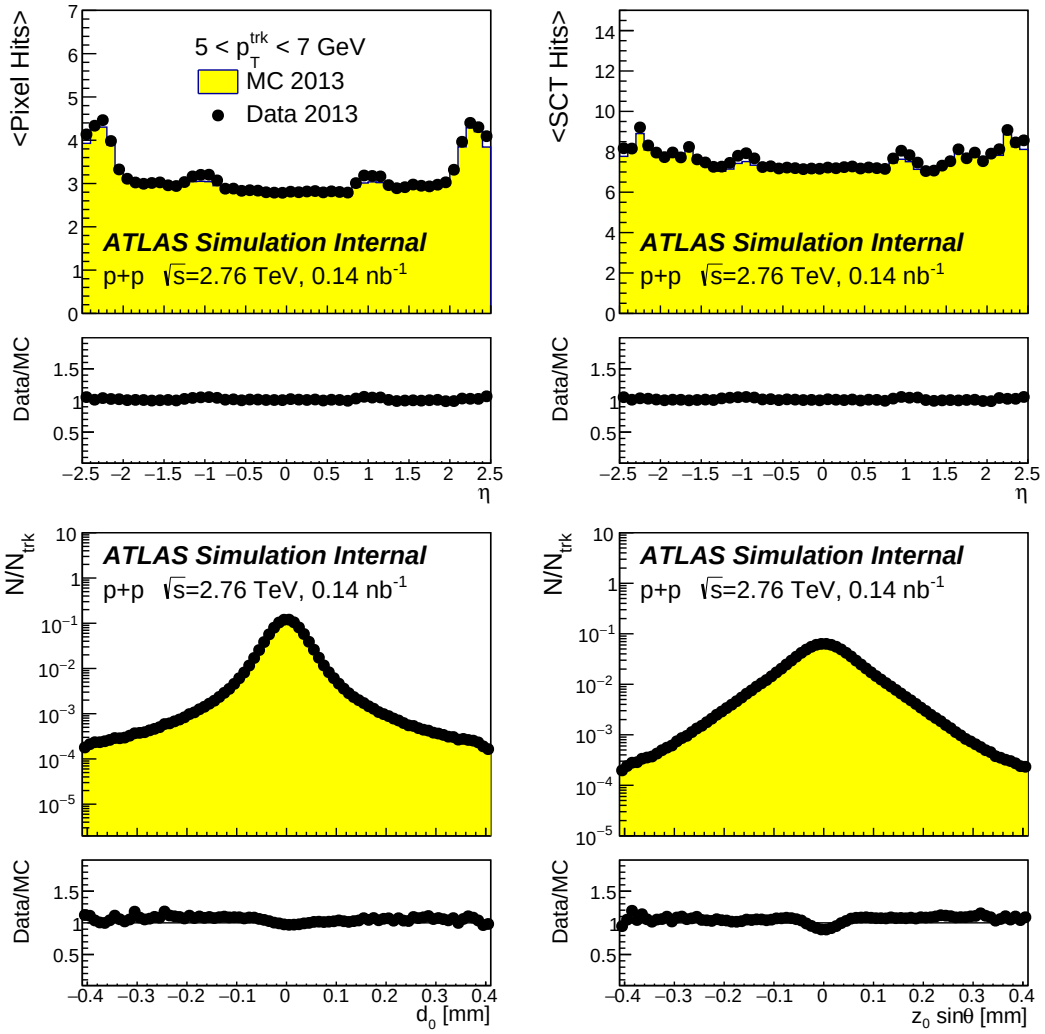

Figure A.3: Upper left panel: Average number of Pixel hits per track. Upper right panel: Average number of SCT hits per track. Lower left panel: The impact parameter d_0 per track. Lower right panel: The impact parameter $z_0 \sin(\theta)$ per track. The pp data 2011 are compared to the pp MC shown with filled histograms.

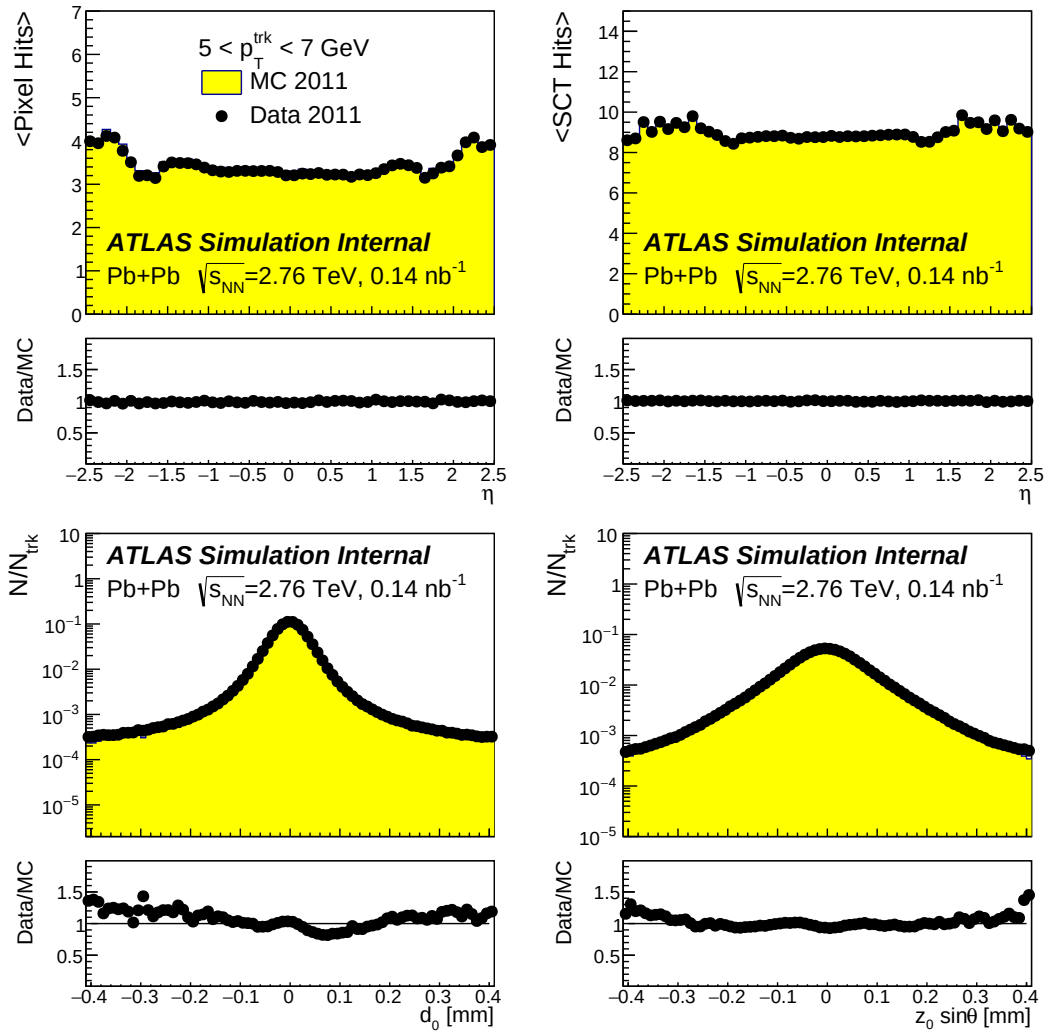

Figure A.4: Upper left panel: Average number of Pixel hits per track. Upper right panel: Average number of SCT hits per track. Lower left panel: The impact parameter d_0 per track. Lower right panel: The impact parameter $z_0 \sin(\theta)$ per track. The Pb+Pb data 2013 are compared to the Pb+Pb MC shown with filled histograms for the most central events.

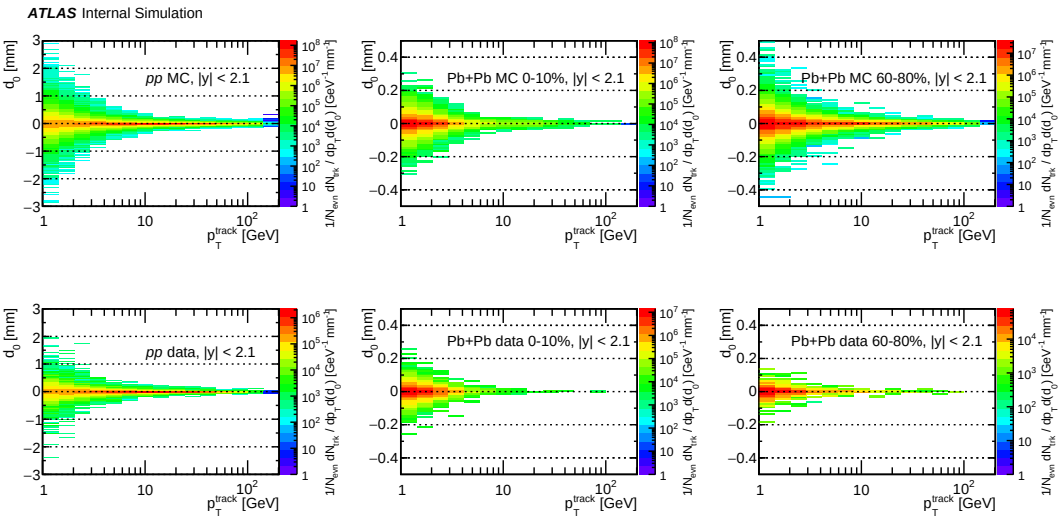

Figure A.5: The impact parameter d_0 as a function of track momentum after applying cuts on d_0 and $z_0 \sin(\theta)$ significance. Each panel show the same distribution in pp and Pb+Pb in data or MC. Corresponding labels are displayed in each panel. All distribution are inclusive in rapidity. The z-axis is $1/N_{events} \mathrm{d}N_{tracks}/(\mathrm{d}p_\mathrm{T}\mathrm{d}(d_0))$.

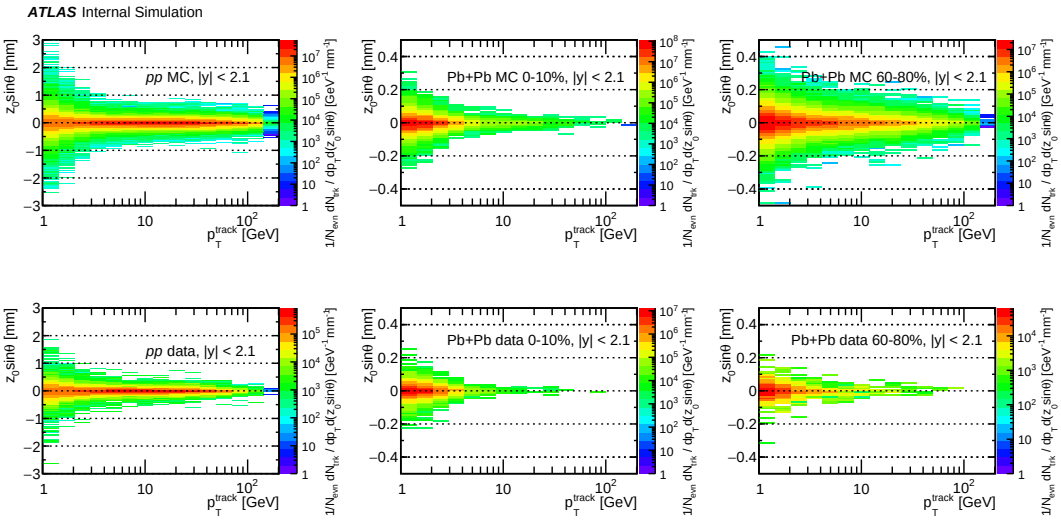

Figure A.6: The impact parameter $z_0 \sin(\theta)$ as a function of track momentum after applying cuts on d_0 and $z_0 \sin(\theta)$ significance. Each panel show the same distribution in pp and Pb+Pb in data or MC. Corresponding labels are displayed in each panel. All distribution are inclusive in rapidity. The z-axis is $1/N_{events} \mathrm{d}N_{tracks}/(\mathrm{d}p_\mathrm{T}\mathrm{d}(z_0 \sin(\theta)))$.

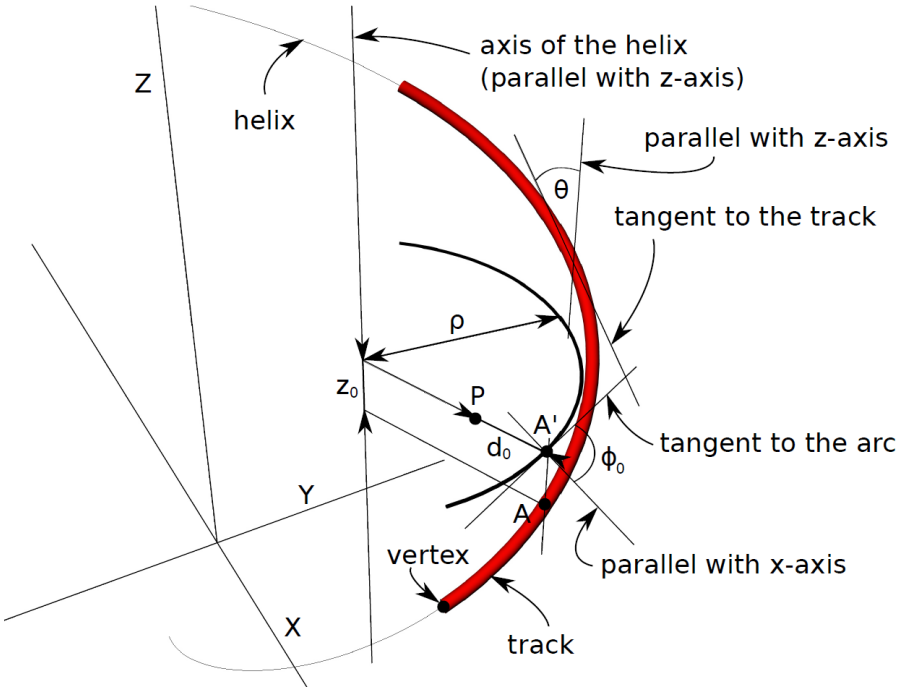

Figure A.7: The track parameters d_0 and z_0.

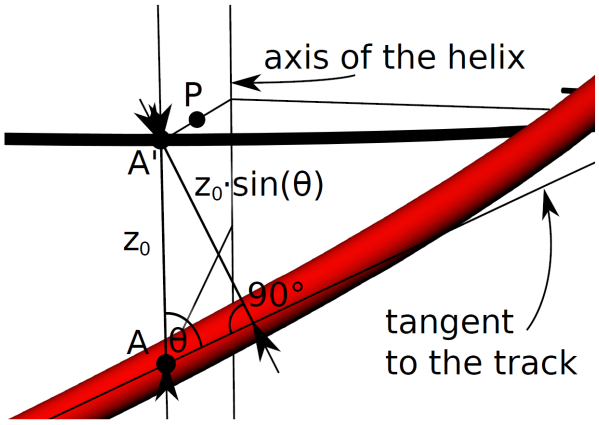

Figure A.8: The track parameters $z_0 \sin\theta$.

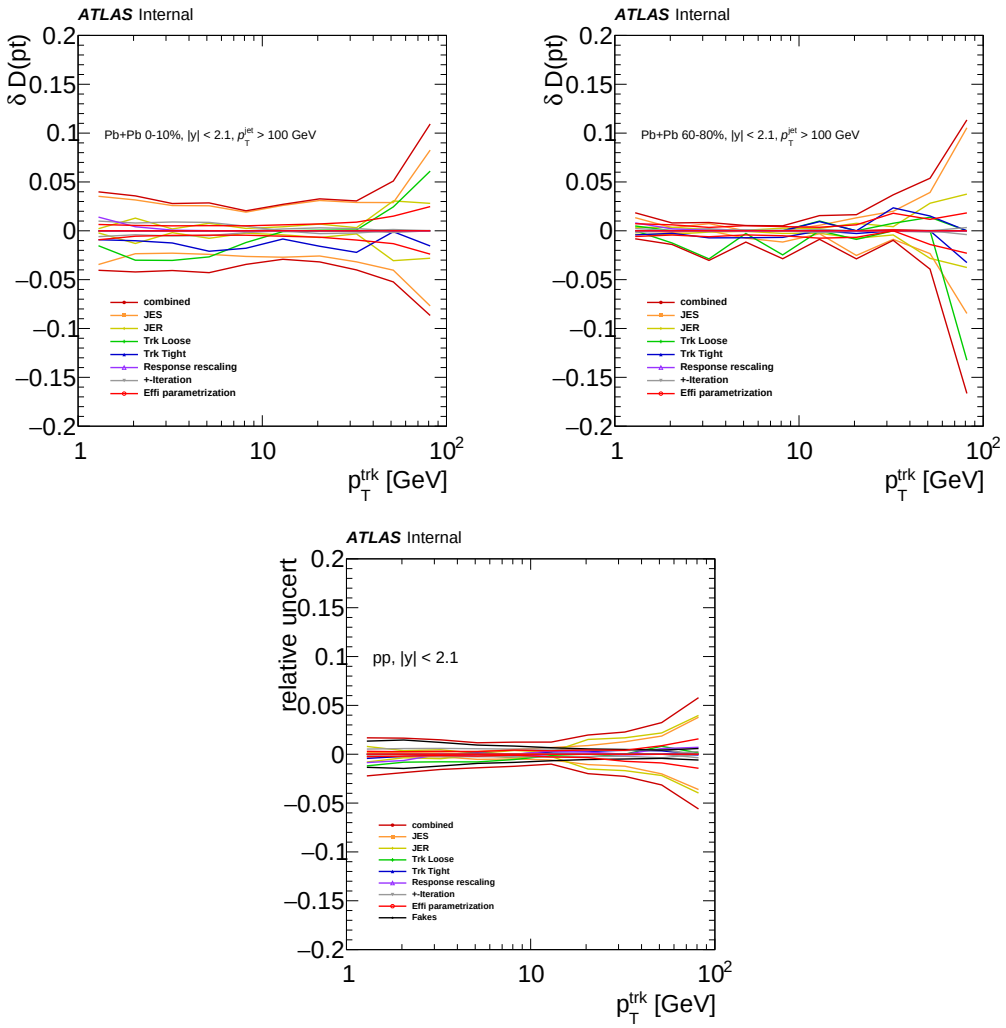

Figure A.9: Size of the positive and negative relative systematic uncertainty and it's sources for $D(p_{\mathrm{T}})$ distributions in inclusive rapidity bin for jets with $p_{\mathrm{T}} > 100$ GeV. Upper left and right panel: central and peripheral HI collisions. Lower panel: pp collisions.

B. Appendix - Inclusive jet suppression

Figure B.1-B.3 shows the trigger performance in terms of the prescale corrected spectra delivered by different triggers.

The centrality dependence for Pb+Pb overlaid with pp for p_{T} distributions in bins of y is shown in Figure B.4. The y dependence for p_{T} distributions in Pb+Pb in difference centrality bins is shown in Figure B.5.

Figure B.6 shows a full set of systematic uncertainites for pp cross-section. Figure B.7 shows systematic uncertainties for Pb+Pb jet yields in all centrality bins, Figure B.8 shows systematic uncertainties for R_{AA} in all centrality bins.

Figure B.9 and B.10 show the per event jet yield in Pb+Pb collisions, multiplied by $1/T_{\mathrm{AA}}$, as a function of jet p_{T} for all centrality bins and all the rapidity bins used in the analysis. The solid lines represent the pp cross-section for the same rapidity selection.

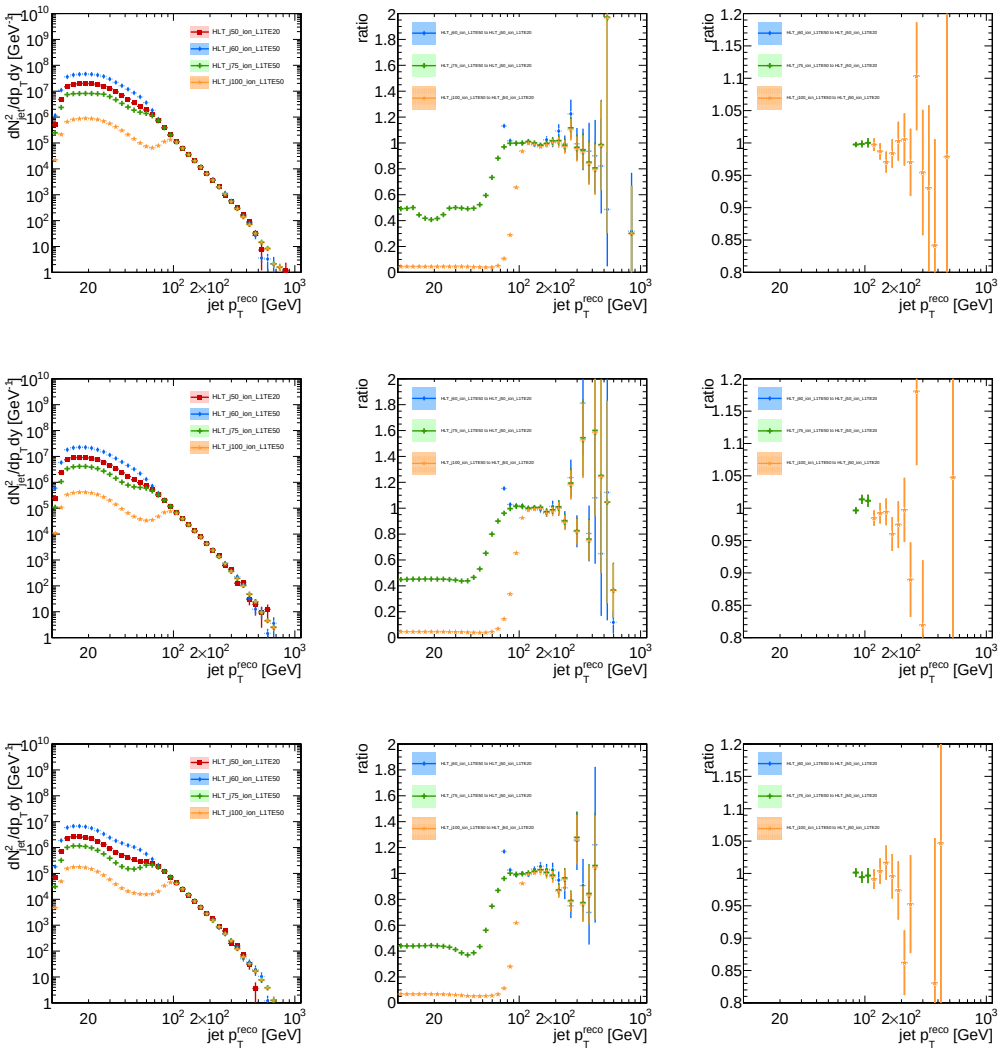

Figure B.1: Left: Prescale-corrected spectra delivered by different triggers. Middle: Ratio of spectra to one of the spectra triggered by one of the lowest p_{T} HLT triggers (indicated in the legend). Right: Ratio of spectra to one of the spectra triggered by one of the lowest p_{T} HLT triggers (indicated in the legend) plotted only in the regions where the given trigger is active. First row: 0-10%, second row: 10-20%, third row: 20-30%.

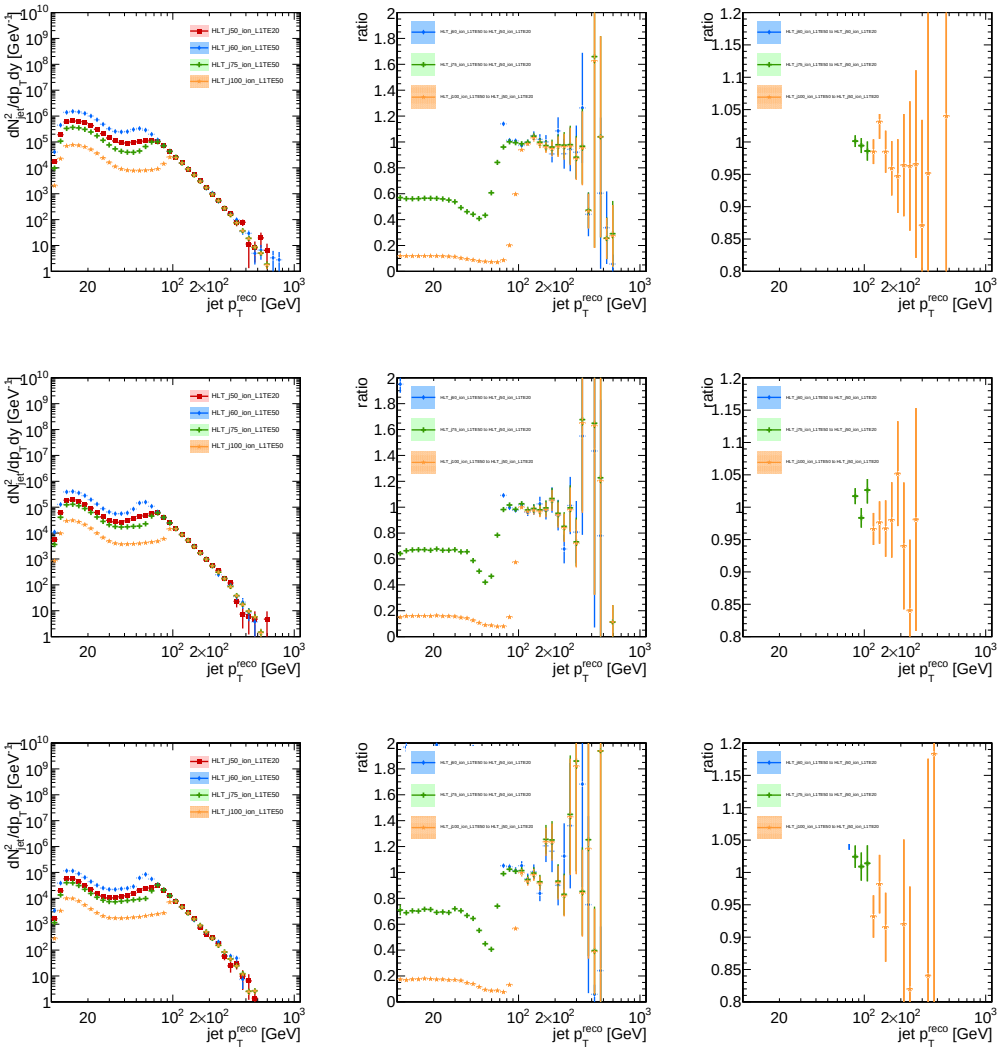

Figure B.2: Left: Prescale-corrected spectra delivered by different triggers. Middle: Ratio of spectra to one of the spectra triggered by one of the lowest p_{T} HLT triggers (indicated in the legend). Right: Ratio of spectra to one of the spectra triggered by one of the lowest p_{T} HLT triggers (indicated in the legend) plotted only in the regions where the given trigger is active. First row: 30-40%, second row: 40-50%, third row: 50-60%.

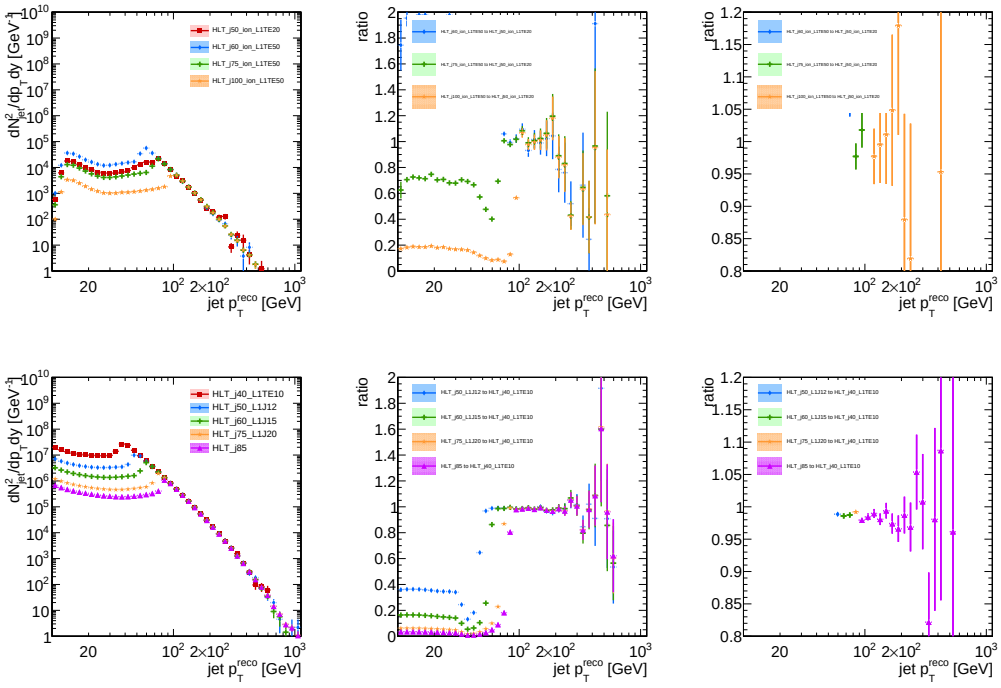

Figure B.3: Left: Prescale-corrected spectra delivered by different triggers. Middle: Ratio of spectra to one of the spectra triggered by one of the lowest p_{T} HLT triggers (indicated in the legend). Right: Ratio of spectra to one of the spectra triggered by one of the lowest p_{T} HLT triggers (indicated in the legend) plotted only in the regions where the given trigger is active. First row: 60-70%, second row: *pp*.

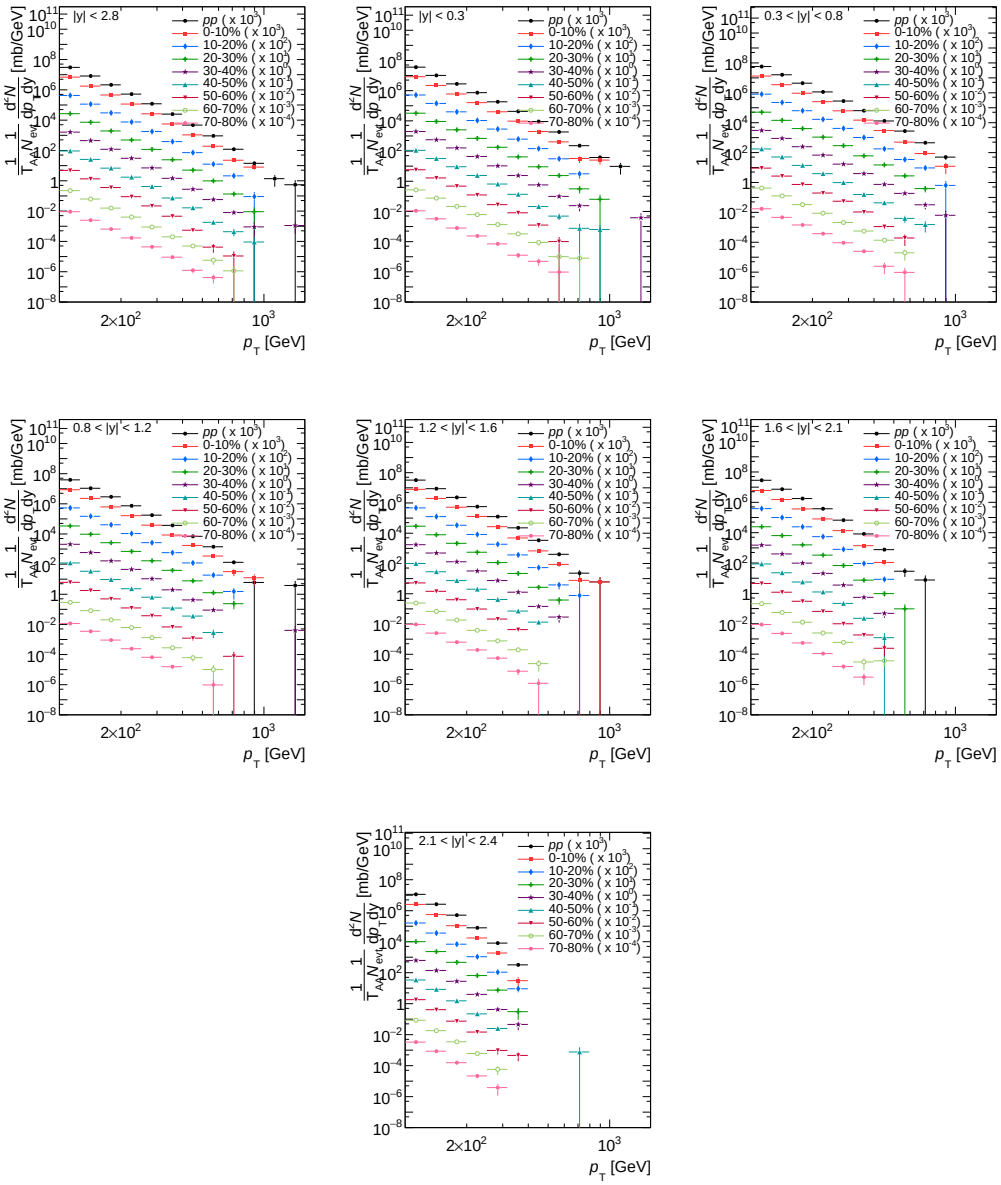

Figure B.4: The raw p_{T} distribution for $R = 0.4$ jets with $p_{\mathrm{T}} > 100$ GeV for pp (pink) and Pb+Pb 0-10% (black), 10-20% (red), 20-30% (blue), 30-40% (green), 40-50% (purple), 50-60% (teal), 60-70% (maroon), and 70-80% (light green) for $|y| < 0.3$ (top left), $0.3 < |y| < 0.8$ (top middle), $0.8 < |y| < 1.2$ (top right), $1.2 < |y| < 1.6$ (middle left), $1.6 < |y| < 2.1$ (middle), $2.1 < |y| < 2.4$ (middle right).

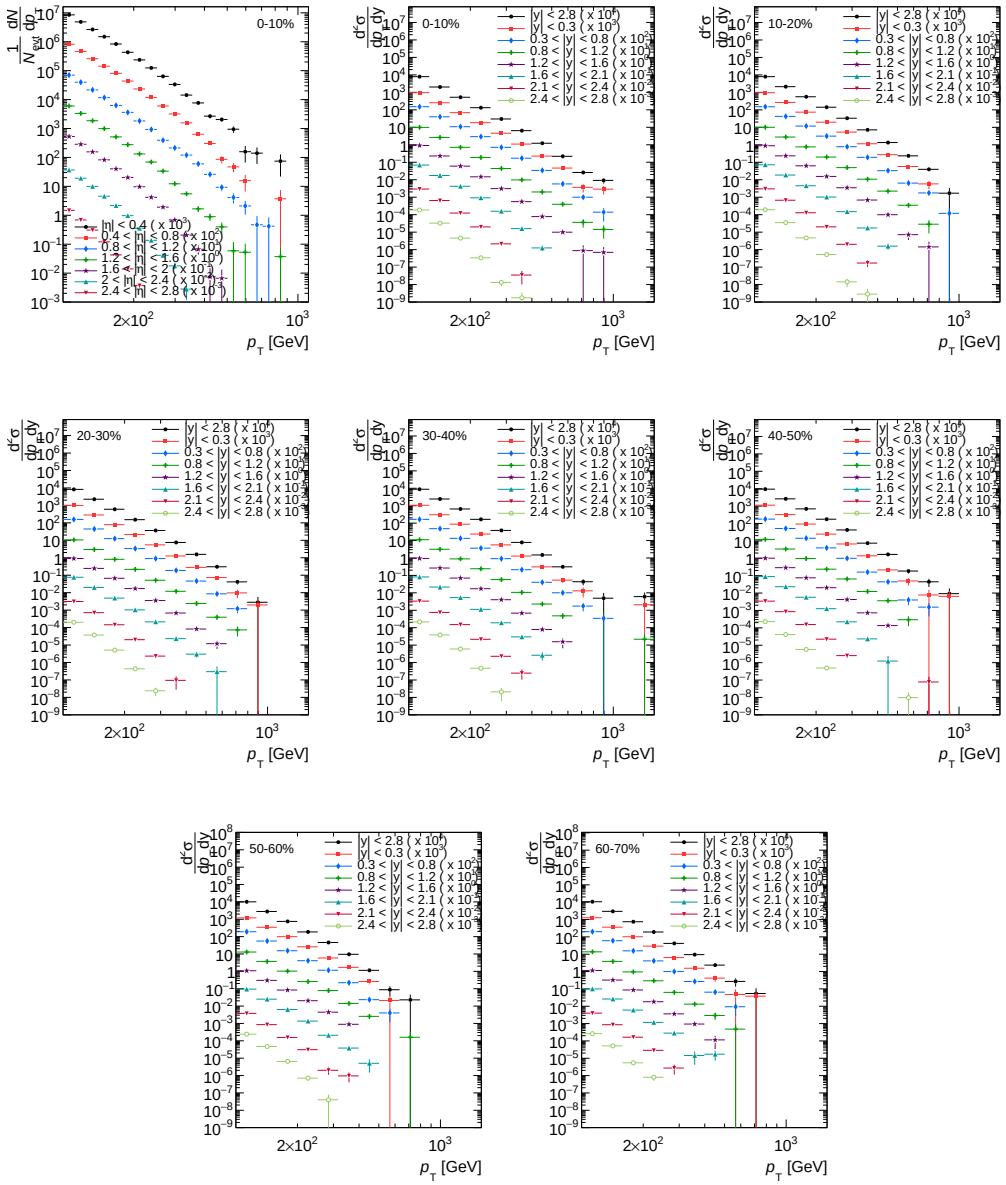

Figure B.5: The raw p_T distribution for $R = 0.4$ jets with $p_T > 100$ GeV for Pb+Pb for $|y| < 0.3$ (black), $0.3 < |y| < 0.8$ (red), $0.8 < |y| < 1.2$ (blue), $1.2 < |y| < 1.6$ (green), $1.6 < |y| < 2.1$ (purple), $2.1 < |y| < 2.4$ (teal), and $2.4 < |y| < 2.8$ (maroon) in 0-10% (top left), 10-20% (top middle), 20-30% (top right), 30-40% (middle left), 40-50% (middle), 50-60% (middle right), 60-70% (bottom left).

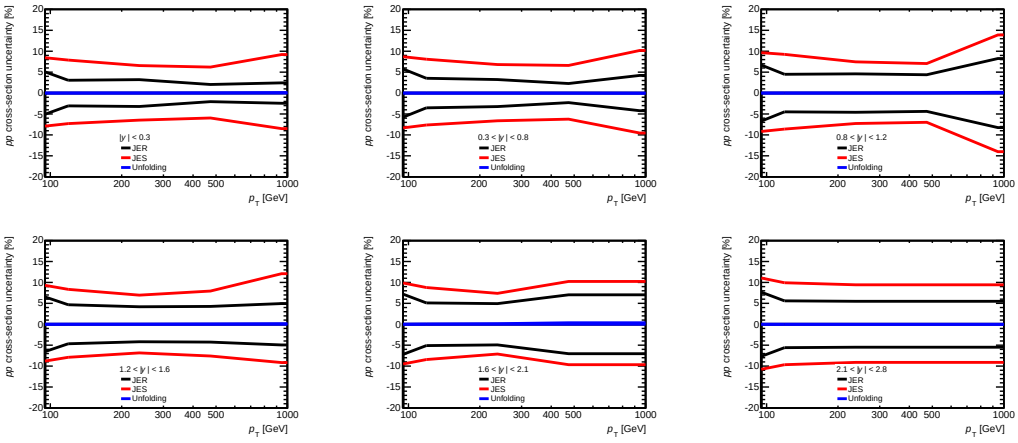

Figure B.6: Systematic uncertainties for pp cross-section for $R = 0.4$ jets with $p_{\mathrm{T}} > 100$ GeV in all the different rapidities.

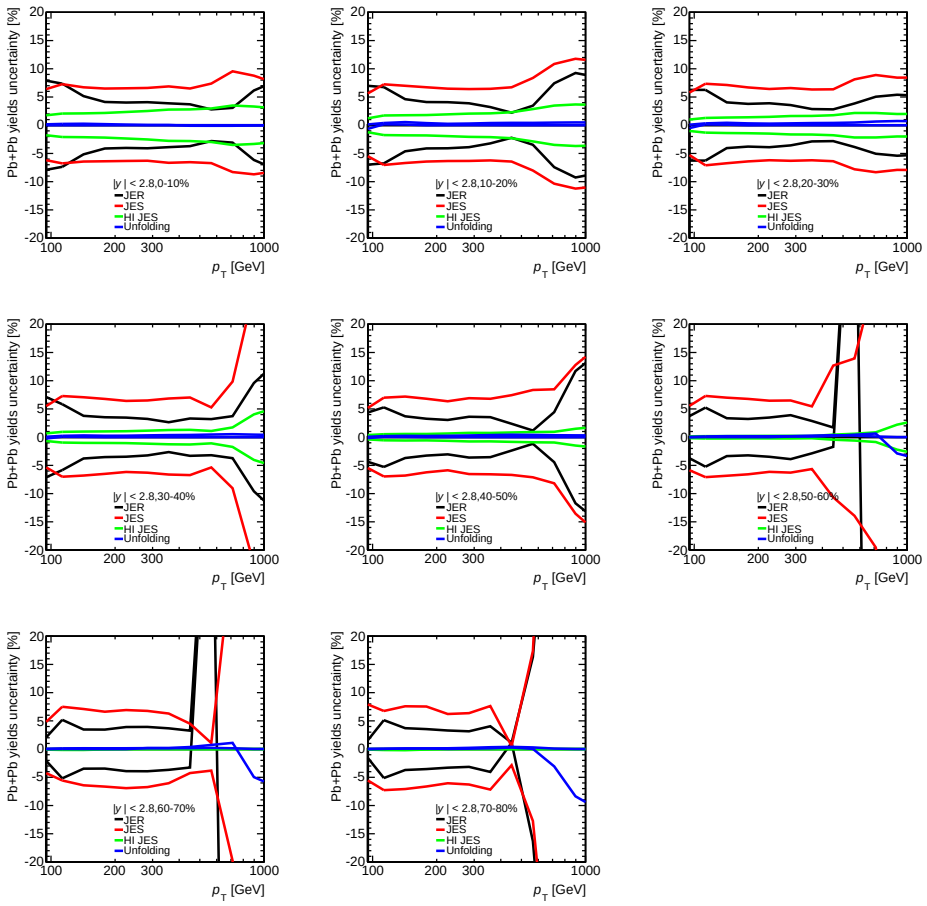

Figure B.7: Systematic uncertainties for Pb+Pb yields for $R = 0.4$ jets with $p_{\mathrm{T}} > 100$ GeV for all the centrality bins and inclusive in rapidity.

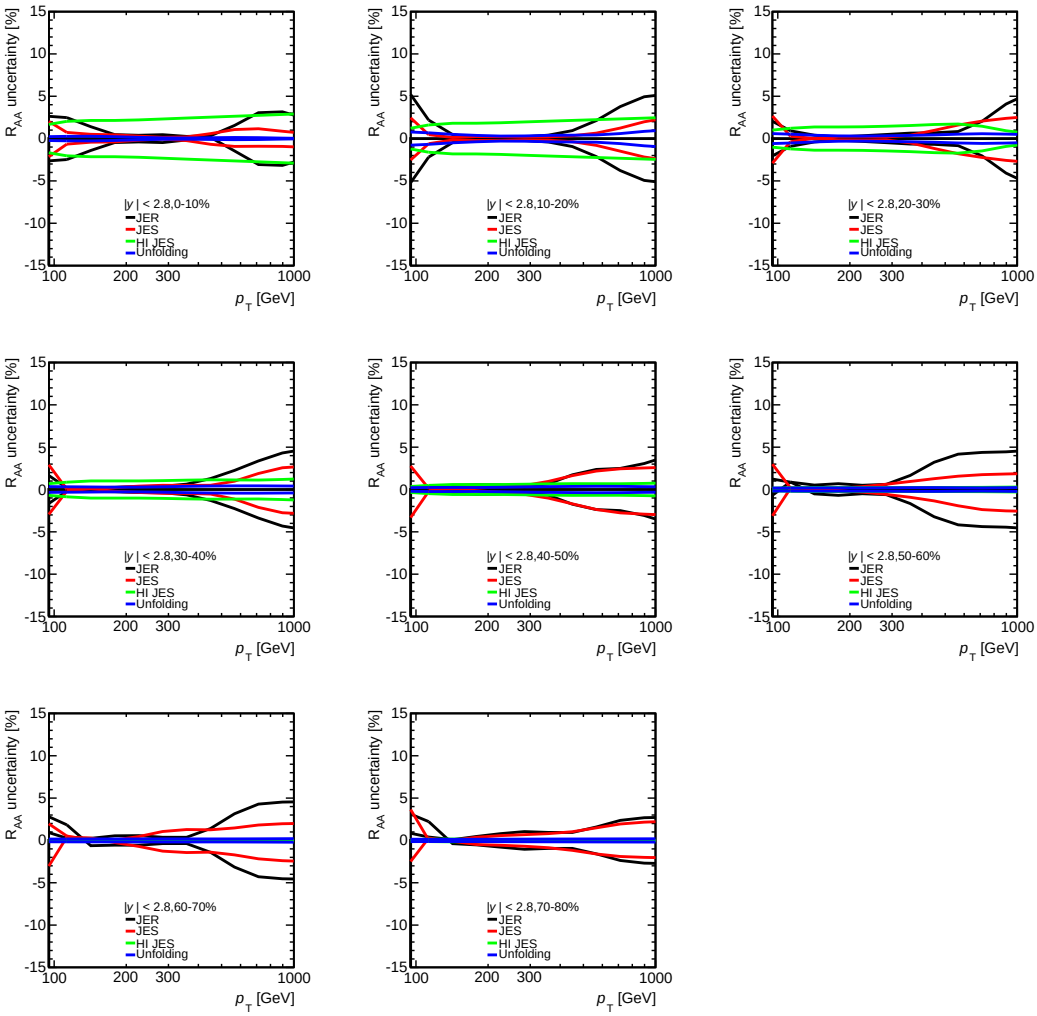

Figure B.8: Systematic uncertainties for R_{AA} for $R = 0.4$ jets with $p_{\mathrm{T}} > 100$ GeV for all the centrality bins and inclusive in rapidity.

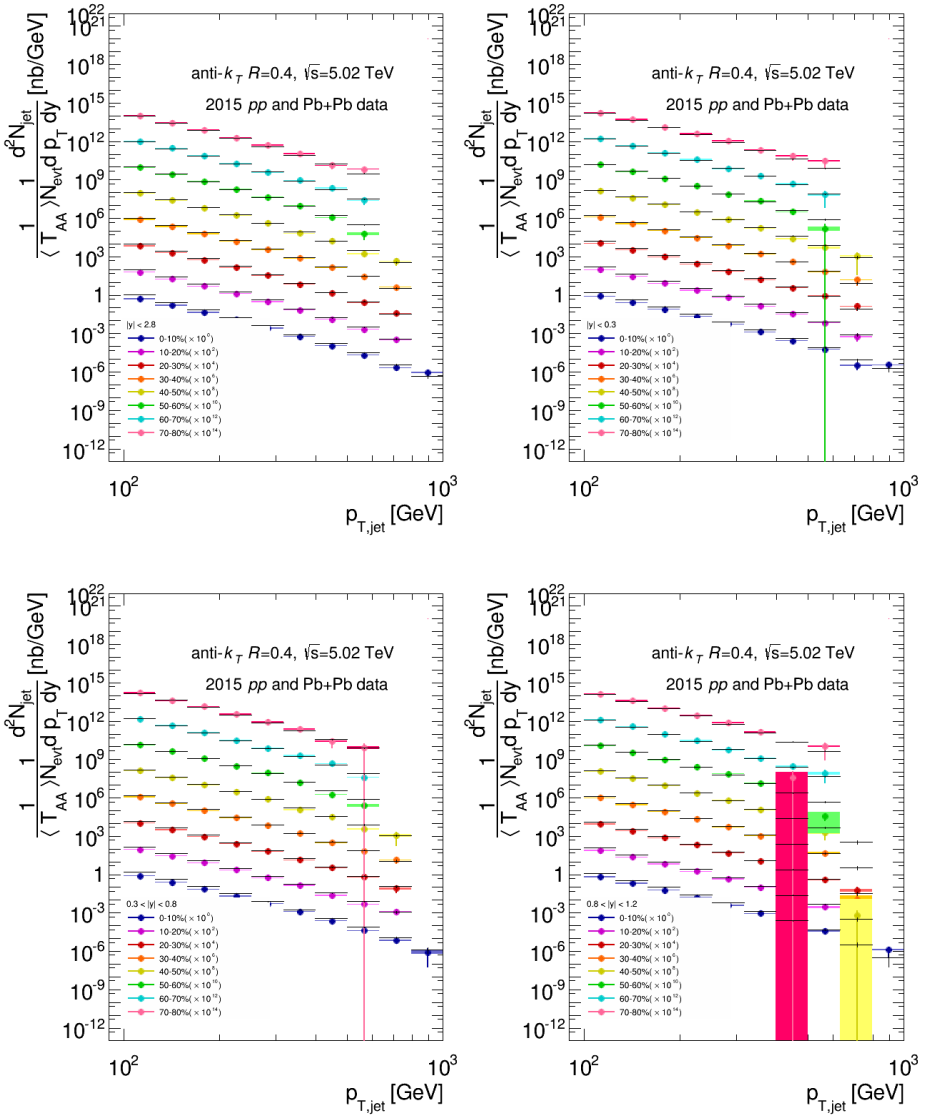

Figure B.9: Per event jet yield in Pb+Pb collisions, multiplied by $1/T_{\mathrm{AA}}$, as a function of jet p_{T} scaled by successive powers of 10^2. The solid lines represent the pp cross-section for the same rapidity selection scaled by the same factor. Rapidity coverage included in the legend.

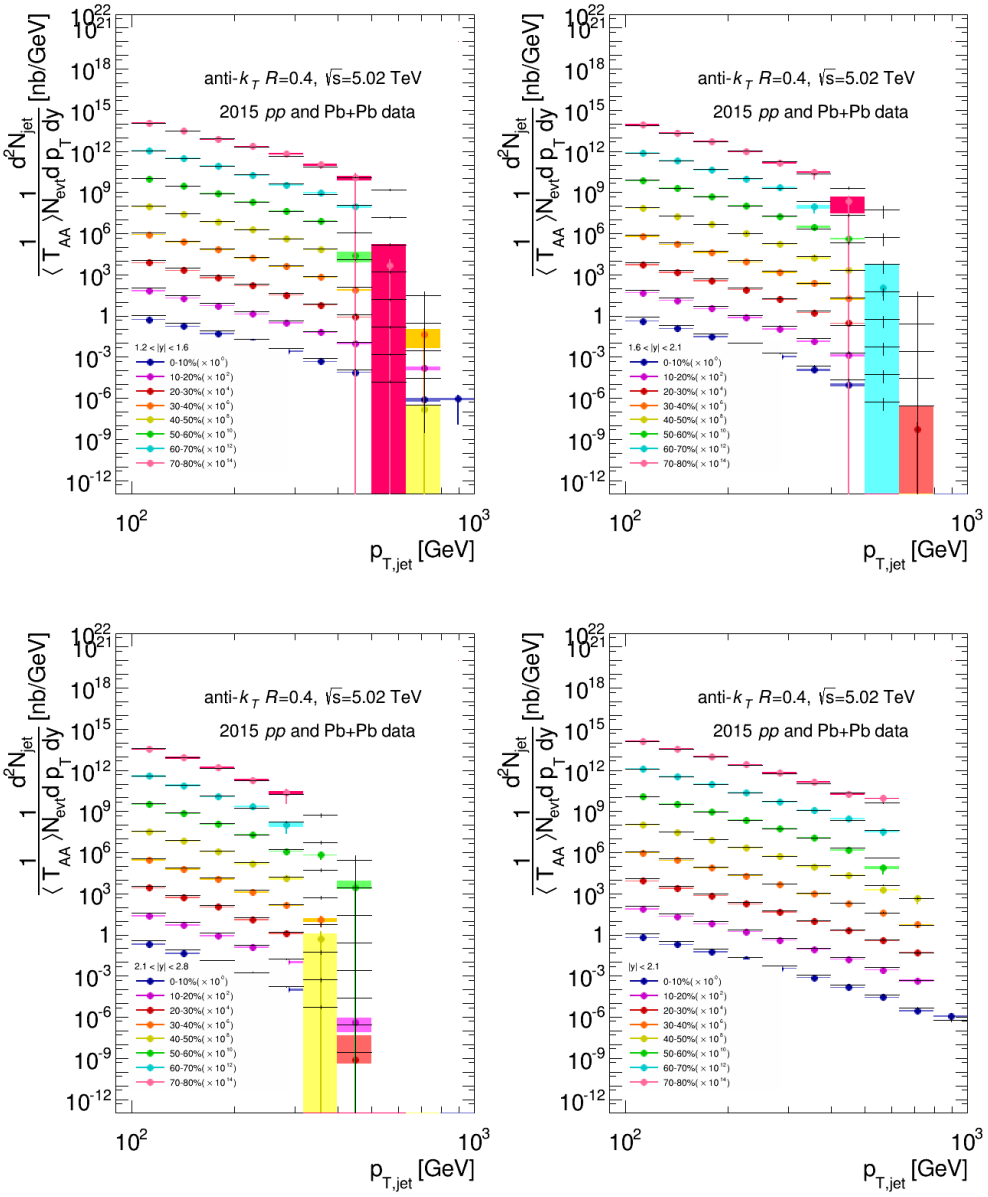

Figure B.10: Per event jet yield in Pb+Pb collisions, multiplied by $1/T_{\mathrm{AA}}$, as a function of jet p_{T} scaled by successive powers of 10^2. The solid lines represent the pp cross-section for the same rapidity selection scaled by the same factor. Rapidity coverage included in the legend.

Bibliography

[1] K. Adcox et al. Formation of dense partonic matter in relativistic nucleus nucleus collisions at rhic: Experimental evaluation by the phenix collaboration. *Nucl. Phys.*, A 757:184–283, 2005.

[2] John Adams et al. Experimental and theoretical challenges in the search for the quark gluon plasma: The STAR collaboration's critical assessment of the evidence from RHIC collisions. *Nucl. Phys.*, A 757:102–183, 2005.

[3] B. B. Back et al. The PHOBOS perspective on discoveries at RHIC. *Nucl. Phys.*, A757:28–101, 2005.

[4] I. Arsene et al. Quark gluon plasma and color glass condensate at RHIC? The Perspective from the BRAHMS experiment. *Nucl. Phys.*, A757:1–27, 2005.

[5] Yacine Mehtar-Tani, Jose Guilherme Milhano, and Konrad Tywoniuk. Jet physics in heavy-ion collisions. *Int. J. Mod. Phys.*, A28:1340013, 2013.

[6] Guang-You Qin and Berndt Muller. Explanation of di-jet asymmetry in Pb+Pb collisions at the Large Hadron Collider. *Phys. Rev. Lett.*, 106:162302, 2011.

[7] Guang-You Qin and Xin-Nian Wang. Jet quenching in high-energy heavy-ion collisions. *Int. J. Mod. Phys.*, E24(11):1530014, 2015.

[8] Jean-Paul Blaizot and Yacine Mehtar-Tani. Jet Structure in Heavy Ion Collisions. *Int. J. Mod. Phys.*, E24(11):1530012, 2015.

[9] ATLAS Collaboration. Measurement of inclusive jet charged-particle fragmentation functions in Pb+Pb collisions at $\sqrt{s_{NN}} = 2.76$ TeV with the ATLAS detector. *Phys.Lett.*, B739:320–342, 2014.

[10] CMS Collaboration. Measurement of jet fragmentation in PbPb and *pp* collisions at $\sqrt{s_{\mathrm{NN}}} = 2.76$ TeV. *Phys. Rev. C*, 90:024908, 2014.

[11] ATLAS Collaboration. Measurement of the jet radius and transverse momentum dependence of inclusive jet suppression in lead-lead collisions at $\sqrt{s_{NN}}$= 2.76 TeV with the ATLAS detector. *Phys.Lett.*, B719:220–241, 2013.

[12] ATLAS Collaboration. Measurements of the Nuclear Modification Factor for Jets in Pb+Pb Collisions at $\sqrt{s_{\mathrm{NN}}} = 2.76$ TeV with the ATLAS Detector. *Phys.Rev.Lett.*, 114(7):072302, 2015.

[13] Nuclear modification factor of high transverse momentum jets in PbPb collisions at sqrt(sNN) = 2.76 TeV. Technical Report CMS-PAS-HIN-12-004, CERN, Geneva, 2012.

[14] ATLAS Collaboration. Measurement of jet fragmentation in Pb+Pb and *pp* collisions at $\sqrt{s_{\mathrm{NN}}} = 2.76$ TeV with the ATLAS detector at the LHC. *Eur. Phys. J.*, C77(6):379, 2017.

[15] ATLAS Collaboration. Study of inclusive jet yields in Pb+Pb collisions at $\sqrt{s_{NN}} = 5.02$ TeV. (ATLAS-CONF-2017-009), Feb 2017.

[16] Radim Slovak. Inclusive jet measurements in Pb+Pb collisions at 5 TeV with the ATLAS detector. Technical Report ATL-PHYS-PROC-2017-004, CERN, Geneva, Jan 2017.

[17] Radim Slovak. Jet Fragmentation in pp, p+Pb and Pb+Pb collisions at ATLAS detector. Technical Report ATL-PHYS-PROC-2017-030, CERN, Geneva, Apr 2017.

[18] J.Chyla. Quarks, partons and Quantum Chromodynamics. 2004. http://www-hep.fzu.cz/chyla/lectures/text.pdf.

[19] H.Politzer. Reliable Perturbative Results for Strong Interactions? *Phys. Rev. Lett.*, 30:1346–1349, 1973.

[20] D. Gross and F. Wilczek. Ultraviolet Behavior of Non-Abelian Gauge Theories. *Phys. Rev. Lett.*, 30:1343–1346, 1973.

[21] C. Patrignani et al. Particle Data Group Collaboration. Review of Particle Physics. *Chin. Phys.*, C 40:100001, 2016.

[22] Y. L. Dokshitzer. Calculation of the Structure Functions for Deep Inelastic Scattering and e^+e^- Annihilation by Perturbation Theory in Quantum Chromodynamics. *Sov.Phys.JETP*, 46:641–653, 1977.

[23] V. Gribov and L. Lipatov. Deep inelastic ep scattering in perturbation theory. *Sov.J.Nucl.Phys.*, 15:438–450, 1972.

[24] G. Altarelli and G. Parisi. Asymptotic Freedom in Parton Language. *Nucl.Phys.B.*, 126:298, 1977.

[25] M. Cacciari and G. P. Salam. Dispelling the N^3 myth for the Kt jet-finder. *Phys. Lett. B*, 641:57, 2006.

[26] S. D. Ellis, D. E. Soper. Successive combination jet algorithm for hadron collisions. *Phys.Rev.*, D48:3160–3166, 1993.

[27] Matteo Cacciari, Gavin P. Salam, and Gregory Soyez. The anti-k_t jet clustering algorithm. *JHEP*, 04:063, 2008.

[28] Y. L. Dokshitzer, G. Leder, S. Moretti, B. Webber. Better jet clustering algorithms. *JHEP*, 9708:001, 1997.

[29] PHENIX collaboration. Formation of dense partonic matter in relativistic nucleus-nucleus collisions at RHIC: Experimental evaluation by the PHENIX collaboration. *Nucl.Phys.*, A757:184–283, 2005.

[30] STAR collaborations. Experimental and theoretical challenges in the search for the quark gluon plasma: The STAR Collaboration's critical assessment of the evidence from RHIC collisions. *Nucl. Phys.*, A757:102–183, 2005.

[31] PHENIX Collaboration. PHENIX detector overview. *Nuclear Instruments and Methods in Physics Research Section A.*, 499(2):469 – 479, 2003.

[32] STAR Collaboration. STAR detector overview. *Nuclear Instruments and Methods in Physics Research Section A.*, 499(2):624 – 632, 2003.

[33] PHENIX collaboration. Suppression of Hadrons with Large Transverse Momentum in Central Au+Au Collisions at $\sqrt{s_{NN}} = 130$ GeV. *Phys. Rev. Lett.*, 89:022301, 2002.

[34] STAR collaboration. Centrality dependence of high pT hadron suppression in Au+Au collisions at $\sqrt{s_{NN}} = 130$ GeV. *Phys. Rev. Lett.*, 89:022301, 2002.

[35] STAR collaboration. Evidence from d+Au measurements for final-state suppression of high pT hadrons in Au+Au collisions at RHIC. *Phys. Rev. Lett.*, 91:072304, 2003.

[36] STAR collaboration. Direct observation of dijets in central Au+Au collisions at $\sqrt{s_{NN}} = 200$ GeV. *Phys. Rev. Lett.*, 97:162301, 2006.

[37] PHENIX collaboration. Trends in Yield and Azimuthal Shape Modification in Dihadron Correlations in Relativistic Heavy Ion Collisions. *Phys. Rev. Lett.*, 104:252301, 2010.

[38] J. D. Bjorken. Energy Loss of Energetic Partons in Quark - Gluon Plasma: Possible Extinction of High p(t) Jets in Hadron - Hadron Collisions (FERMILAB-PUB-82-059-THY). 1982.

[39] A. Peshier. Collisional jet quenching becomes probable. *Phys. Rev.*, C75:034906, 2007.

[40] d'Enterria David. Jet quenching. *Landolt-Bornstein*, 23:471, 2010.

[41] Arkady B. Migdal. Bremsstrahlung and pair production in condensed media at high-energies. *Phys. Rev.*, 103:1811–1820, 1956.

[42] L. D. Landau and I. Pomeranchuk. Limits of applicability of the theory of bremsstrahlung electrons and pair production at high-energies. *Dokl. Akad. Nauk Ser. Fiz.*, 92:535–536, 1953.

[43] R. Baier, Yuri L. Dokshitzer, Alfred H. Mueller, S. Peigne, and D. Schiff. Radiative energy loss and p(T) broadening of high-energy partons in nuclei. *Nucl. Phys.*, B484:265–282, 1997.

[44] B. G. Zakharov. Fully quantum treatment of the Landau-Pomeranchuk-Migdal effect in QED and QCD. *JETP Lett.*, 63:952–957, 1996.

[45] Miklos Gyulassy and Michael Plumer. Jet Quenching in Dense Matter. *Phys. Lett.*, B243:432–438, 1990.

[46] Miklos Gyulassy and Xin-nian Wang. Multiple collisions and induced gluon Bremsstrahlung in QCD. *Nucl. Phys.*, B420:583–614, 1994.

[47] A. Majumder and M. Van Leeuwen. The Theory and Phenomenology of Perturbative QCD Based Jet Quenching. *Prog. Part. Nucl. Phys.*, 66:41–92, 2011.

[48] Wiedemann U. Salgado C. Calculating Quenching Weights. *Phys. Rev.*, D68, 2003.

[49] Wiedemann U. Transverse Dynamics of Hard Partons in Nuclear Media and the QCD Dipole. *Nucl. Rev.*, B582, 2000.

[50] Miklos Gyulassy, Peter Levai, and Ivan Vitev. Jet quenching in thin plasmas. *Nucl. Phys.*, A661:637–640, 1999.

[51] M. Gyulassy, P. Levai, and I. Vitev. Reaction operator approach to non-Abelian energy loss. *Nucl. Phys.*, B594:371–419, 2001.

[52] Jianwei Qiu and George Sterman. Power corrections in hadronic scattering (i). leading 1/q2 corrections to the drell-yan cross section. *Nuclear Physics B*, 353(1):105 – 136, 1991.

[53] Jianwei Qiu and George Sterman. Power corrections in hadronic scattering (ii). factorization. *Nuclear Physics B*, 353(1):137 – 164, 1991.

[54] Ma Luo, Jianwei Qiu, and George Sterman. Anomalous nuclear enhancement in deeply inelastic scattering and photoproduction. *Phys. Rev. D*, 50:1951–1971, Aug 1994.

[55] A. Majumder and Xin-Nian Wang. Dihadron fragmentation function and its evolution. *Phys. Rev. D*, 70:014007, Jul 2004.

[56] A. Majumder and Xin-Nian Wang. Evolution of the parton dihadron fragmentation functions. *Phys. Rev.*, D72:034007, 2005.

[57] Peter Arnold, Guy D. Moore, and Laurence G. Yaffe. Photon emission from ultrarelativistic plasmas. *Journal of High Energy Physics*, 2001(11):057, 2001.

[58] Peter Arnold, Guy D. Moore, and Laurence G. Yaffe. Photon emission from quark-gluon plasma: complete leading order results. *Journal of High Energy Physics*, 2001(12):009, 2001.

[59] Peter Arnold, Guy D. Moore, and Laurence G. Yaffe. Photon and gluon emission in relativistic plasmas. *Journal of High Energy Physics*, 2002(06):030, 2002.

[60] Torbjorn Sjostrand, Stephen Mrenna, and Peter Z. Skands. A Brief Introduction to PYTHIA 8.1. *Comput. Phys. Commun.*, 178:852–867, 2008.

[61] I. P. Lokhtin and A. M. Snigirev. A Model of jet quenching in ultrarelativistic heavy ion collisions and high-p(T) hadron spectra at RHIC. *Eur. Phys. J.*, C45:211–217, 2006.

[62] Nestor Armesto, Leticia Cunqueiro, and Carlos A. Salgado. Q-PYTHIA: A Medium-modified implementation of final state radiation. *Eur. Phys. J.*, C63:679–690, 2009.

[63] Korinna C. Zapp. JEWEL 2.0.0: directions for use. *Eur. Phys. J.*, C74(2):2762, 2014.

[64] Michael L. Miller, Klaus Reygers, Stephen J. Sanders, and Peter Steinberg. Glauber modeling in high energy nuclear collisions. *Ann.Rev.Nucl.Part.Sci.*, 57:205–243, 2007.

[65] Glauber, R. J. Cross Sections in Deuterium at High Energies. *Phys. Rev.*, 100:242–248, Oct 1955.

[66] Roger D. Woods and David S. Saxon. Diffuse surface optical model for nucleon-nuclei scattering. *Phys. Rev.*, 95:577–578, Jul 1954.

[67] H. De Vries, C. W. De Jager, and C. De Vries. Nuclear charge and magnetization density distribution parameters from elastic electron scattering. *Atom. Data Nucl. Data Tabl.*, 36:495–536, 1987.

[68] ATLAS Collaboration. Observation of a Centrality-Dependent Dijet Asymmetry in Lead-Lead Collisions at $\sqrt{s_{NN}} = 2.76$ TeV with the ATLAS Detector at the LHC. *Phys. Rev. Lett.*, 105:252303, 2010.

[69] ATLAS Collaboration. Measurement of the pseudorapidity and transverse momentum dependence of the elliptic flow of charged particles in lead-lead collisions at $\sqrt{s_{NN}} = 2.76$ TeV with the ATLAS detector. *Phys. Lett.*, B707:330–348, 2012.

[70] Lyndon Evans and Philip Bryant. LHC Machine. *Journal of Instrumentation*, 3(08):S08001, 2008.

[71] ATLAS Collaboration. Luminosity public results. https://twiki.cern.ch/twiki/bin/view/AtlasPublic/ LuminosityPublicResults.

[72] ATLAS Collaboration. The ATLAS Experiment at the CERN Large Hadron Collider. JINST 3 S08003, 2008.

[73] ATLAS Collaboration. Measurement of the centrality and pseudorapidity dependence of the integrated elliptic flow in lead–lead collisions at $\sqrt{s_{\mathrm{NN}}} =$ 2.76 TeV with the ATLAS detector. *Eur. Phys. J. C*, 74:2982, 2014.

[74] ATLAS Collaboration. Measurement of the centrality dependence of J/ψ yields and observation of Z production in lead–lead collisions with the ATLAS detector at the LHC. *Phys. Lett. B*, 697:294, 2011.

[75] A. Sidoti. Minimum bias trigger scintillators in atlas run ii. *Journal of Instrumentation*, 9(10):C10020, 2014.

[76] Peter Jenni, Marzio Nessi, and Markus Nordberg. Zero Degree Calorimeters for ATLAS. Technical Report LHCC-I-016. CERN-LHCC-2007-001, CERN, Geneva, Jan 2007.

[77] ATLAS Collaboration. ATLAS High-Level Trigger, Data Acquisition and Controls Technical Design Report. ATLAS TDR-016:369, 2003.

[78] ATLAS Collaboration. *ATLAS level-1 trigger: Technical Design Report.* ATLAS-TDR-12. CERN, Geneva, 1998.

[79] The CMS Collaboration. The CMS experiment at the CERN LHC. *Journal of Instrumentation*, 3(08):S08004, 2008.

[80] The ALICE Collaboration. The ALICE experiment at the CERN LHC. *Journal of Instrumentation*, 3(08):S08002, 2008.

[81] Ulrich W. Heinz. Concepts of heavy ion physics. In *2002 European School of high-energy physics, Pylos, Greece, 25 Aug-7 Sep 2002: Proceedings*, pages 165–238, 2004.

[82] Ulrich W. Heinz. Early collective expansion: Relativistic hydrodynamics and the transport properties of QCD matter. 2009. [Landolt-Bornstein23,240(2010)].

[83] ATLAS Collaboration. Jet energy scale and its uncertainty for jets reconstructed using the atlas heavy ion jet algorithm. ATLAS-CONF-2015-016, Apr 2015.

[84] Martin Spousta. The influence of the underlying event on jet measurements in heavy ion collisions. *J. Phys. Conf. Ser.*, 270:012013, 2011.

[85] Transverse energy fluctuations in Pb+Pb collisions at $\sqrt{s_{NN}}$=2.76 TeV with the ATLAS detector at the LHC. Technical Report ATLAS-CONF-2012-045, CERN, Geneva, Apr 2012.

[86] G. D'Agostini. A Multidimensional unfolding method based on Bayes' theorem. *Nucl.Instrum.Meth.*, A362:487–498, 1995.

[87] Tim Adye. Unfolding algorithms and tests using RooUnfold. In *Proceedings, PHYSTAT 2011 Workshop on Statistical Issues Related to Discovery Claims in Search Experiments and Unfolding, CERN,Geneva, Switzerland 17-20 January 2011*, pages 313–318, Geneva, 2011. CERN, CERN.

[88] Torbjorn Sjostrand, Stephen Mrenna, and Peter Z. Skands. PYTHIA 6.4 Physics and Manual. *JHEP*, 05:026, 2006.

[89] ATLAS Collaboration. ATLAS tunes of PYTHIA 6 and Pythia 8 for MC11. 2011. ATL-PHYS-PUB-2011-009, ATL-COM-PHYS-2011-744.

[90] ATLAS Collaboration. Measurement of charged-particle spectra in Pb+Pb collisions at $\sqrt{s_{\mathrm{NN}}}$ = 2.76 TeV with the ATLAS detector at the LHC. *JHEP*, 1509:050, 2015.

[91] ATLAS Collaboration. Measurement of charged-particle spectra in Pb+Pb collisions at $\sqrt{s_{\mathsf{NN}}}$ = 2.76 TeV with the ATLAS detector at the LHC. *JHEP*, 09:050, 2015.

[92] ATLAS Collaboration. Measurement of the pseudorapidity and transverse momentum dependence of the elliptic flow of charged particles in lead-lead collisions at $\sqrt{s_{NN}}$ = 2.76 TeV with the ATLAS detector. *Phys. Lett.*, B707:330–348, 2012.

[93] ATLAS Collaboration. Selection of jets produced in 13TeV proton-proton collisions with the ATLAS detector. Technical Report ATLAS-CONF-2015-029, CERN, Geneva, Jul 2015.

[94] ATLAS Collaboration. Jet energy measurement with the ATLAS detector in proton-proton collisions at sqrt(s) = 7 TeV. *Eur. Phys. J. C*, 73:2304, 2013.

[95] ATLAS Collaboration. Jet energy scale and its uncertainty for jets reconstructed using the ATLAS heavy ion jet algorithm. ATLAS-CONF-2015-016.

[96] B. Alver, M. Baker, C. Loizides, and P. Steinberg. The PHOBOS Glauber Monte Carlo, arXiv:nucl-ex/0805.4411. 2008.

[97] ATLAS Collaboration. ATLAS Pythia 8 tunes to 7 TeV data. ATL-PHYS-PUB-2014-021, 2014.

[98] Georges Aad et al. Improved luminosity determination in pp collisions at $\sqrt{s}$ = 7 TeV using the ATLAS detector at the LHC. *Eur. Phys. J.*, C73(8):2518, 2013.

[99] ATLAS Collaboration. Measurement of the inclusive jet cross-sections in proton–proton collisions at $\sqrt{s}$ =8 TeV with the ATLAS detector, arXiv:hep-ex/1706.03192. 2017.

[100] Andreas Hocker and Vakhtang Kartvelishvili. SVD approach to data unfolding. *Nucl. Instrum. Meth.*, A 372:469–481, 1996.

[101] ATLAS Collaboration. Measurement of jet fragmentation in 5.02 TeV lead-lead and proton-proton collisions with the ATLAS detector. (ATLAS-CONF-2017-005), Feb 2017.

[102] CMS Collaboration. Measurement of inclusive jet cross-sections in pp and PbPb collisions at $\sqrt{s_{NN}}$=2.76 TeV. *Submitted to: Phys. Rev. C*, 2016.

[103] Measurement of jet suppression in central PbPb collisions at $\sqrt{s_{\mathrm{NN}}}$ = 2.76 TeV. *Phys. Lett. B*, 746:1. 27 p, Feb 2015.

[104] T. Renk. Physics probed by the p_{T} dependence of the nuclear suppression factor. *Phys. Rev. C.*, C88(014905), 2013.

[105] K. C. Zapp, F. Krauss, and U. A. Wiedemann. A perturbative framework for jet quenching. *JHEP*, 1303(080), 2013.